Università degli Studi di Ferrara

DOTTORATO DI RICERCA IN
FISICA

Ciclo XXIX

COORDINATORE Prof. GUIDI VINCENZO

Multinucleon transfer in the ^{197}Au+^{130}Te reaction studied with a high-resolution kinematic coincidence

---

Settore Scientifico Disciplinare FIS/04

Dottorando:
Dott. Galtarossa Franco

Tutore:
Prof. Gambaccini Mauro

Tutore esterno:
Dott. Fioretto Enrico

Anni 2014/2016

The worthwhile problems are the ones you can really solve or help solve, the ones you can really contribute something to. No problem is too small or too trivial if we can really do something about it.

Richard P. Feynman

Contents

1 Introduction

Multinucleon transfer (MNT) reactions are processes in which many nucleons are transferred between target and projectile. In the last decades they have been widely used for the definition of the reaction mechanism that describes the evolution from the quasi-elastic to the more complex deep-inelastic regime and for the study of nuclear structure [1]. These studies benefited considerably from the advent of large γ arrays combined to large acceptance magnetic spectrometers.

In this Chapter we will first introduce some of the most relevant features of heavy-ion reactions at energies close to the Coulomb barrier, mainly focusing on MNT reactions. We will present major experimental results and theoretical models that were or are still being developed to describe the transfer process. We will then discuss recent works devoted to the study of the population of neutron-rich heavy nuclei and the development of new facilities and techniques to study the structure of these exotic nuclei.

1.1. Heavy-ion reactions close to the Coulomb barrier

In heavy-ion reactions very complex quantum mechanical processes take place, which depend on both structures of the colliding nuclei and reaction dynamics. The variety of processes that can occur in heavy-ion collisions at energies close to the Coulomb barrier is schematically depicted in Figure 1.1. Simplifying, one could divide these reactions into main groups, assuming a main depedence on impact parameter and reaction time.

The elastic scattering is fundamental to study the interaction potential between the two nuclei. For instance, the deviation of the elastic cross section from the Rutherford one indicates the onset of competitive reaction channels, spanning from Coulomb excitation of collective degrees of freedom to transfer and progressively more complex ones. The cross section for the elastic scattering depends on both energy and scattering angle and its determination is at the basis of the correct treatment of any scattering process.

The quasi-elastic (QE) scattering belongs to the so-called *peripheral reactions*. In these reactions there is very little change between initial and final states of the nucleus because they occur as a result of the interaction of the projectile with a specific degree of freedom, either of a single nucleon or a collective coordinate. The reaction time is usually very short (10^{-23}-10^{-22} s).

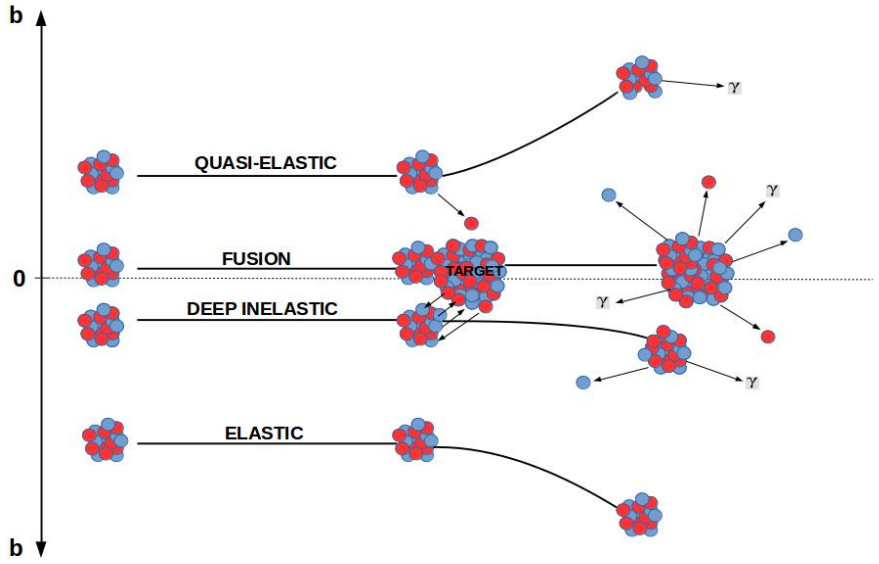

Figure 1.1.: A schematic view of the different types of reactions between heavy ions at bombarding energies close to the Coulomb barrier.

Decreasing the impact parameter deep-inelastic (DIC) components are more likely to show up. The DIC scattering is an intermediate process between quasi-elastic collisions and compound nucleus formation. It usually features a large dissipation of kinetic energy into excitation energy of the fragments and the exchange of many nucleons. Being a peripheral collision, a high angular momentum can be transferred. MNT reactions can be located in between QE and DIC reactions as regards the reaction time and the amount of kinetic energy loss. In MNT reactions a significant number of nuclei can be populated with masses not far from the entrance channel mass partition. They will be discussed in more detail in Section 1.1.1.

At the smallest impact parameters we find reactions that occur in longer times (10^{-18}-10^{-16} s) with respect to direct reactions. Among these processes, very important are the ones leading to the *compound nucleus* (CN). In these reactions a strong rearrangement of nucleons takes place and the kinetic energy of reaction partners is transformed into intrinsic degrees of freedom of the CN. The large number of interactions makes the process random and causes loss of memory of what type of particle brought in the energy that is shared throughout the CN. This can be produced with very high excitation energy, causing the evaporation of particles (mainly neutrons) and γ rays. Fission may be also a strong decay channel, especially for heavy nuclei.

In spite of the large number of processes involved in heavy-ion reactions, some features are common to all of them [2], like, for example, the major role played by the Coulomb force compared to light-ion induced collisions and the large angular momenta involved.

Some of the basic features of heavy-ion reactions can be understood in terms of an interaction potential V(r) between the two colliding nuclei consisting of a Coulomb repulsion $V_c(r)$, a short-range nuclear attraction $V_n(r)$ and a centrifugal potential $V_l(r)$. Let us consider a reaction a+A $\rightarrow$ b+B, with A_i and Z_i the mass and atomic number of the particle i, respec-

tively. A realistic expression for the nuclear interaction is represented by a Woods-Saxon potential with depth V_0, diffusion parameter a and nuclear radii $R_i = (1.20A_i^{1/3} - 0.09)$ fm. The real part of the effective potential in the radial Schrödinger equation can then be written as:

$$\begin{aligned} V(r) &= V_c(r) + V_n(r) + V_l(r) \\ &= \frac{Z_a Z_A e^2}{r} + \frac{V_0}{1 + \exp[(r - R_a - R_A)/a]} + \frac{l(l+1)\hbar^2}{2Mr^2} \end{aligned}$$

where M is the reduced mass $M=(A_a \cdot A_A)/(A_a + A_A)$. To simplify the discussion, in head-on collisions ($l = 0$), when the masses of the two nuclei are not too large ($A_a \cdot A_A < 23400$), this potential shows a maximum, called Coulomb barrier, at a relative distance r_c given by:

$$\left(\frac{\partial V(r)}{\partial r}\right)_{r=r_c} = 0 \ ,$$

For heavier systems the maximum attractive force cannot compensate for the strong Coulomb repulsion and the Coulomb barrier vanishes.

The barrier vanishes also for trajectories associated to large partial waves, with impact parameters $b \neq 0$ corresponding to angular momenta $L_b = b\sqrt{2ME_{cm}}$. For a fixed bombarding energy E_{cm}, increasing impact parameters b lead to increasing angular momenta L_b. For high L_b the centrifugal potential becomes so steep that the maximum nuclear attraction is not able to produce a barrier, as shown in Figure 1.2 for the case of ^{40}Ca+^{40}Ca [3].

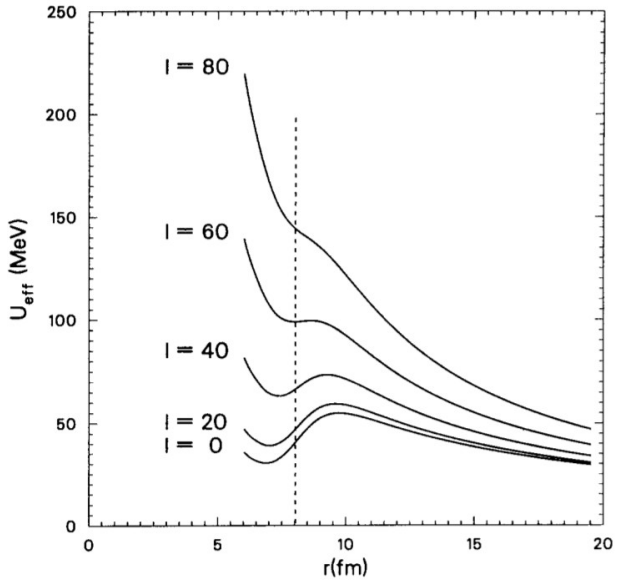

Figure 1.2.: Effective potential for ^{40}Ca+^{40}Ca for different angular momenta l. The dashed line indicates the sum of the radii. Notice that for high values of l the barrier vanishes. Taken from Ref. [4].

For the reaction studied in this thesis, in which $A_{Te} \cdot A_{Au} \sim 25000$, the Coulomb barrier vanishes already for low values of l. This means that the two nuclei can come into contact for

a short time interval but cannot form a compound nucleus even when the impact parameter is close to 0. However, in a simplified macroscopic picture, the nuclei can rotate in a dinuclear configuration exchanging many nucleons and dissipating a considerable fraction of the initial kinetic energy.

1.1.1. Heavy-ion transfer reactions

Processes in which nucleons are transferred between target and projectile take place when the nuclei approach distances where the tail of the wave functions of the nucleons in one nucleus starts to overlap with the nuclear field of the other [3]. Transfer reactions play an essential role in heavy-ion collisions for studies of nuclear dynamics and nuclear structure [1]. In particular, from the determination of form factors and transfer matrix elements one can learn about the relative role of single particle and collective degrees of freedom and the properties of nucleon-nucleon correlations [5, 6]. While with light ions the transfer process can be often treated by a perturbation calculation, with heavy ions one usually needs to employ complex coupled channels to account for the large variety of open reaction channels. This is particularly true when dealing with the evolution of the reaction mechanism from the quasi-elastic to the deep-inelastic regime [7].

In a phenomenological picture, multinucleon transfer reactions can be identified by some characteristic features, among which the specific paths of population of final products, the shape of the angular distributions and the behaviour of the Total Kinetic Energy Loss (TKEL) distributions with increasing number of transferred nucleons.

Due to their grazing character, MNT reactions populate a significant number of nuclei with mass A and nuclear charge Z not far from those of the initial mass partition. This is nicely shown in Figure 1.3 where the Z and A distributions of the light products in the reaction ^{40}Ca+^{208}Pb at E_{lab} = 235 MeV are plotted [8].

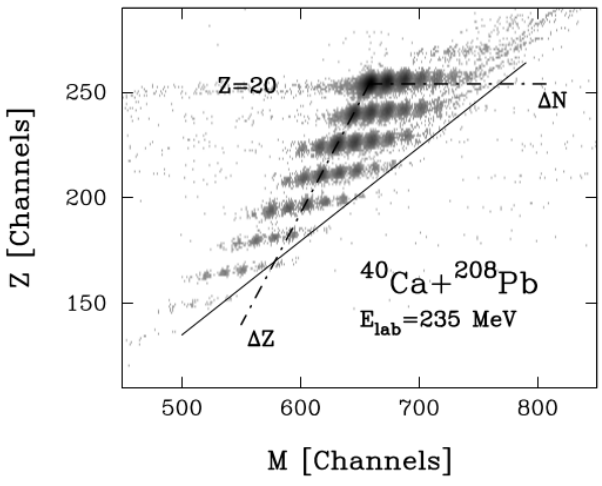

Figure 1.3.: Mass-charge distribution of Ca-like ions in the reaction ^{40}Ca+^{208}Pb at E_{lab} = 235 MeV. The dash-dotted lines correspond to pure neutron pick-up (ΔN) and proton stripping (ΔZ) channels. Taken from Ref. [8].

The most intense spot corresponds to Z = 20 and A = 40 (the ^{40}Ca beam), the dash-dotted lines to pure neutron pick-up (ΔN) and proton-stripping (ΔZ) channels. One can notice that at these bombarding energies (close to the Coulomb barrier) the transfer of as many as about 10 nucleons can occur. Moreover it is evident that not all the channels are open with the same probability but in this case only the proton stripping and the neutron pick-up take place. This behaviour is related to optimum Q-value considerations which will be discussed in more detail in Section 1.2.2.

MNT reactions usually feature bell-shaped angular distributions peaked at the *grazing angle* θ_{gr}. The grazing angle is defined as the scattering angle corresponding to a grazing collision, namely when the distance of closest approach between the two colliding nuclei is very close to the sum of their radii [9]. We remind that the shape of the angular distributions in MNT processes also depends on the bombarding energy. For example at deep sub-barrier energies the bell shape can vanish, being the maximum of the distribution at $\theta_{cm} = 180°$.

Figure 1.4 shows experimental Q-value integrated angular distributions in the reaction ^{64}Ni+^{238}U at E_{lab} = 390 MeV for the indicated transfer channels [10]. For few-nucleon transfers the distributions have the typical bell shape peaked at the grazing angle $\theta_{gr} = 95°$. Moving from large impact parameters (more forward angle) to lower impact parameters (more backward angles), the transfer cross section first increases due to the larger and larger overlap of the interacting nuclei, and then decreases for the absorption effects due to the opening of competing reaction channels and their gradually increasing importance. As more nucleons are transferred the distributions become more spread in angle due to the progressive transition to a deep-inelastic regime.

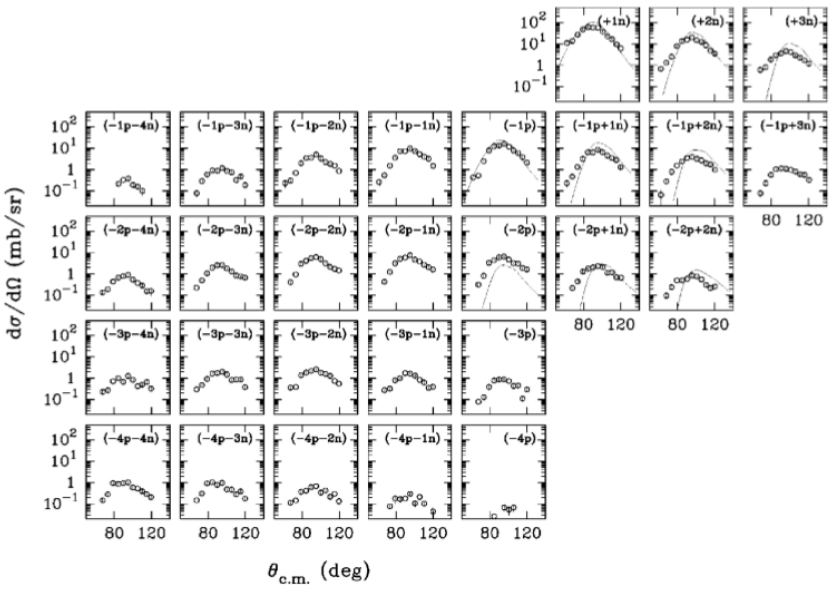

Figure 1.4.: Experimental (points) and theoretical (lines) Q-value integrated angular distributions for the indicated transfer channels in the reaction ^{64}Ni+^{238}U at E_{lab} = 390 MeV. Taken from Ref. [10].

We already mentioned that when the number of transferred nucleons increases, the reaction gradually shifts from a quasi-elastic to a deep-inelastic character. A signature of this behaviour is the progressive decrease of the reaction Q value, i.e. the lower and lower kinetic energy of the outgoing fragments, which is mainly converted into intrinsic excitation of the fragments. The dependence of the Q value on the number of nucleon transferred has been experimentally observed in many systems, like for example the one reported in Figure 1.5 (left), where the Q-value distributions are plotted for different transfer channels. One can notice how Q becomes more and more negative, extending down to $\sim$ -80 MeV, as more nucleons are transferred.

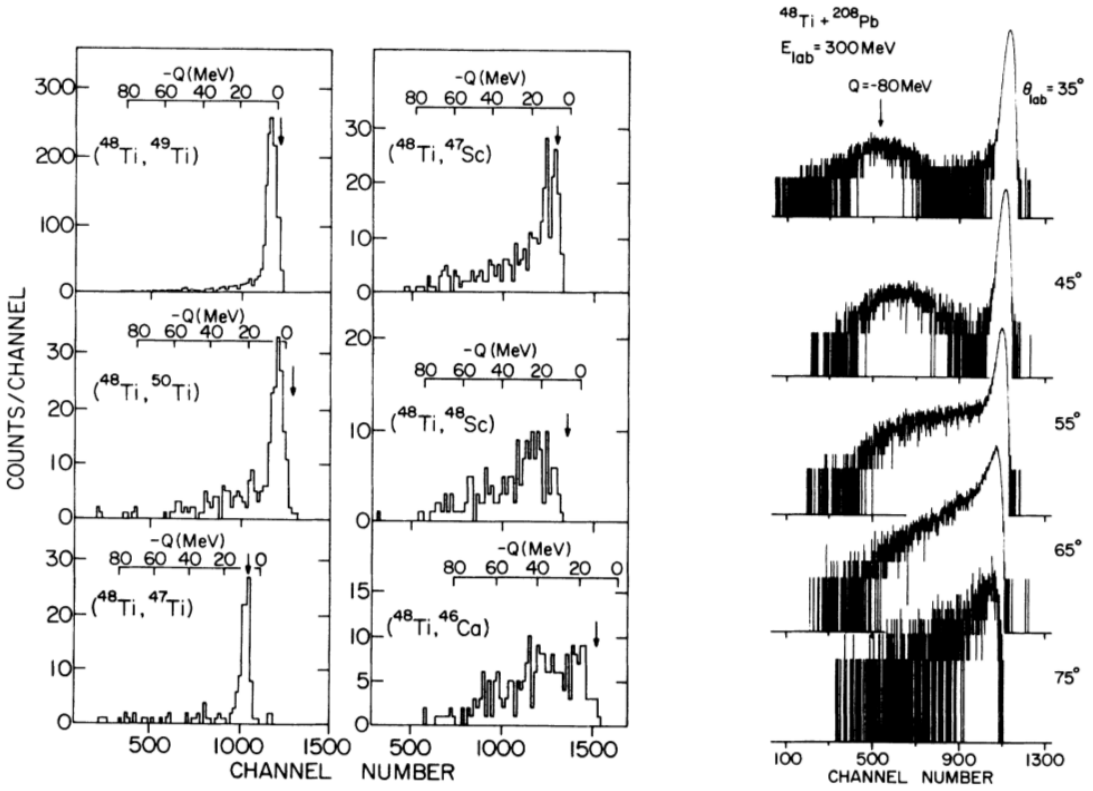

Figure 1.5.: Q-value spectra for the different transfer channels at $\theta_{\rm lab} = 5°$ (left) and mass- and charge-integrated kinetic energy spectra (right) in the reaction ^{48}Ti+^{208}Pb at $E_{\rm lab}$ = 300 MeV. In the left panel the arrows indicate the corresponding ground-to-ground-state Q values. Taken from Ref. [11].

The amount of average kinetic energy lost in typical Coulomb barrier transfer reactions can be understood qualitatively with a very simple model. In a heavy-ion collision the number of open channels is very large (N $\sim$ 100) thus, in first approximation, one can assume that each transfer has the same probability p to occur. Under these assumptions the probability to have the transfer of n particles is simply given by the binomial distribution:

$$P_n = \left(\begin{array}{c} N \\ n \end{array} \right) p^n (1-p)^{N-n}$$

In heavy-ion collisions, 5 MeV can be taken as a typical value of the average energy loss for each transition and 10 as the average number of transferred nucleons. In this simple picture one can then derive an energy loss for the transfer process of the order of 50 MeV, a value compatible with the distributions reported in Figure 1.5 (left).

The onset of deep-inelastic components can be more easily recognised in a plot of the total kinetic energy (TKE) vs the centre-of-mass scattering angle (Wilczyński plot [12]). Here the DIC components should show up as a tail towards larger energy losses, as shown in Figure 1.6. The different trends of the tails extending towards lower TKE are mainly determined by the product of the atomic numbers of projectile and target Z_pZ_t. Increasing this product the reaction evolves from an "orbiting" configuration (top panels), where the two nuclei are in contact for quite a long time and rotate in a di-nuclear configuration exchanging many nucleons, to an intermediate "focusing" configuration (bottom left panel), where they stay in contact for a shorter time and then scatter in a more limited angular range, to a "repulsive" configuration (bottom right panel) where the Coulomb field is so high that the nuclei cannot come into contact. This repulsion is related to the disappearing of the "pocket" of the Coulomb barrier for high partial waves, as seen in Figure 1.2. Concerning bombarding energies and nuclei involved, in the reaction studied in this thesis we will deal with a configuration similar to the Xe-Au one in the bottom left panel.

One can also notice that in some angular ranges the QE and the DIC components are clearly separated, in other they are close together forming a unique structure. This is shown also in Figure 1.5 (right). This feature can make the distinction between QE and DIC very difficult or even impossible from an experimental point of view, thus complicating the theoretical interpretation of data. We will come back on this point in Chapter 6.

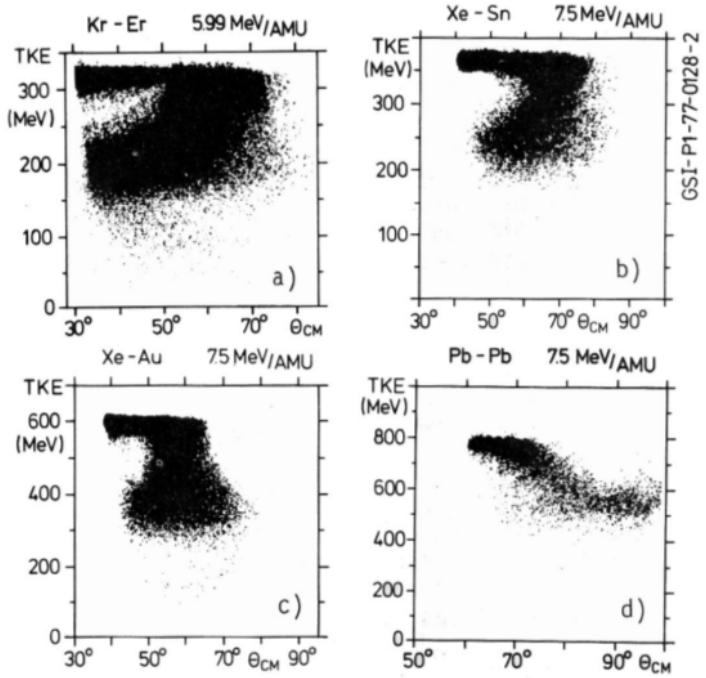

Figure 1.6.: Wilczyński plots for different heavy-ion reactions at the indicated energies. Taken from Ref. [13].

1.1.2. MNT reactions studied with large acceptance magnetic spectrometers

Large acceptance magnetic spectrometers were designed for the detection of low-energy medium-mass reaction products (5-20 MeV/A) in heavy-ion collisions around the Coulomb barrier. In this Section we would like to outline the many possible applications of transfer reactions for different physics cases, like for example the study of transfer dynamics and measurement of transfer cross sections around and above the Coulomb barrier, γ spectroscopy of nuclei moderately far from the stability and nucleon correlation in transfer processes. The first case, whose main characteristics and references have been presented above, is the subject of the present thesis, therefore we will focus on the other two cases.

In recent years MNT reactions have proved to be a powerful tool for γ-spectroscopy studies, which benefited from the combination of large γ arrays and large acceptance magnetic spectrometers. There are several advantages in using γ and particle detectors in coincidence. One can for example tag the particle responsible for the emission of a detected γ ray and perform a Doppler correction for γ rays emitted in flight. The position information of the particle detector can then be used to construct the angular distributions of specific transitions. From the reaction mechanism point of view, the coupling to a γ array can help in the difficult task of discriminating between inelastic and elastic scattering. With heavy ions the typical energy resolution of a magnetic spectrometer is in fact not sufficient to disentangle different excited states in the detected ions and only inclusive cross sections can be determined. When the spectrometer operates in combination with a γ array, the pure elastic scattering, at least in some cases, can be determined by comparing the events with and without γ coincidences.

MNT reactions have been widely used in the last years for lifetime measurements of nuclear excited states. In many of these experiments the Recoil Distance Doppler Shift method (RDDS) [14] was employed, taking advantage of the measurement of the ions velocity inside the spectrometer to distinguish between γ rays emitted before (not Doppler corrected) or after (Doppler corrected) the ion has passed through a degrader placed at a known distance after the target. Thanks to the different Doppler correction a certain γ transition will appear split in two peaks at two slightly different energies, depending on whether the γ ray was emitted before or after the degrader. From the relative intensities of the peaks the lifetime can be measured (see an example in Figure 1.7 left). We only mention here, without entering into more detail, the use of MNT reactions for many other nuclear structure studies, from the validity of the shell model in the medium-mass region to the study of collective motions and shape coexistence. The possibility to identify with a magnetic spectrometer the nucleus responsible for the emission of a specific γ ray turns out to be necessary in this kind of experiments.

The possibility of probing pair correlations in heavy-ion collisions has been an open question for many years. Existing experimental data were explained via the extraction of enhancement coefficients [15] which should provide a direct measurement of the correlation of the populated states. This was made more difficult by the fact that most of the existing studies involved inclusive cross sections at energies above the Coulomb barrier, where the interplay between Coulomb repulsion and nuclear attraction complicates the reaction mechanism [16]. The use of large acceptance spectrometers allowed to perform this kind of studies with enough statistics also using bombarding energies below the Coulomb barrier, where nuclei interact

at very large distances and the effect of the nuclear attraction can be easily accounted for. An example of the transfer probability versus the distance of closest approach for the case of the superfluid system ^{60}Ni+^{116}Sn is shown in Figure 1.7 (right). The experimental data for the (+1n) and (+2n) transfer channels are well accounted for by microscopic calculations which incorporate nucleon-nucleon correlations.

The mentioned sub-barrier measurements have been performed in inverse kinematics, i.e. using a heavy projectile on a lighter target. In fact, the choice of the bombarding energy must in general take into account the experimental difficulty to detect and identify, with enough resolution, heavy ions with very low kinetic energy. At energies close or below the Coulomb barrier this difficulty can be overcome by using inverse kinematics since in this condition the target-like reaction products are forward focused with quite high kinetic energy. The use of inverse kinematics in the experiment discussed in this thesis has been indeed addressed also by these considerations.

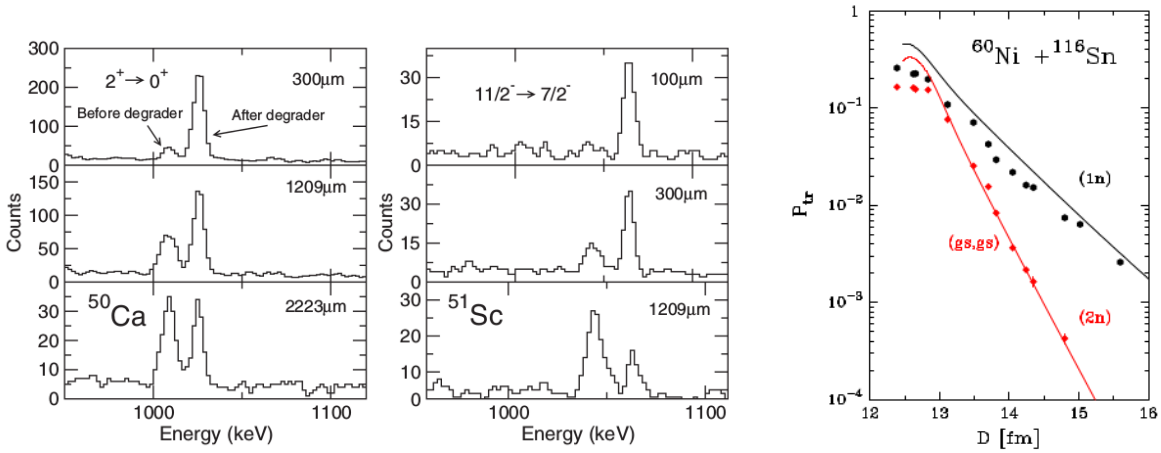

Figure 1.7.: Left: Doppler-corrected γ-ray spectra showing the indicated transitions in ^{50}Ca and ^{51}Sc, populated in the MNT reaction ^{48}Ca+^{208}Pb at E_{lab} = 310 MeV, for different target-degrader distances. Taken from Ref. [17]. Right: experimental (points) and microscopically calculated (lines) transfer probabilities for the one- (^{61}Ni) and two-neutron (^{62}Ni) pick-up plotted as a function of the distance of closest approach D. Taken from Ref. [16].

1.2. Theoretical approach to transfer reactions

Transfer reactions among heavy ions may be described, up to some level, within the fully quantal coupled-channel formalism. However, very often one uses perturbation theory to describe in first order approximation the one-particle transfer and in second order approximation the two-particle transfer [18]. The main features of the process can be better understood in terms of a semi-classical description. In deriving the equations which describe the transfer process, Broglia and Winther [3] showed that it can be treated within the same semiclassical approach used for Coulomb excitation after including the effect of nuclear interaction. The approach is defined semiclassical because the relative motion is treated classically while

inelastic excitations and transfers are treated in a microscopic way.

In this Section we will briefly present the formalism underlying the coupled-channel approach, that is at the base for any description of direct reaction processes [1]. We will focus in particular on an important feature cited previously in this Chapter, the dependence of the cross section on the Q value and the definition of the optimum Q value. We will then present two semiclassical models that were widely used to describe and predict transfer data, GRAZING and the CWKB approximation.

1.2.1. The coupled-channel approach

Let us consider again a reaction a+A $\rightarrow$ b+B. We define $|\Psi\rangle$ the total wavefunction of the system, which can be expanded in terms of exit channel wavefunctions $|\psi_\beta\rangle = |\psi_\mathrm{b}\psi_\mathrm{B}\rangle$, where $|\psi_\mathrm{b}\rangle$ and $|\psi_\mathrm{B}\rangle$ describe the intrinsic states of the two nuclei belonging to the $\beta \equiv (b, B)$ mass partition. The evolution of the system can be described by solving the time-dependent Schrödinger equation

$$i\hbar\frac{\partial}{\partial t}\Psi(t) = H\Psi(t) \tag{1.1}$$

The Hamiltonian H is given by the sum of the single Hamiltonians $\mathrm{H_b}$ and $\mathrm{H_B}$ for the intrinsic states of the two ions, a kinetic term $T_\mathrm{bB} = -\hbar^2\nabla^2_{bB}/2m_{bB}$ which accounts for the relative motion and the effective interaction $\mathrm{V_{bB}}$ between the colliding nuclei:

$$H = H_b + H_B + T_{bB} + V_{bB}$$

One can now express the total wavefunction through the ansatz:

$$\Psi(t) = \sum_\beta c_\beta(t)\ \psi_\beta(t)\ e^{-iE_\beta t/\hbar}\ , \tag{1.2}$$

where the coefficients $c_\beta(t)$ defines the amplitude to be in channel β. Inserting Eq. 1.2 in Eq. 1.1, one finally obtains the following system of coupled equations:

$$i\hbar\dot{c}_\beta(t) = \sum_\gamma \langle\omega_\beta|\, V_\gamma - U_\gamma\,|\psi_\gamma\rangle\ \ e^{i(E_\beta - E_\gamma)t/\hbar}\ c_\gamma(t)\ . \tag{1.3}$$

This system has to be solved with the condition that at t = -∞ it is in its entrance channel α, i.e. $c_\beta(-\infty) = \delta_{\alpha\beta}$. The vectors $|\omega_\xi\rangle$ constitute a dual base introduced to overcome the problem of the non-orthogonality of the vectors $|\psi_\gamma\rangle$.

The matrix elements $\langle\omega_\beta|\, V_\gamma - U_\gamma\,|\psi_\gamma\rangle$ are the most relevant components of Eq. 1.3 because they represent the *form factor*, which reflects the nuclear structure properties of the reaction partners and is used to "weight" the relative importance of different channels.

For the inelastic excitation the form factor can be expressed as the r-derivative of the average potential of entrance and exit channel times a deformation parameter β_λ which bears information on the collectivity of the state:

$$f^\mathrm{inel}_{\beta\gamma}(r) = \beta_\lambda\frac{\partial U(r)}{\partial r}\ . \tag{1.4}$$

For the transfer process the form factor depends not only on the distance r between the two nuclei but also on the momentum transfer $\vec{\kappa}$, $f_{\beta\gamma}(\vec{\kappa}, r)$. At large distances and using the parametrization of Ref. [19], it can be expressed as:

$$f^{\text{tran}}_{\beta\gamma}(0, r) \propto \frac{e^{-\kappa_{a'_1} r}}{\kappa_{a'_1} r} \ , \tag{1.5}$$

where $\kappa_{a'_1}$ contains the binding energy of the single particle state a'_1 entering in the transition and essentially governes the asymptotic behaviour of the transfer form factor. This, at large distances, prevails over the nuclear component of the inelastic form factor.

1.2.2. Q-value dependence of the cross sections

The estimation of the probability of a given transfer process does not require to solve explicitly the whole system of coupled equations: it is instead sufficient to pass through a first-order perturbation expansion. In this approximation we can write the first-order amplitude for the transition $\alpha \to \beta$ as:

$$a^I_\beta(t) = -\frac{i}{\hbar} \int_{-\infty}^{t} \langle \psi_\beta | \, V_\alpha - U_\alpha \, | \psi_\alpha \rangle \ e^{i(E_\beta - E_\alpha)t'/\hbar} \, dt'$$

and the probability is given by

$$P_{\beta\alpha} = |a^I_\beta(t)|^2 \ .$$

Approximating the true trajectory of the transferred particle with a parabolic parametrization, it is possible to find that the transition probability has the following expression:

$$P_{\beta\alpha} = \sqrt{\frac{1}{16\pi\hbar^2 |\ddot{r_0}| \kappa_{a'_1}}} \ |f_{\beta\alpha}(0, r_0)|^2 \ g(Q_{\beta\alpha}) \ , \tag{1.6}$$

where $\ddot{r_0}$ is the radial acceleration at the distance of closest approach r_0 for the grazing partial waves and g(Q) is given by:

$$g(Q) = \exp\left[-\frac{(Q - Q_{opt})^2}{\hbar^2 \ \ddot{r_0} \ \kappa_{a'_1}} \right] \ . \tag{1.7}$$

The optimum Q value Q_{opt} can be written as:

$$Q_{opt} = \left(\frac{Z_d}{Z_A} - \frac{Z_d}{Z_b} \right) E_c + \left(\frac{m_d}{m_b} - \frac{m_d}{m_A} \right) (E - E_c) + \frac{m_d \ \ddot{r_0}}{m_a + m_A} (R_A m_b - R_a m_B) \ , \tag{1.8}$$

where E_c is the Coulomb barrier and m_d and Z_d are the mass and charge of the transferred particle, respectively. The quantities are defined to be positive for stripping reactions, negative for pick-up reactions and zero for inelatic scattering. It is important to keep in mind that this equation is valid when the trajectories of the colliding nuclei match smoothly, i.e. in the approximation that the distances of closest approach before and after the transfer process are equal. This is generally true when the number of nucleons transferred is limited to few units.

The adiabatic cut-off function of Eq. 1.7 is an indication of the transition probability and the maximum of the Gaussian occurs for $Q = Q_{opt}$. Figure 1.8 shows, as an example, plots of the adiabatic cut-off functions for different transfer channels for the reaction ^{58}Ni+^{208}Pb at 330 MeV. The horizontal red bars represent the available states (they extend up to the Q_{gs} value for the indicated channel) and the overlap between red bars and Gaussian distributions corresponds to the open transfer channels. For this reaction we see that only proton stripping and neutron pick-up channels are open, as experimentally proved by Corradi et al. [20].

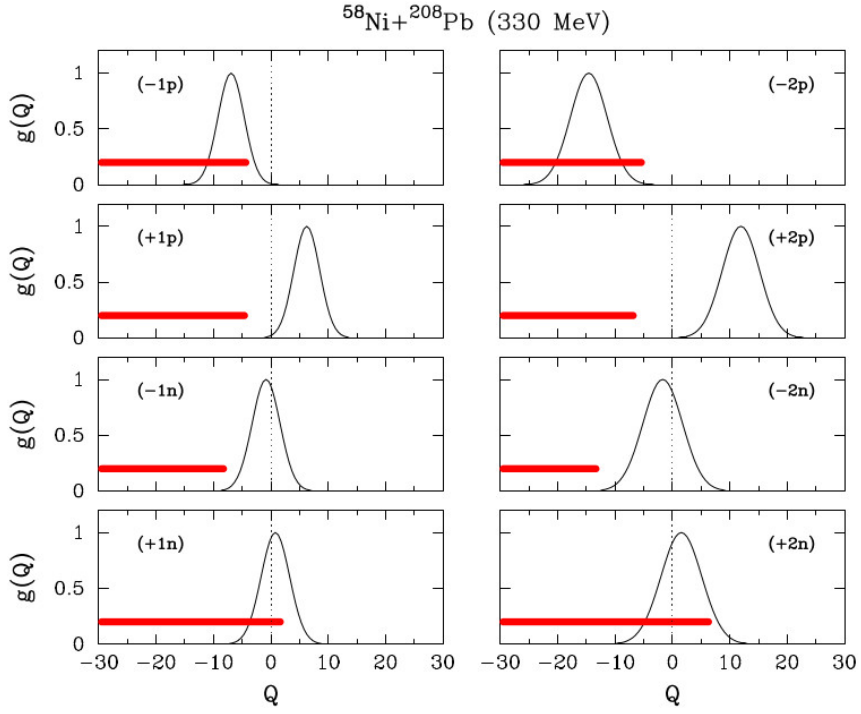

Figure 1.8.: Adiabatic cut-off functions for one- and two-neutron and proton transfer channels for the reaction ^{58}Ni+^{208}Pb at 330 MeV. The Q value (on the x axis) is in MeV. The horizontal red bars represent the location of all possible transitions (see text for details). Taken from Ref. [1].

In Eq. 1.8 the most relevant term for the determination of the optimum Q value is the first one, containing the nuclear charges of initial, final and transferred particles. This means that for neutron transfer channels $Q_{opt} \sim 0$, while proton transfer channels are generally associated to $Q_{opt} \neq 0$, as visible in Figure 1.8.

1.2.3. Semiclassical models for transfer reactions

The use of a semiclassical approach to describe transfer reactions is justified when using heavy ions, since in this case the De Broglie wave length $\lambda = h/p$ associated with the relative motion is much smaller than the interaction region. Among the semiclassical models two have been particularly successful in reproducing experimental data: GRAZING and the Complex WKB. We will outline their main features in this Section, while in the next one we will

present other models that are presently employed to describe the transfer process within a dynamical approach.

The GRAZING model

The necessity to have a description of MNT reactions able to treat at the same time QE and DIC scattering led to the development of the reaction code GRAZING [21]. The formalism on which the code is based is described in Ref. [4, 22].

The semiclassical model GRAZING treats the relative motion of the ions on a classical basis and incorporates surface vibrations and transfer in a microscopic way. The interacting nuclei are represented as an ensemble of independent particles that can vibrate around their spherical equilibrium shapes, the basic degrees of freedom being surface vibrations and single particle degrees of freedom. The two ions, which interact via a Coulomb plus nuclear interaction like the one of Eq. 1.1, can exchange nucleons. As briefly outlined at the end of Section 1.2.1, the excitation of surface modes is treated with a macroscopic approximation whose form factors are given by Eq. 1.4 and whose strengths are deduced from the experimental B(Eλ); the exchange of nucleons is instead governed by microscopic form factors (see Eq. 1.5) which take into account single-particle properties of the colliding ions. The different single-particle states that participate in the transfer process are described by introducing average single particle level densities.

For a given transition characterized by several observables such as excitation energies E_i^*, number of neutrons N_i, number of protons Z_i and so on, GRAZING constructs the associated probability $P(E_A^*, E_B^*, N_A, Z_A, ...)$ not by directly solving the semiclassical system of coupled equations 1.3 but introducing a characteristic function. Without going into detail, we feel important to mention that the transition probabilities are calculated following classical trajectories constructed in a self-consistent way so as to be compatible with the different quantities defining the final states [1].

For the description of the relative motion and for the calculation of the inelastic form factors, GRAZING uses a parametrization of the nuclear ion-ion potential derived by Winther [4]:

$$U_{aA}^{n}(r) = -\frac{R_a R_A}{R_a + R_A} \frac{16\pi\gamma a}{1+\exp[(r-R_a-R_A)/a]} \ , \tag{1.9}$$

where $R_i = (1.20A_i^{1/3} - 0.09)$ fm are the radii of the two nuclei, a the diffuseness of the potential and γ the surface tension which is given by:

$$\gamma = 0.95\left(1 - 1.8\frac{(N_a - Z_a)(N_A - Z_A)}{A_a A_A}\right) \mathrm{MeV}\cdot fm^{-2}$$

where N_i, Z_i and A_i are the neutron, proton and mass numbers of the interacting ions, respectively.

Figure 1.9 shows an example of how GRAZING (histogram) is able to reproduce experimental angle and Q-value integrated cross sections (points) in different measured systems at energies close to the Coulomb barrier. One sees a remarkably good agreement with the data for few nucleon transfers, a feature observed in different studied systems. Deviations between data and calculations become progressively more marked as more nucleons are transferred, most likely due to the fact that GRAZING uses average level densities and does not fully

take into account all DIC components. Indeed it provides only an estimation of the flux that overcomes the Coulomb barrier but is not able to completely follow the evolution of the reaction mechanism toward a more complex regime eventually leading to the formation of a di-nuclear system or of a compound nucleus.

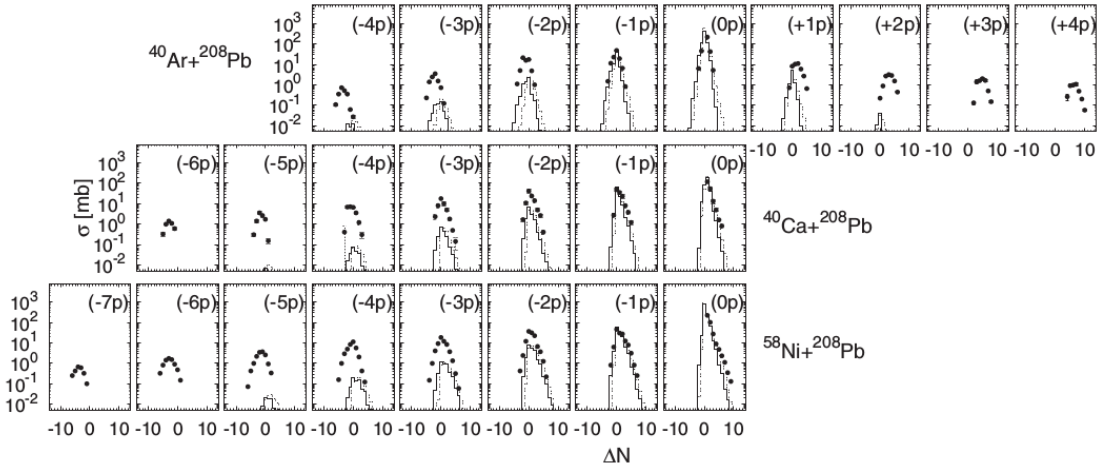

Figure 1.9.: Angle and Q-value integrated experimental cross sections for ^{40}Ar, ^{40}Ca, and ^{58}Ni projectiles on the ^{208}Pb target, at energies E_{lab} = 6.4, 6.2, and 6.0 MeV/A, respectively (points) and the GRAZING calculations not including (dashed line) and including (solid line) neutron evaporation. Taken from Ref. [23].

The CWKB approximation

First introduced into nuclear physics by Knoll and Schaffer in 1973 [24], the complex Wentzel-Kramers-Brillouin (CWKB) theory is a semiclassical model which has been successfully applied to the study of transfer reactions [8, 25]. It uses the WKB approximation [26] for the radial wave functions and for the calculation of the first-order transfer amplitudes. The empirical potential of Ref. [3] is used as the real part, while the microscopically calculated one [27, 28] as the imaginary part of the optical potential. Multinucleon transfer channels are calculated from a multistep mechanism, as in GRAZING, but with the possibility to include explicitly pair transfer modes.

As an example, in Figure 1.10 are shown the angular distributions of inclusive (energy integrated) one-particle transfer channels in two reactions (^{40}Ca+^{208}Pb [8] and ^{58}Ni+^{208}Pb [20]) at energies close to the Coulomb barrier. The calculations are done with the GRAZING (dash) and the CWKB models (solid). One can notice the good agreement between the two models which are able to reproduce the angular distributions, both in shape and absolute values, for the shown transfer channels.

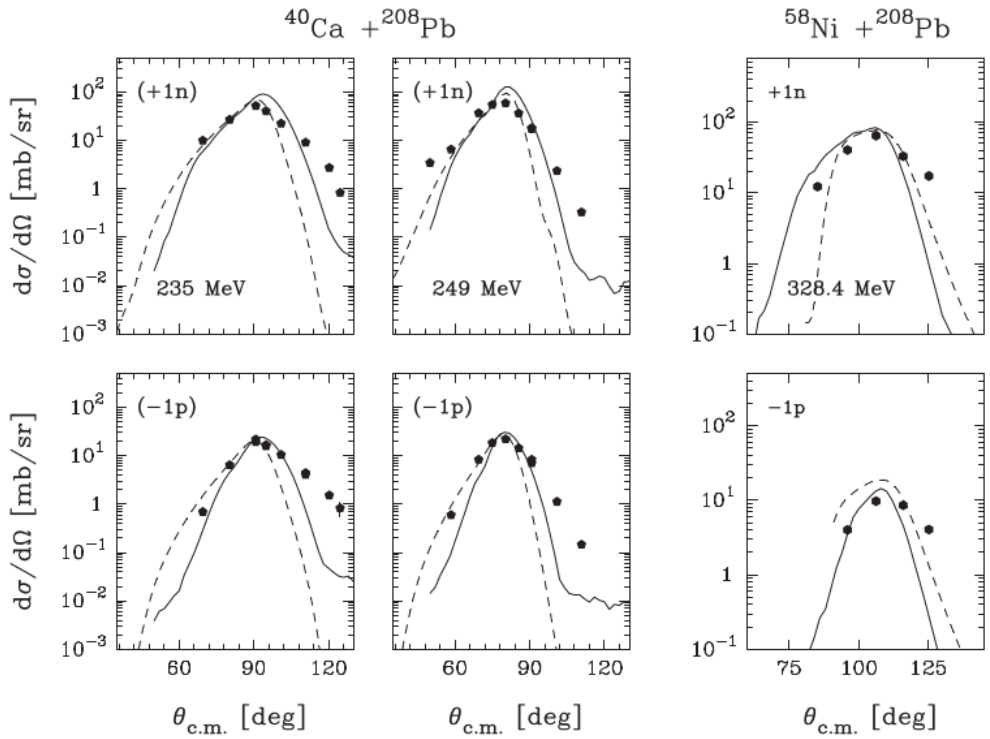

Figure 1.10.: Experimental angular distributions (points) of inclusive one-particle transfer reactions compared with calculations done with GRAZING (dash) and in CWKB approximation (solid) for the indicated systems and bombarding energies. Taken from Ref. [1].

1.3. Other theoretical approaches to MNT reactions

Besides the semiclassical models just described, other models have been developed to describe damped collisions, the dinuclear system (DNS) model [29–39], the improved quantum molecular dynamics model (ImQMD) [40–46], a dynamical model based on Langevin-type equations [47–54] and the time-dependent Hartree-Fock (TDHF) approach.

The DiNuclear System (DNS) concept [29] was proposed to investigate the dynamics of the damped collisions of two very heavy nuclei and to explain the mechanism of complete fusion and quasifission. More recently the DNS model has been extended to transfer reactions to study the population of neutron-rich nuclei [31–33]. In this approach, the production of exotic nuclei is treated as a three-step process. The initial dinuclear system (DNS) is formed in the entrance reaction channel after the dissipation of the kinetic energy of relative motion, then it proceeds through a more complex configuration involving a large mass transfer, eventually decaying into two fragments.

The Improved Quantum Molecular Dynamics (ImQMD) model [40] is an extension of the Quantum Molecular Dynamics (QMD) model, which has been widely used in intermediate energy heavy-ion collisions. As in other transport models, the ImQMD follows the evolution of a nuclear reaction through the time evolution of the coordinate and momentum of each

nucleon. The initial conditions, such as properties of projectile and target nuclei and the corresponding reaction geometry, are very important to study low-energy heavy-ion reactions by means of the transport model description [44]. The ImQMD model was initially employed in the description of fusion reaction at energies close to the Coulomb barrier [40–43]; more recently it was applied to the study of mechanisms and probabilities of production of superheavy fragments in heavy-ion collisions like for example ^{238}U+^{238}U [44, 45].

The dynamical model based on Langevin-type equations [47, 49] was originally developed for the analysis of deep-inelastic scattering and fusion-fission reactions occurring in collisions between heavy ions and later applied also to collisions induced by light ions [54]. The most relevant degrees of freedom in this model are the distance between the nuclear centers (corresponding to the elongation of a mono-nucleus), the dynamic spheroidal-type surface deformations and the mass asymmetry $(A_2\text{-}A_1)/(A_1+A_2)$. Neutron and proton transfers have to be considered separately in deriving the yields of different isotopes of a given element. Except for the neutron and proton asymmetries, for all the other variables the model uses the usual Langevin equations of motion. This model was successfully applied for the description of the angular, energy and mass distributions of reaction products observed in the deep-inelastic scattering of heavy ions at above barrier energies [55]. More recently it has been employed also in the description of multinucleon transfer reactions at energies close to the Coulomb barrier showing the possibility to use these reactions to synthesize superheavy elements [48, 51, 52] and produce heavy neutron-rich nuclei [50, 53].

The Time-Dependent Hartree-Fock (TDHF) theory [56] uses a description that is similar to the Langevin-type one but with the relevant difference that no empirical parameter specific of the reaction is used. Most TDHF calculations presently employ Skyrme-type interactions [57], whose parameters fit a wide mass region. The formulation of the model [58] starts by applying the stationary condition to an action containing an energy density functional (EDF). The EDF is a functional of various densities and is constructed so as to reproduce several properties of finite nuclei and nuclear matter. The TDHF approach was first applied to nuclear collision dynamics in the 1970s [59] and since then the theory has been widely developed and extended, also thanks to the new computational possibilities. The TDHF theory describes the dynamics of both peripheral and central collisions and the nuclear structure is introduced through the mean field which acts as a time-dependent perturbation for the orbitals. In particular, in collisions at small impact parameters, the TDHF theory describes macroscopic dynamics leading to fusion and deep-inelastic collisions (more details can be found in Ref. [56] and references therein).

Figure 1.11(a) shows an example of the evolution of the density distribution for the ^{40}Ca+^{124}Sn reaction at E_{lab} = 170 MeV and impact parameter b = 3.96 fm, calculated in the TDHF framework. One can notice the formation of a neck between the projectile and the target during the collision. The TDHF theory has been recently tested with many available data on multinucleon transfer and has been also compared with GRAZING predictions. Figure 1.11(b) shows an example for the same ^{40}Ca+^{124}Sn reaction.

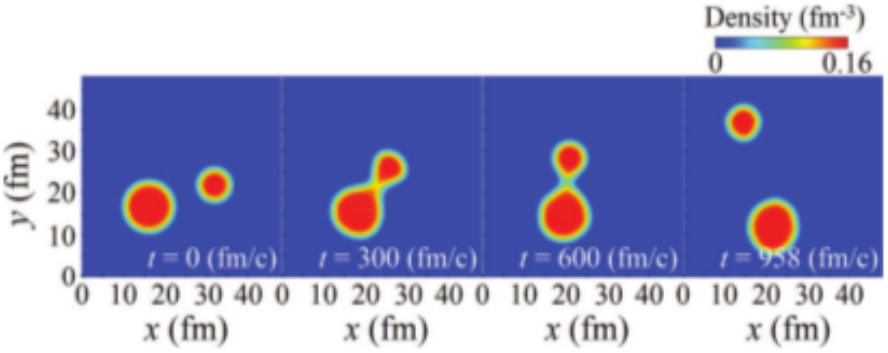

(a) Snapshots of the density distribution for an impact parameter b = 3.96 fm, just outside the fusion critical impact parameter.

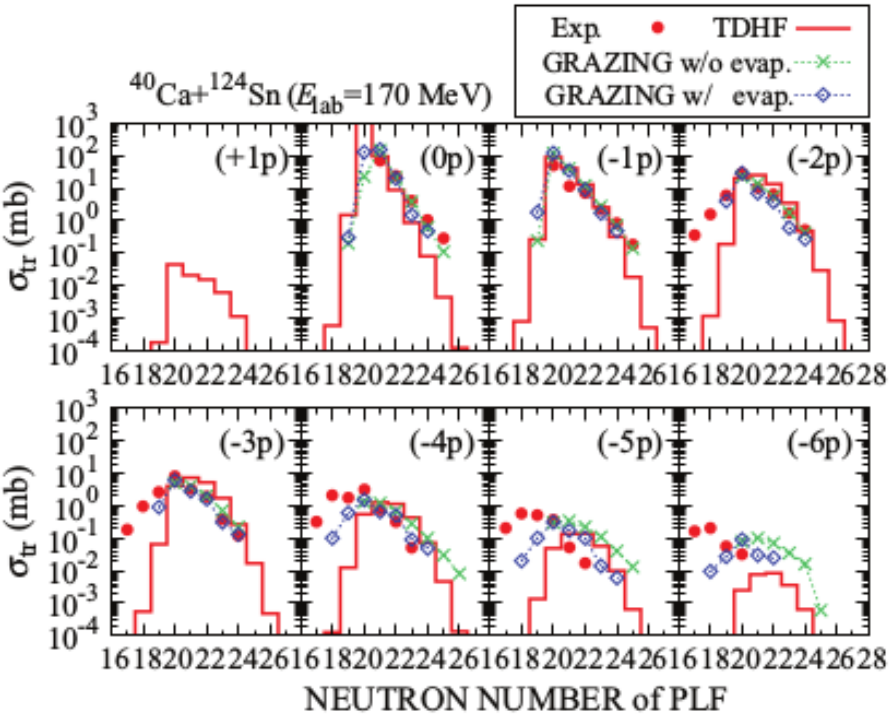

(b) Comparison between calculated and experimental transfer cross sections. Red filled circles denote measured cross sections, red solid lines denote results of the TDHF calculations, and green crosses (blue open diamonds) connected with dotted lines denote calculated results using the GRAZING code without (with) the neutron evaporation effect. Experimental and GRAZING cross sections are from Ref. [60].

Figure 1.11.: Evolution of the density distribution and transfer cross sections for the ^{40}Ca+^{124}Sn reaction at E_{lab} = 170 MeV. Both figures are taken from Ref. [56].

1.4. Neutron-rich nuclei populated in MNT reactions

The production of heavy neutron-rich nuclei with stable beams has always been a very challenging task. Conventionally fusion, fission, and fragmentation are used to this aim. These three methods show in general significant limitations, in particular for the specific case of the production of neutron-rich nuclei near N = 126 and beyond, which is pertinent to the general framework of the present thesis. Fusion is made unsuitable for the production of isotopes with Z < 82 by the lack of relevant stable beams and targets; asymmetric fission would produce the nuclei of interest with extremely small cross sections; fragmentation of Pb [61] and U [62, 63] suffers from rapidly decreasing cross sections with proton removal.

In recent years the renewed interest in transfer reactions has been mainly due to the realization that MNT reactions could be used to populate nuclei moderately rich in neutrons [50, 64, 65]. Experimentally it was shown [20] that in heavy-ion collisions at energies close to the Coulomb barrier, the cross sections for multinucleon transfer processes are rather high. At the same time the use of a low bombarding energy reduces the excitation energy of the fragments and, as a consequence, after the evaporation of a few neutrons, one of the surviving residual nuclei might remain far from the stability line.

One could naively think that any neutron excess in a light projectile has a fair chance to be deposited in a target but a rapid glance at the nuclear chart tells us that for nuclei with Z > 60 only neutron-deficient isotopes are produced by ordinary nuclear reactions with stable beams. This is due to a well-known rule which states that in transfer processes involving stable projectiles only proton stripping and neutron pick-up are likely to occur. This means that the (light) projectile tends to lose protons and gain neutrons, moving in the "south-east" direction, while the (heavy) target has an opposite trend, as shown by the orange arrows of Figure 1.12. This mechanism populates heavy nuclei to the left of the stability valley.

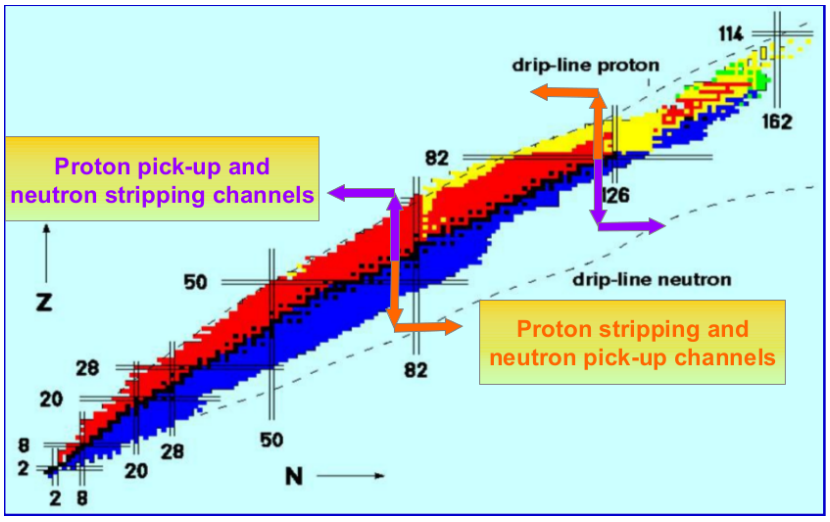

Figure 1.12.: Nuclear chart showing the two possible paths described in the text for a heavy-ion transfer reaction. With neutron-rich projectiles, besides the expected neutron pick-up and proton stripping (orange arrows), neutron stripping and proton pick-up channels (purple arrows) are open.

If one chooses a neutron-rich projectile a transition towards the opposite situation should take place. Figure 1.13 displays contours of calculated cross sections for multinucleon transfer processes where the target is fixed (^{208}Pb) and the projectiles are different isotopes of Xe, from the neutron-poor ^{118}Xe to the neutron-rich ^{154}Xe. One can clearly see that with neutron-rich projectiles, proton pick-up and neutron stripping paths are favoured, leading to the population of neutron-rich nuclei in the region around N = 126 (purple arrows in Figure 1.12).

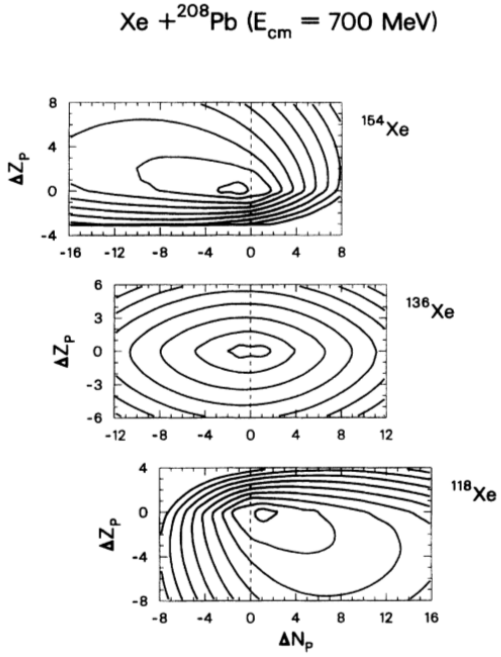

Figure 1.13.: Contours of differential cross sections as a function of the change in projectile neutron number ΔN_p and nuclear charge ΔZ_p in the transfer process for the reaction ^{A}Xe+^{208}Pb at E_{cm} = 700 MeV for the indicated Xe isotopes. Taken from Ref. [64].

In a very recent work [23], a systematic study of the ^{40}Ar+^{208}Pb system clearly demonstrates how, by using the stable neutron-rich ^{40}Ar isotope, the reaction evolves towards neutron stripping and proton pick-up channels.

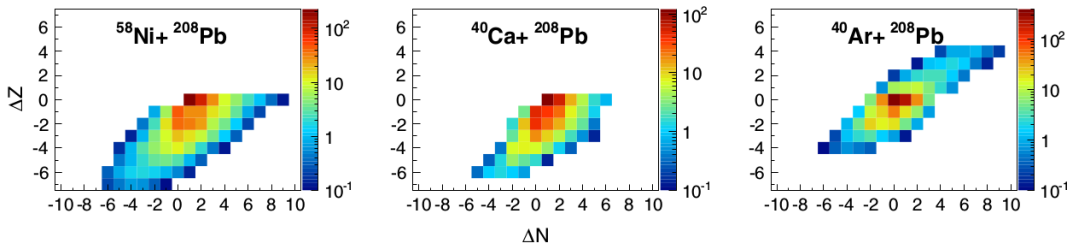

Figure 1.14.: Angle and energy integrated total cross section for ^{40}Ar, ^{40}Ca, and ^{58}Ni projectiles on the ^{208}Pb target, at energies E_{lab} = 6.4, 6.2, and 6.0 MeV/A, respectively. Taken from Ref. [23].

The comparison between this system and other previously studied is reported in Figure 1.14. Here the angle- and energy-integrated total cross section are reported as a function of the number of transferred neutrons and protons for different beams at similar bombarding energies on a ^{208}Pb target. While for the less neutron-rich ^{40}Ca (N/Z = 1) and ^{58}Ni (N/Z = 1.07) only proton stripping and neutron pick-up paths are open, for the more neutron-rich ^{40}Ar (N/Z = 1.22) also the reverse process takes place. This is of course related to the optimum Q-value considerations discussed in Section 1.2.2 with reference to Figure 1.8.

Few studies have been performed so far where transfer reactions have been measured with a complete ion identification in the A $\sim$ 120-140 mass region. Very recently a high resolution measurement has been performed in the ^{136}Xe+^{198}Pt system [66] to study the population yields of neutron-rich nuclei. The measurement was carried out at GANIL in Caen. A beam of ^{136}Xe was directed onto a thick foil of ^{198}Pt with an energy of 7.98 MeV/A ($\sim$ 55% higher than the Coulomb barrier). The Xe-like fragments were detected with the magnetic spectrometer VAMOS++, while the γ rays from both reaction partners were detected by the EXOGAM array [67] with ten CLOVER germanium detectors. With a complex iterative procedure the authors were able to deduce the production of the Pt-like ions around the N = 126 shell closure from the measured energies and angles of the light partner of the reaction. The result is reported in Figure 1.15 and compared with the one of a recent fragmentation measurement performed at GSI, where a 1 GeV/A ^{208}Pb beam impinged on a Be target [61]. The advantage of using MNT reactions to populate neutron-rich nuclei with Z $\leq$ 77 can be clearly seen.

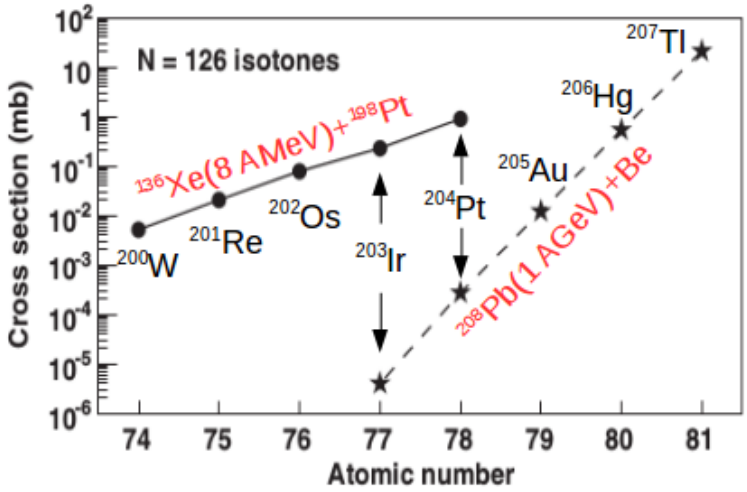

Figure 1.15.: Experimentally deduced cross sections for the N = 126 isotones as a function of the atomic number Z. The filled circles are from the ^{136}Xe+^{198}Pt MNT reaction of Ref. [66], while the filled stars are from the fragmentation reaction ^{208}Pb(1 GeV/A) + Be of Ref. [61]. The solid and dashed lines are to guide the eye. Adapted from Ref. [66].

It is important to keep in mind that, though the production cross sections in a certain mass region are higher for MNT than for fragmentation, the detection yields may be comparable. The recoils produced in fragmentation reactions are indeed strongly forward focused with

yields concentrated in a rather narrow angular range, whereas MNT reactions have much wider angular distributions. The use of MNT is useful also in γ-spectroscopy measurements. The lower β of the produced ions, compared to fragmentation reactions, reduces the Doppler effect and simplifies the associated correction. Moreover fragmentation reactions require very sofisticated detection systems, like for example FRS at GSI [68, 69] or RIPS at RIKEN [70, 71], while for low-energy MNT much more compact magnetic spectrometers, like PRISMA and VAMOS, are perfectly suitable. As an example, in Figure 1.16 a schematic of the FRS at GSI is depicted which clearly illustrates the complexity of the apparatus. Of course these sofisticated devices are unique for experiments devoted to the study of the decay process after radioactive nuclei have been selected and implanted into small-area detectors.

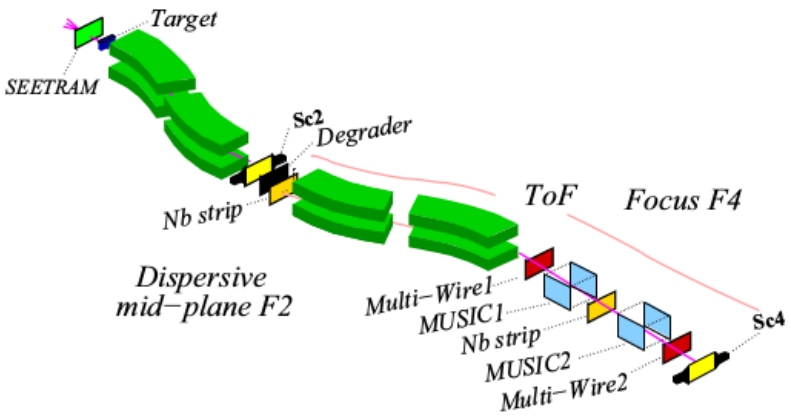

Figure 1.16.: A schematic view of the FRS at GSI. Taken from Ref. [61].

In the framework of studying the population of neutron-rich heavy nuclei and their probability to survive to secondary processes, a large number of experimental studies have been made, in particular by the Dubna group [72–77]. In these works the two-body coincidence method is employed, in which the two reaction products are detected in coincidence by the two-arm time-of-flight spectrometer CORSET [78, 79]. The low mass and energy resolutions (typical values for the cited cases are ~ 7 a. m. u. and ~ 25 MeV, respectively) do not allow to determine the detailed isotopic distributions. Moreover the nuclear charge is not measured. On the other hand the detectors can be placed close to the target, covering a large solid angle, and therefore one can detect both reaction partners with high efficiency. In this way one can study binary processes involving large TKEL, typically constructing bidimensional spectra total kinetic energy (TKE) vs mass. Figure 1.17 shows as an example the mass-TKE distributions of binary fragments measured in the energy range from about the Coulomb barrier ($V_c = 421.5$ MeV) to well above it [74]. One can notice, besides the elastic and quasi-elastic components (high TKE values), a significant part of events attributed to strongly damped collisions (low TKE values). Their contribution to the total cross section increases with increasing bombarding energy. The trade-off between using high bombarding energies to have large primary cross sections but higher contribution from secondary processes and using low bombarding energies to have lower contribution from secondary processes but more modest cross sections is an important issue in the context of the production of neutron-rich nuclei.

This aspect will be further discussed in Chapter 6.

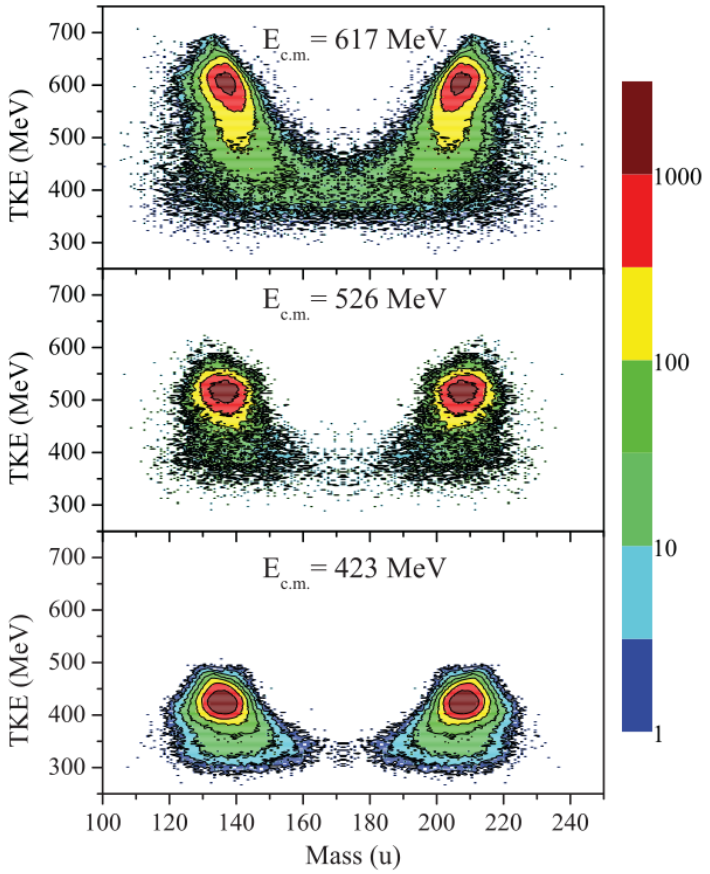

Figure 1.17.: Mass-energy distributions of the primary binary fragments obtained in the reaction ^{136}Xe+^{208}Pb at center-of-mass energies of 423, 526, and 617 MeV, and integrated over the angular range of $40° \leq \theta_{\mathrm{cm}} \leq 140°$. Only true two-body events are included. Taken from Ref. [74].

1.4.1. The astrophysical r-process

Subject of this thesis is the determination of the cross sections of multinucleon transfer channels corresponding to nuclei approaching the regions of the nuclide chart close to N = 82 and N = 126. The extracted cross sections, both in absolute value and in trend as a function of the number of transferred nucleons, are important in the context of using the MNT mechanism for future β- and γ-spectroscopy studies in these regions. In particular, the study of β-decay half-lives and structure of neutron-rich heavy nuclei can shed light on an important astrophysical process, the so-called rapid neutron-capture process of nucleosynthesis (*r-process*).

The r-process, which proceeds under the stellar environment of high neutron densities and high temperatures, is responsible for the creation of about half of the nuclei in nature beyond Fe [80, 81]. It requires high neutron density in order to make neutron capture faster than β decay even for neutron excess nuclei 15-30 units from the stability line. Starting with a

seed nucleus, neutron-rich nuclides are produced via a series of neutron captures until an equilibrium is reached between neutron capture and (γ, n) photodisintegration. Once the neutron source ceases, the progenitor nuclei decay either via β^- or α emission or by fission towards stability and form the stable isotopes of elements up to the heaviest species Th, U and Pu. Nuclei with neutron magic number N = 50, 82, 126 have half lives that are large compared with "regular" r-process nuclides and for this reason they essentially determine the dynamical time scale of the r-process. In correspondence of these neutron-magic nuclei around A = 80, 130, and 195 the r-process should "stall" before they undergo other β decays, hence the name of *waiting points* given to these nuclei. Much matter is accumulated at these waiting points resulting in the observed peak structure in the r-process abundance distribution shown in Figure 1.18.

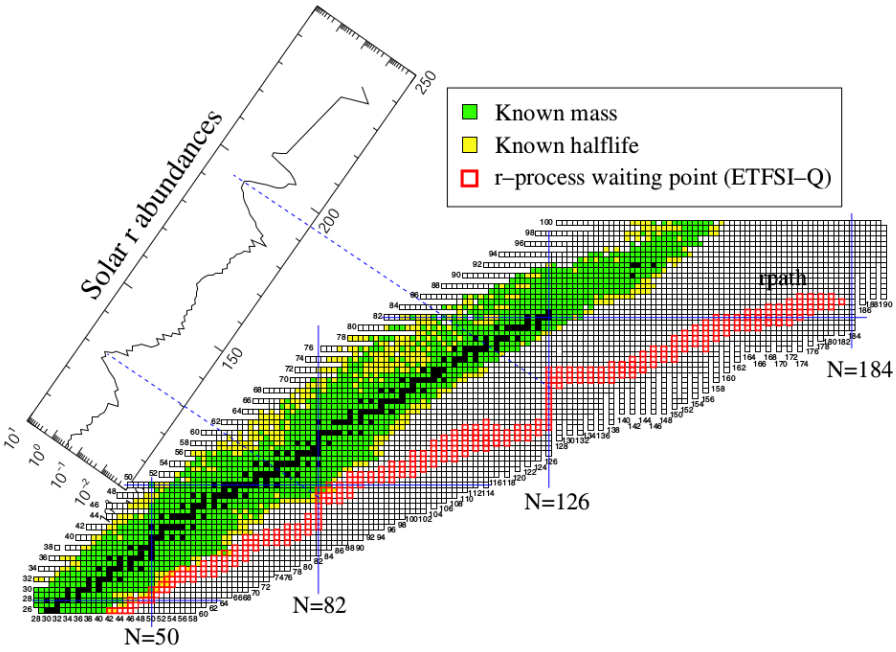

Figure 1.18.: Range of r-process paths, defined by their waiting point nuclei. One can see that the masses and half lives of neutron-rich nuclei through which the r-process paths generally run are experimentally unknown. Blue solid lines indicate proton and neutron magic numbers. Taken from Ref. [80].

The half lives of the nuclei involved in the r-process are related to the decay Q values, which in turn depend on the nuclear masses. As also Figure 1.18 points out, the masses (and the half lives) of neutron-rich nuclei through which the r-process paths generally run are not measured. In these regions the nuclear masses used in large scale nucleosynthesis simulations are largely based on model predictions and additional experimental data are necessary to put constraints on the parameter used in nuclear models. For instance, the measurement of β decay half lives can shed light on the competition between allowed Gamow-Teller and first-forbidden transitions, a crucial information to test models which predict a different relative importance of these two types of transition.

To study the β and γ properties of neutron-rich nuclei with N $\sim$ 126 different set-ups, based

on the In-Gas Laser Ionization and Spectroscopy (IGLIS) approach, are being developed. With this technique one can stop the heavy target-like fragments produced in MNT reactions in a gas cell and then perform a selective resonance laser ionization. This approach allows to extract nuclei with a given atomic number and then separate the different ionized isotopes by means of magnetic fields. The main facilities of this kind under design and/or construction are GALS [82] and CORSAR-V [83] at JINR Dubna and KISS at RIKEN [84–87]. In Figure 1.19 a scheme of the proposed set-up for GALS is depicted, where one can see the structure and the operation principles of these facilities.

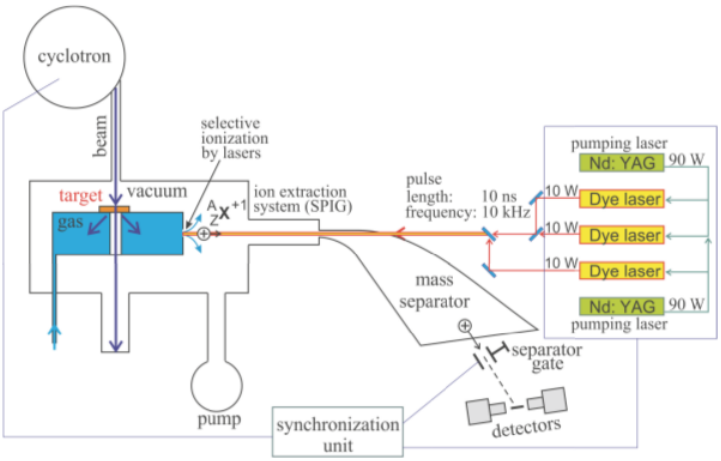

Figure 1.19.: Schematic view of the proposed setup for resonance laser ionization of nuclear reaction products stopped and neutralized in gas and subsequently ionized, mass separated and transported to detecting area. Taken from Ref. [82].

2 Experimental setup

The experiment described in this thesis was performed at the INFN Laboratori Nazionali of Legnaro (LNL) in Italy in July 2014. The ^{197}Au beam was provided by the PIAVE-ALPI accelerator complex. The experimental set-up consisted of the large acceptance magnetic spectrometer PRISMA and an ancillary detection system, composed of a parallel plate avalanche counter followed by an axial ionization chamber, acting as second arm in kinematic coincidence with PRISMA. This setup allows to construct the kinematic coincidence between the binary reaction partners, as we will discuss in Chapter 5.

In this Chapter we will start by introducing the accelerator complex which provided the ^{197}Au beam (at the moment the heaviest beam ever accelerated at LNL). Then we will describe in more detail PRISMA and the coincident second arm. In Chapter 3 we will present the laboratory and in-beam tests carried out to study the performance of the second arm and to investigate about possible developments employing digital electronics to process the signal of the Bragg chamber.

2.1. The accelerator complex

The ^{197}Au beam was provided by the PIAVE-ALPI accelerator complex at LNL with an energy of 1.07 GeV ($\sim$ 5.5 MeV/A) and a current of $\sim$ 1.5 pnA.

PIAVE [88–90] (Positive Ion Accelerator for Very-low Energy) is a positive ion injector for the linac ALPI. Its construction was imposed by the need of accelerating heavy beams (A $>$ 100) which could not be provided by the TANDEM electrostatic accelerator [91–93], even when used as injector for ALPI, due to the short lifetime of the stripper foils with very heavy beams. It consists of two Superconducting Radio Frequency Quadrupoles (SRFQ) and eight superconducting Quarter Wave Resonators (QWR) for an equivalent voltage of about 8 MV. The RFQ has a frequency of 80 MHz and a length of $\sim$ 2 m. It accelerates beams from $\beta = 0.0089$ to $\beta = 0.045$, in the case of a $^{238}U^{28+}$ beam, for an efficient injection into ALPI [89]. A sketch of the PIAVE injector is depicted in Figure 2.1.

The ALPI (Acceleratore Lineare Per Ioni) project [94–97] started in 1989 with the primary goal of extending the XTU TANDEM performance toward heavier beams and higher energies. ALPI is a linear accelerator (LINAC), consisting of 93 independently phased superconducting resonators. The magnets and the linac basic module configuration allow very rigid beams like

$^{197}Au^{13+}$ (which is the case of the present experiment) to be transported. ALPI can boost beams at energies ranging from 6 up to 20 MeV/A, which is sufficient to overcome Coulomb barrier energies also for very heavy systems like U-U [95].

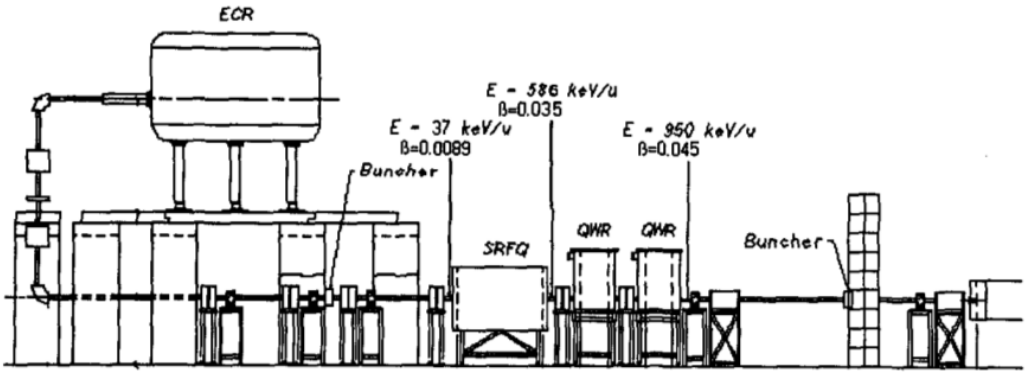

Figure 2.1.: The layout of the PIAVE injector. Taken from Ref. [89].

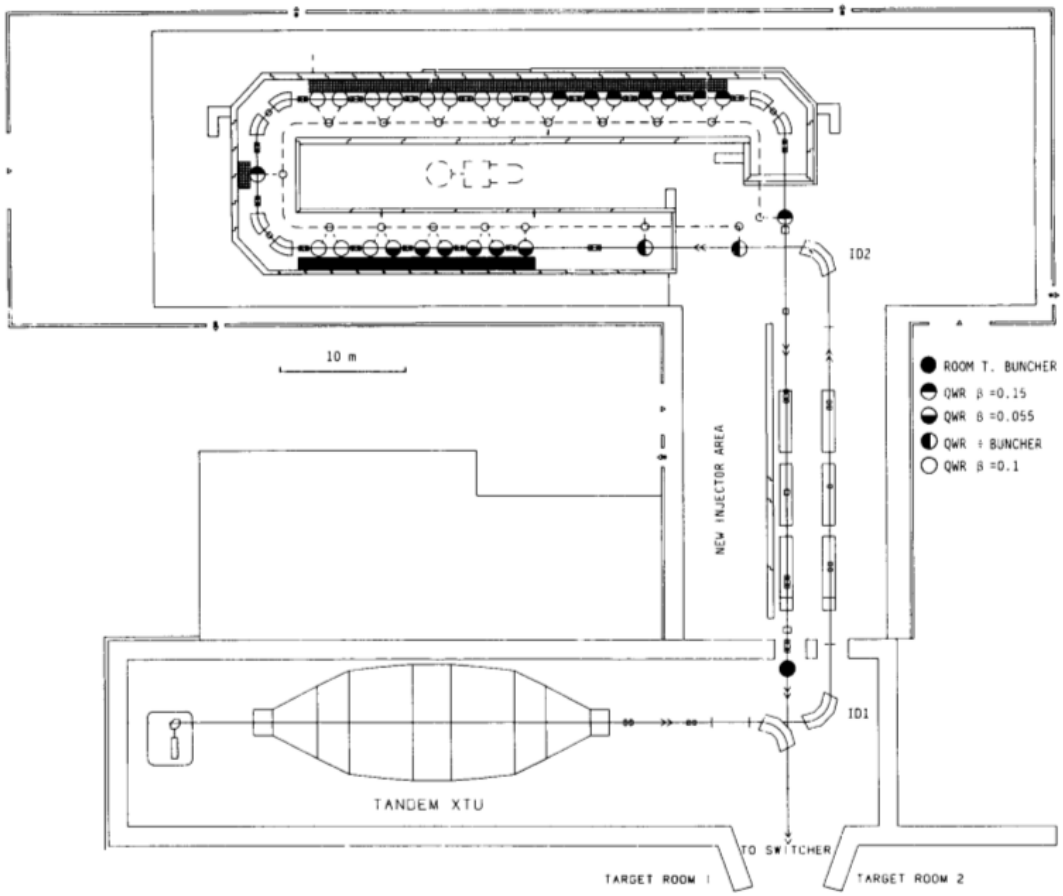

Figure 2.2.: The layout of the ALPI linac (on the top) with the TANDEM electrostatic accelerator (on the bottom). Taken from Ref. [96].

To match the output velocities of the ions coming from the TANDEM ($0.04 < \beta < 0.11$) the linac is divided into three sections based on QWR: a low-β (0.055), a medium-β (0.11) and high-β (0.14) section [97]. The QWR cavities are placed inside cryostats and cooled down by liquid helium, to maintain them in a superconducting state. A sketch of the ALPI linac accelerator is depicted in Figure 2.2. The picture shows also the TANDEM accelerator, which was used to test the second arm with S and Ni beams (see Chapter 3).

After the acceleration in ALPI the beam is delivered to the experimental hall through a switching magnet which bends it on the beam line directed towards the dedicated experimental set-up. Before describing in more detail the detection set-ups, we will briefly outline the main operating principles of the detectors of which they are composed.

2.2. Main operating principles of MCP, MWPPAC and IC detectors

The MCP detector

The Micro-Channel Plate (MCP) detector is a particle detector which combines very good efficiencies, timing and position resolutions with a low energy loss of the ions detected. For this reason it is widely employed in experimental set-ups for nuclear physics studies at low and intermediate energies.

It is routinely used in a non-interceptive configuration, detecting secondary electrons which are produced by ions impinging on a thin carbon foil and then accelerated towards a position-sensitive anode by an electric field. At the same time they are kept confined by a parallel magnetic field to preserve the position information, as schematically depicted in the figure on the right (from Ref. [98], where B_i and B_f indicate a stronger and a weaker magnetic fields, respectively). The position information is provided by a system of delay lines for both the x and y directions and measured as the difference in arrival time of the signals.

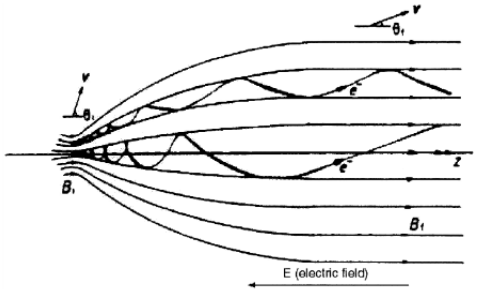

In order to get high gains, a pair of MCP, mounted in a chevron configuration, are placed in front of the anode and amplify the signal by multiplying the electrons. Typical resolutions obtainable with this kind of detectors are 1 mm for position and 350 ps for timing. The efficiency depends on both the nuclear charge and the energy of the incoming ions. Typically for heavy ions like the presently detected Te ones, it is higher than 80%.

The MWPPAC detector

The Multi-Wire Parallel-Plate Avalanche Counter (MWPPAC) detector is particularly useful, in application involving heavy charged particles, when one needs mainly fast timing

and good position information [99]. Among other advantages of using this kind of detectors is the possibility to cover a large area, placing a grid of cathodes between two anode planes (or viceversa).

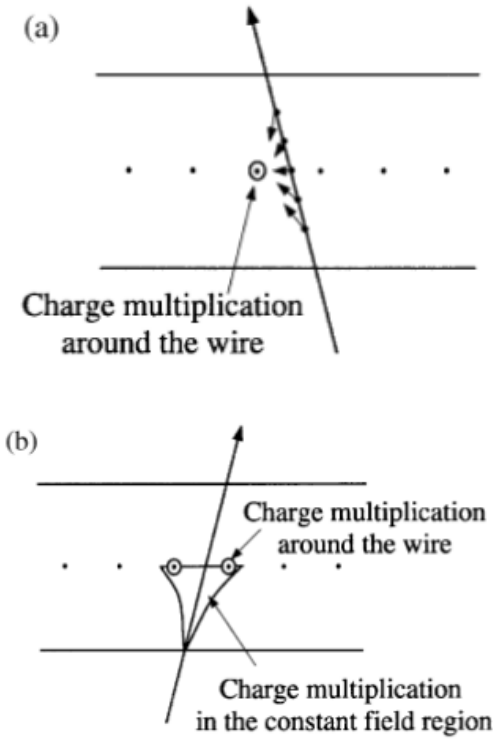

In typical MWPPAC detectors primary electrons, formed by the ionization of the gas due to the passage of an ion, are accelerated by the electric field between anode and cathode. If the electric field is high enough, the electrons may gain sufficient kinetic energy to ionize other neutral atoms of the gas (secondary ionization). This process can be repeated by the secondary electrons, eventually leading the ionization process to assume the form of a cascade, known as *Townsend avalanche* [99]. Depending on the reduced electric field E/p, the charge multiplication can occur mainly in the vicinity of the cathode wire, where the electric field is very high (Figure (a) on the left), or start when the electrons are still in the constant field region rather far from the wire (Figure (b) on the left). Once the geometry of the detector is fixed, the former case corresponds to high gas pressures (low E/p), the latter to low gas pressures (high E/p).

MWPPAC detectors typically reach timing and position resolutions of about 300 ps and 1 mm, respectively, with a very high ($> 80\%$) detection efficiency.

The IC

Ionization chambers (IC) are gas-filled detectors used for the detection of charged particles in many different types of experiment, thanks to features that may be attractive in various circumstances and may make them preferable with respect to semiconductor detectors. For instance they can be constructed with almost arbitrary size and geometry and the gas pressure can be modified according to the requirements of the experiment. Moreover they are far less subject to performance degradation due to radiation damage than semiconductor detectors [99].

The normal operation of IC is based on the collection of all the charges created by direct ionization within a gas through the application of an electric field. A fast heavy charged particle interacts with a gas mainly through Coulomb forces between its positive charge and the electrons of the absorber atoms. Such interaction progressively reduces its energy until it is completely stopped, eventually becoming a neutral atom. The rate at which ions lose their kinetic energy inside the gas (also called *stopping power*) can be calculated according to the Bethe formula [100]:

$$-\frac{dE}{dx} = \frac{4\pi e^2}{m_0}\frac{(qe)^2}{v^2}\ NZ\left[ln\left(\frac{2m_0v^2}{W}\right) - ln\left(1-\beta^2\right) - \beta^2\right] \tag{2.1}$$

where e and m_0 are the charge and rest mass of the electron respectively, qe and v the charge and the velocity of the primary particle, N and Z the number density and the atomic number of the absorber atoms, β is the ratio between the velocity of the ion and the velocity of light and W is an experimentally determined parameter which represents the average excitation and ionization potential of the absorber.

In the non-relativistic approximation the last two terms including β^2 can be neglected and equation 2.1 reduces to:

$$-\frac{dE}{dx} = A\ \frac{mq^2}{E_{kin}}\ ln\left(B\ \frac{E_{kin}}{m}\right) \tag{2.2}$$

where A and B are constants.

The energy released to the gas creates, along the track of the ionizing particle, a large number of electron-ion pairs. Since electrons have a drift velocity $\sim 10^3$ times higher than that of the positive ions, reflecting the ratio of their respective masses, what is then collected at the electrodes is essentially due to the electrons. In typical ionization chambers the field can have two different orientations with respect to the direction of the incoming ion: orthogonal (and we will speak of *transverse field chamber*) or parallel (*axial chamber*). An explicative drawing is reported in Figure 2.3.

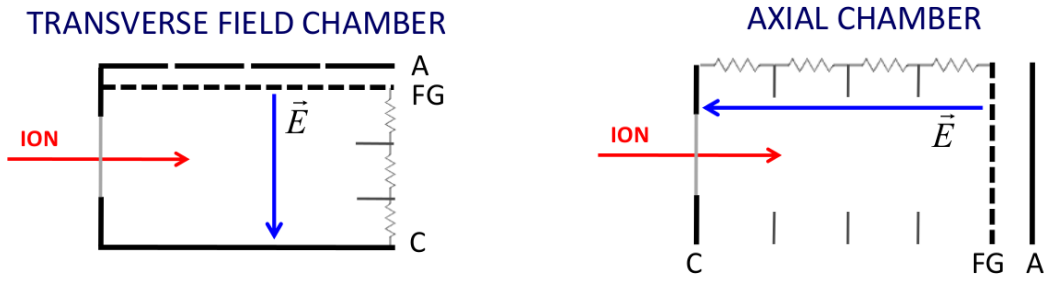

Figure 2.3.: Picture of a transverse-field chamber, where the electric field is orthogonal to the direction of the incoming ions (left), and of an axial-field chamber, where the electric field is parallel to the direction of the incoming ions (right).

In both kind of chambers fundamental is the presence of a Frisch grid (FG), which allows to make the amplitude of the signal (collected between the FG and the anode) independent on the entrance position of the ion in the chamber.

Transverse-field gas detectors, like for instance the ionization chamber of PRISMA (see Section 2.3.4), are usually operated as E-ΔE chambers. Their cathode and anode are divided into different sections, each one providing an independent ΔE signal. The sum of all these signals will determine the total energy lost by the ion in the chamber[1]. According to the Bohr's criterion [101], the average charge state $\bar{q}$, which can be calculated as a function of

[1] This is true only if the ion is completely stopped in the chamber, otherwise part of its energy is not measured.

the velocity and the atomic number of the ion, is proportional to $Z^{1/3}$. Inserting this in Eq. 2.2, one finds that the product of the differential (ΔE) and the total (E) energy losses is proportional to $mZ^{2/3}$.

Axial chambers, like for instance the second arm of PRISMA (see Section 2.4), operate following the principles of *Bragg Curve Spectroscopy* (BCS) [102]. The BCS is based on the principle that the amplitude of the Bragg peak (BP) of heavy ions in a stopping medium scales approximately as the atomic number Z of the ions. According to Bohr's picture, the interaction time of the ions with the atomic electrons of the stopping medium, as well as the energy loss, is maximum when the velocity of the ion is comparable to the average velocity of its electrons. When this happens the Bragg peak occurs. The anode signal is sent to a charge preamplifier and then split into two amplifiers: one operates with a longer shaping time, typically of the order of few microseconds, to integrate the whole charge produced by the passage of the ion and measure its total energy; the other operates with a shorter shaping time, of the order of hundreds of nanoseconds, to measure the amplitude of the BP. As this amplitude is independent on the ion energy, the method can be used, in principle, over a wide range of energy only limited by the gas pressure required to stop the ions in the detector and the energy threshold to produce the BP.

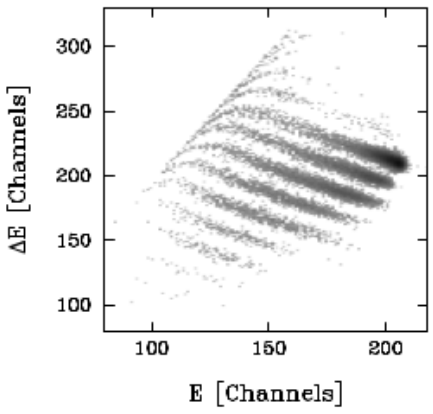

(a) Example of E-ΔE matrix for the reaction ^{40}Ca+^{208}Pb at E_{lab} = 235 MeV. Taken from Ref. [8].

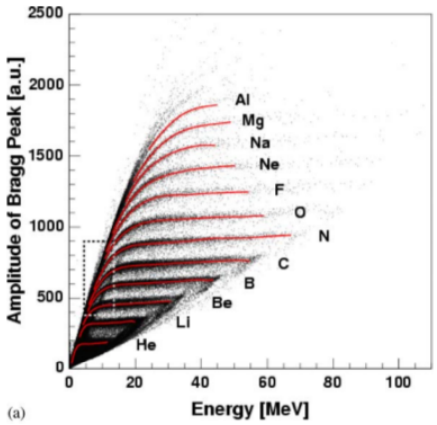

(b) Example of matrix BP amplitude vs energy for the reaction p+^{58}Ni at E_{lab} = 1.9 GeV. Taken from Ref. [103].

Figure 2.4.: Examples of a E-ΔE matrix produced with a transverse-field chamber (top) and of a matrix BP amplitude vs energy produced with an axial chamber (bottom).

Figure 2.4 shows an example of Z identification performed with the two types of ionization chamber described above. One can notice how the different nuclear charges are neatly separated. For both kind of chambers typical energy and Z resolutions for medium-mass ions at few MeV/A are 1% and 1.6%, respectively.

2.3. The PRISMA spectrometer

PRISMA [104–106] is a large acceptance magnetic spectrometer, designed for the detection of low-energy medium-mass reaction products (5-20 MeV/A) in heavy-ion collisions around the Coulomb barrier. The name "PRISMA" comes from the analogy with an optical prism, which decomposes the white light into the different wavelengths in the same way as PRISMA disperses the incoming ions according to their magnetic rigidity.

Other new-generation magnetic spectrometers of this kind are VAMOS in GANIL [107, 108] and MAGNEX in Catania [109]. All of them are based on the combination of simple magnetic elements and tracking methods for the reconstruction of the trajectory of the ions and their complete identification in nuclear charge and mass.

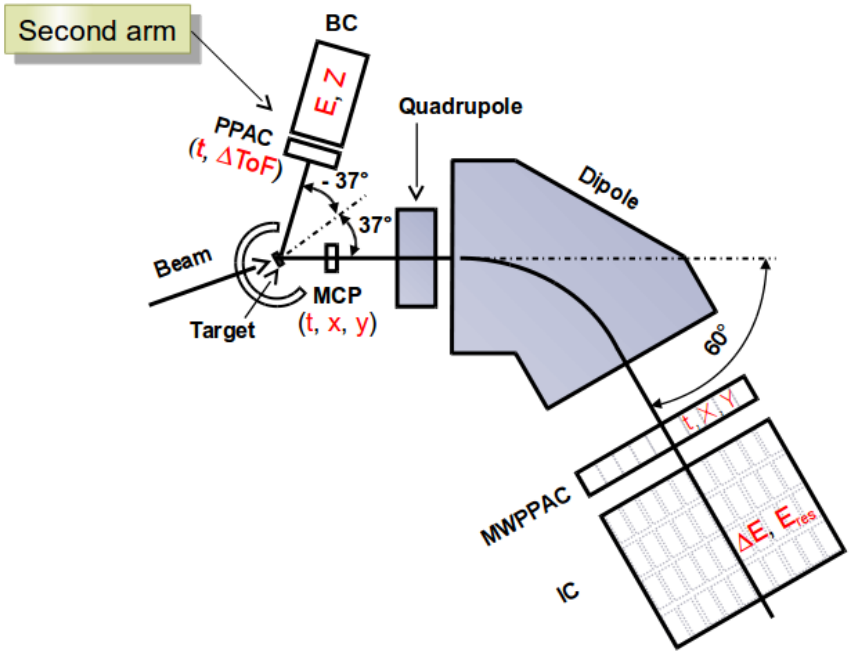

Figure 2.5.: Picture of the whole experimental apparatus (PRISMA + second arm) for the present experiment.

The main characteristics of PRISMA are reported in Table 2.1.

Solid angle Ω	80 msr
ΔA/A	1/250
ΔZ/Z	1/60
ΔE/E	1/1000
Δp/p	± 10%
Maximum Bρ	1.2 Tm
$\Delta\theta_{lab}$	±6°
Rate capability	100 kHz

Table 2.1.: Main characteristics of the PRISMA spectrometer.

PRISMA is composed of complex detector systems and two magnetic elements that deserve a more detailed description. In Figure 2.5 a picture of the whole experimental apparatus for the present experiment is reported. The different detectors composing PRISMA and the second arm will be described in this Chapter.

2.3.1. The Micro-Channel Plate detector of PRISMA

The entrance detector of PRISMA is a MCP detector [110] (see Section 2.2). It is placed at 25 cm from the target, rotated by an angle of 135° with respect to the optical axis of the spectrometer and provides timing and position information in the x and y directions, namely along and transversal to the dispersion plane, respectively. The active area of detection is 8×10 cm^2 and covers the whole solid angle of PRISMA. The carbon foil which generates the secondary electrons is 20 μg/cm^2 thick. Upstream the carbon foil is a cross-shaped mask with 5 reference points of known position for calibration purpose (see Section 4.2.1). The position resolution is 1 mm which corresponds to an angular resolution of less than 0.5°, while the time resolution is less than 350 ps. The efficiency is close to 100% for heavy ions at energies of few MeV/A.

Figure 2.6 shows a photograph (left) and a scheme (right) of the MCP detector of PRISMA.

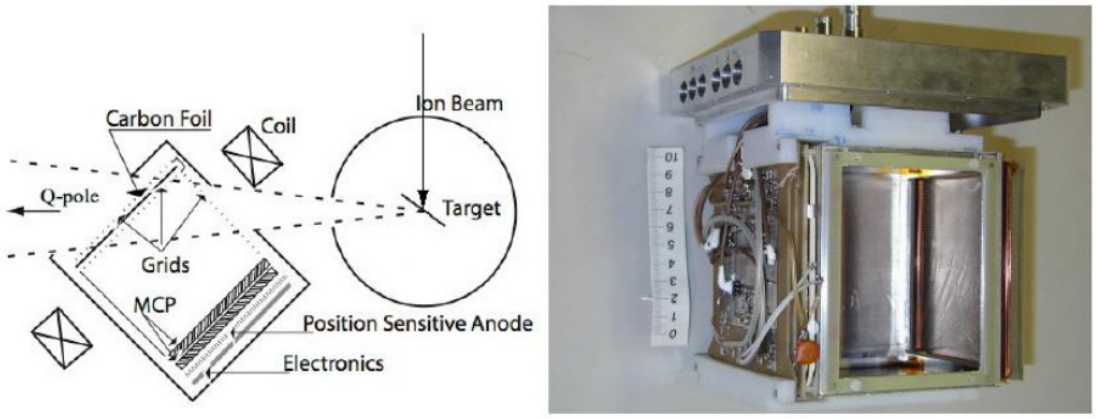

Figure 2.6.: A simple scheme (left) and a photograph (right) of the MCP detector of PRISMA. Taken from Ref. [110].

2.3.2. The magnetic elements of PRISMA

In their trajectory, immediately after the MCP the ions encounter two magnetic elements (first a quadrupole and then a dipole) which constitute the optical system of PRISMA. Their function is to focus on one axis, disperse on the other and bend the trajectory of the incoming particles to make them reach the focal plane detectors. It is important to know the geometric properties of the magnets and the value of the fields set in the experiment in order to obtain a good reconstruction of the ions trajectory.

Quadrupole It is mounted at a distance of 50 cm from the target and has a length of about 42 cm. As the magnetic field extends over the geometrical dimension of the magnet itself (fringing field), in the analysis of the experiment it has been necessary to slightly adjust these parameters. Its magnetic field is set to focus the ions in the vertical (y) direction and defocus them in the horizontal (x) one.

Dipole It is located 60 cm after the exit window of the quadrupole. Its function is to bend the incoming particles to the different positions in the focal plane detectors according to their magnetic rigidity. The bending angle is fixed at 60° with a curvature radius of 1.2 m. Since the maximum reachable magnetic field is 1 T, the maximum magnetic rigidity Bρ is 1.2 T·m.

2.3.3. The MWPPAC detector of PRISMA

The first focal plane detector passed by the particles, after about 3.2 m of drift in vacuum, is an array of MWPPAC [111] (see Section 2.2). It is 100 cm wide in the horizontal (x) direction and 13 cm wide in the vertical (y) direction; in the x direction it is segmented in 10 independent sections, or pads, each one with an active area of 10 × 13 cm^2.

Each section has a three-electrode structure: a central cathode polarized at high voltage (500-600 V) for timing and two orthogonal wire planes, placed at ground potential at 2.4 mm from the cathode, which provide x and y position information. The combined timing information of the MCP and MWPPAC detectors gives the Time-of-Flight (ToF) of the detected ions. Each pad has 100 wires placed in steps of 1 mm on the horizontal axis, for a total of 1000 wires for the whole detector. The position resolution in the x direction is 1 mm. The vertical axis is instead constituted of a single section that covers the entire length of the detector with a step of 1 mm between the wires. As the y direction is mostly used to ensure the scattering in the reaction plane, these wires are connected in groups of two, resulting in a position resolution of 2 mm.

A photograph and a three dimensional schematic view of the MWPPAC detector of PRISMA is depicted in Fig. 2.7.

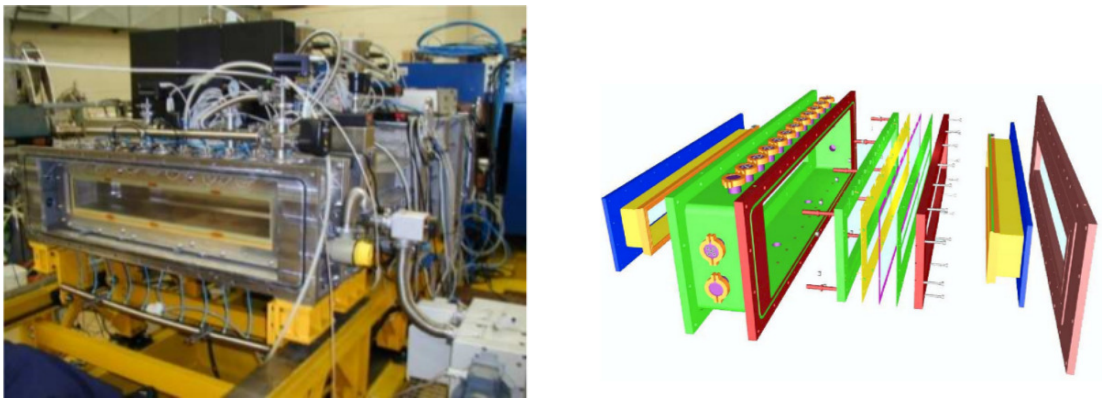

Figure 2.7.: A photograph (left) and a three dimensional view (right) of the MWPPAC detector. Taken from Ref. [111].

2.3.4. The IC detector of PRISMA

The MWPPAC detector is followed (60 cm downstream) by an IC [111]. Its dimensions are 110(x) × 20(y) cm^2 while the active depth (z) is 120 cm. This long depth allows to stop all the ions by using low working pressures, thus reducing the stress on the entrance mylar window which can stand a maximum pressure of around 100 mbar. The cathode and anode electrodes of the IC are composed of 40 pads (10 in the x direction times 4 in the z direction), each one having dimensions 265×99 mm^2 and acting as an independent ΔE section. The IC is usually operated with fast gases, such as carbon tetrafluoride (CF_4) or high-purity methane (CH_4), in order to preserve a good energy resolution even with the high counting rates (several kHz per section) needed in typical experiments with PRISMA. The CF_4, for his higher stopping power, is used when dealing with very energetic ions.

A three dimensional picture of the IC detector of PRISMA can be seen in Fig. 2.8.

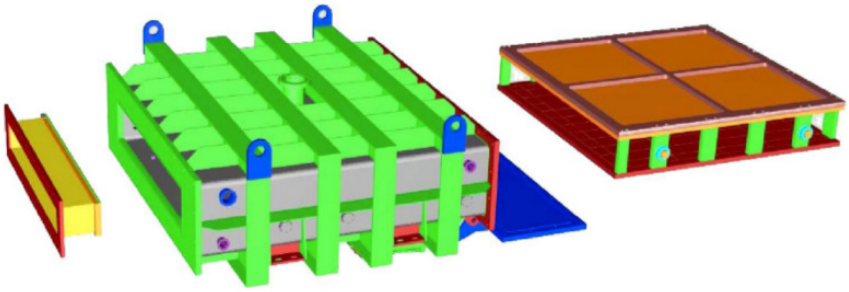

Figure 2.8.: Schematic layout of the IC detector of PRISMA. Taken from Ref. [111].

2.4. The second arm of PRISMA

In the experiment subject of this work PRISMA operated in conjunction with a new device, acting as a *second arm*, in a kinematic coincidence configuration. It consists of a position sensitive Parallel-Plate Avalanche Counter (PPAC) followed by an axial ionization chamber, namely a Bragg Chamber (BC). A photograph of the device is reported in Figure 2.9.

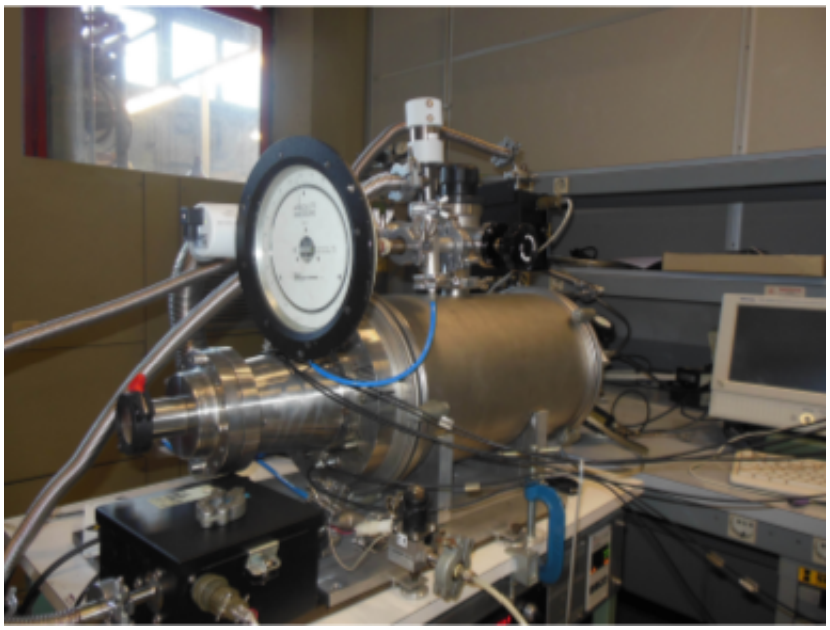

Figure 2.9.: Photograph of the second arm of PRISMA. The big cylinder contains the active volume of the BC.

2.4.1. The PPAC of the second arm

The PPAC [112] has an active area of 10 × 10 cm^2 and is composed of a central cathode and two anode planes orthogonally oriented on each side at a distance of 2 mm. The cathode is made of a double aluminized (20 $\mu g/cm^2$ + 20 $\mu g/cm^2$) mylar foil with a thickness of 1.5 μm. The anode planes consist of 10 μm diameter gold-plated tungsten wires with 1 mm spacing. Four timing signals from the anode planes (x_l, x_r, y_u and y_d) are used to reconstruct the x and y position information from the delay measurement x_l vs x_r and y_u vs y_d. The total delay of each wire plane (x and y) amounts to 100 ns. Moreover, the cathode provides a timing signal for ToF measurements.

2.4.2. The BC of the second arm

The vacuum vessel of the BC is a stainless steel cylinder 37 cm long with 25 cm internal diameter. The entrance window, also acting as cathode of the ionization chamber, is an aluminized (20 $\mu g/cm^2$) mylar foil (1.5 μm) with a diameter of 10 cm. The active depth of the detector is 33 cm. To shield the anode from the induced charge due to movement of electrons and positive ions in the drift volume, a Frisch grid (FG) was mounted at 2 cm from the anode. The uniformity of the electric field in the cathode-FG region is obtained by means

of 114 guard rings. The Z identification inside the BC is performed with the BCS technique described in Section 2.2. A photograph of the PPAC and the BC is reported in Figure 2.10.

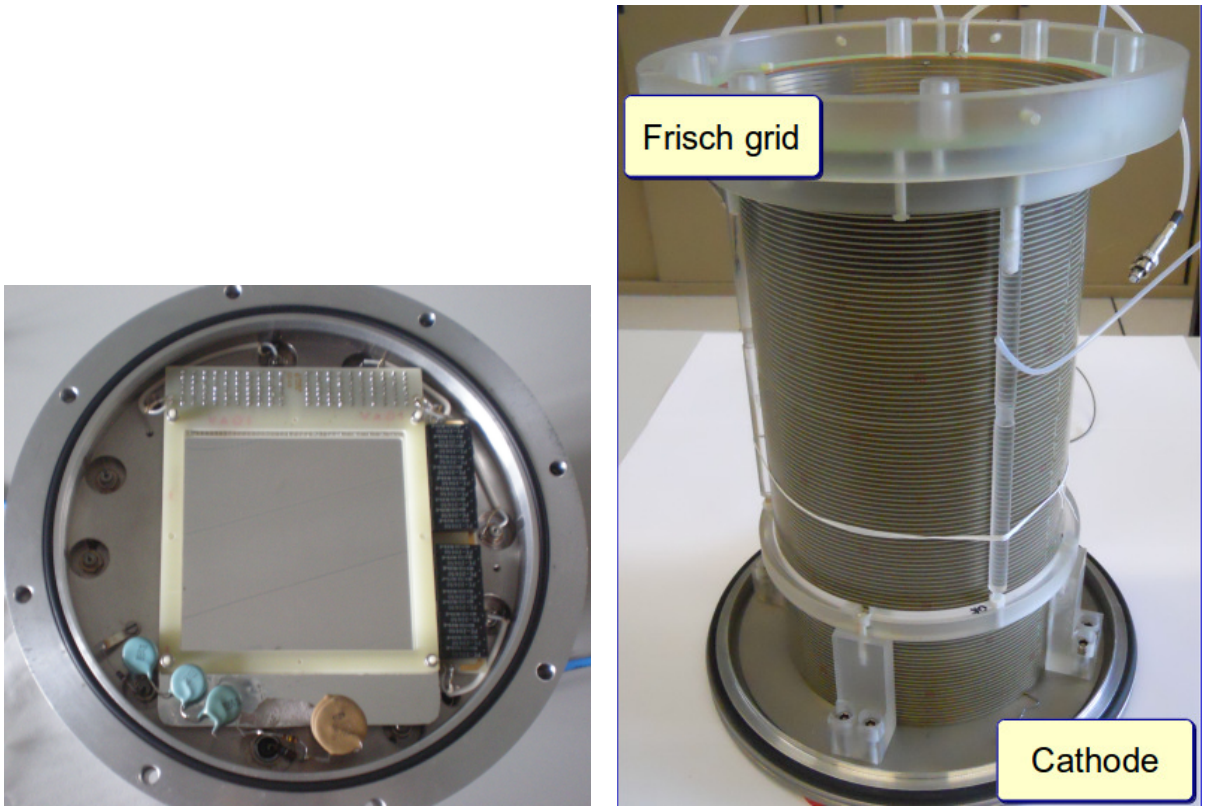

Figure 2.10.: A photograph of the PPAC of the second arm (left) and of the inner parts of the BC (right) where the guard rings and the Frisch grid are visible.

3 Tests of the second arm

Preliminary laboratory and in-beam tests were carried out to determine the performance of the second arm and to fully characterize the detector. For the laboratory tests a α source and a standard analog readout chain were used. For the successive in-beam tests both analog and digital electronics were employed. In this Section we will present the main results of these tests and some interesting outcomes concerning the analysis of the digital signal.

3.1. Tests with analog electronics

3.1.1. Laboratory tests

The laboratory tests of the detector were performed using α particles from a triple α source (^{239}Pu, ^{241}Am, ^{244}Cm). Analog electronics was used to process the BC signals: a charge sensitive preamplifier followed by two amplifiers working in parallel, with different shaping times: 4 μs for energy information and 0.5 μs or 0.25 μs to measure the Bragg peak amplitude.

The cathode signal of the PPAC was sent to a home-made fast amplifier with a gain of 250 and differentiating and integrating constants of 10 ns. Anode signals were processed through fast amplifiers and then sent to commercial Constant Fraction Discriminators (CFD). The position information is obtained by measuring through a Time-to-Amplitude-Converters (TAC) the time difference between the signals from the end of the delay lines (x_l and x_r, y_u and y_d). Figure 3.1 shows the scheme of the electronics layout used in the laboratory tests. We remind that this configuration is valid only for the tests described in this Chapter. In the experiment discussed in the thesis the master trigger was always given by PRISMA and the second arm operated in slave mode.

The bias voltage of the cathode was set to maximize the detector efficiency, which turned out to be close to 100% for α particles. The efficiency was determined by comparing the PPAC and the BC spectra (in these tests the anode signal from the BC was used as master trigger of the data acquisition system). In these working conditions the cathode exhibits a signal with a pulse height of about 500 mV and a rise time of approximately 10 ns (upper panel of Figure 3.2), mainly due to the short integration time of the home-made fast amplifier.

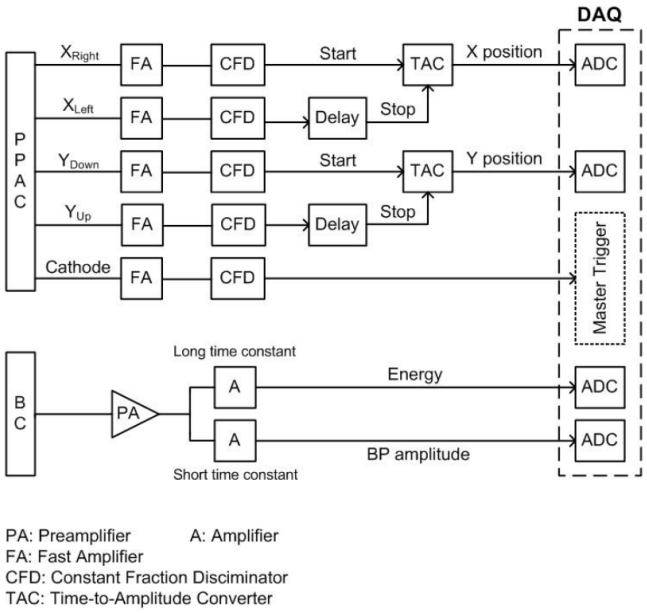

Figure 3.1.: Schematic layout of the electronics used in the laboratory tests.

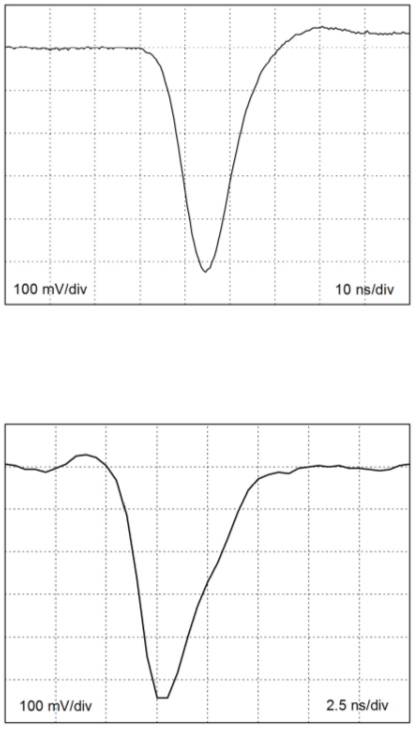

Figure 3.2.: PPAC signals from cathode (top) and x anode plane (bottom) as seen on a digital oscilloscope.

Because of the attenuation of the delay lines, the signal amplitudes of the anode wire planes range from 30 to about 500 mV with a rise time of about 2 ns (lower panel of Figure 3.2). Different wires show up as different peaks in the position spectra. Consequently, the spatial resolution of the PPAC, mainly given by the wire spacing, is 1 mm for both X and Y planes.

The BC was filled with CF_4 at a pressure of 60 mbar in order to stop α particles into the active depth of the detector. The reduced electric fields E/p between cathode and FG and between FG and anode were set in order to have a high electron drift velocity (about 8-10 cm/μs) and minimize the screening inefficiency of the FG.

As the calibration α source was not collimated, only events corresponding to the central portion of the position spectra (x and y) of the PPAC were selected for the BC in order to reject signals due to α particles which hit the guard rings. Figure 3.3 shows the three peaks corresponding to the α particles emitted by the triple source at energies of 5.155 MeV (^{239}Pu), 5.486 MeV (^{241}Am) and 5.805 MeV (^{244}Cm). The energy resolution turned out to be $\Delta E/E \sim 1.8\%$.

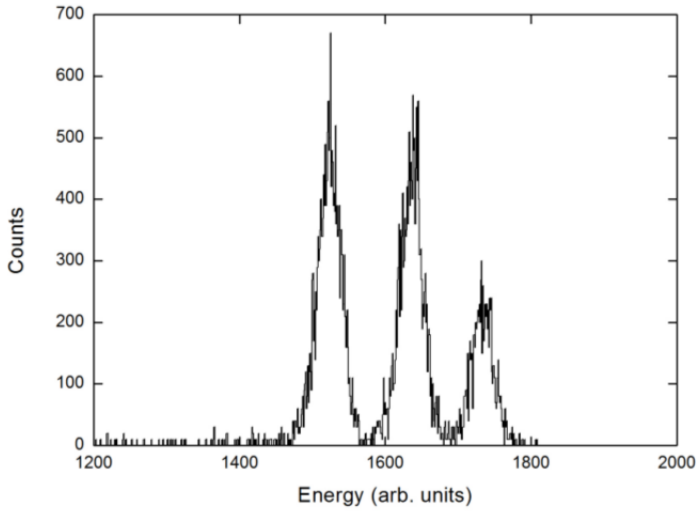

Figure 3.3.: Energy spectrum measured with a triple α source in laboratory tests of the second arm.

3.1.2. In-beam tests with analog electronics

The detection system was also tested with heavy ions at the Tandem-ALPI accelerator complex of LNL using ^{32}S and ^{58}Ni beams impinging on different targets:

- ^{197}Au (150 μg/cm^2);
- ^{96}Zr (200 μg/cm^2 of $^{96}Zr_2O_3$ on 20 μg/cm^2 carbon backing);
- ^{208}Pb (200 μg/cm^2 on 20 μg/cm^2 carbon backing)

The set-up was mounted on the sliding seal scattering chamber of the electrostatic deflector PISOLO and placed at $\theta_{lab} = 65°$ and 75° with respect to the beam direction. The electronics

used to process the signals from BC and PPAC were the same as in the laboratory tests. A MCP detector, installed at 15 cm of distance from the target, also allowed to get a start signal for ToF measurements. The opening angle of the second arm, placed at 115 cm from the target, was $\sim 5°$ and the gas detectors operated with a maximum counting rate of about 2 kHz.

Figure 3.4 displays, as an example, the x and y position spectra of the PPAC for the ^{32}S+^{96}Zr reaction at E_{lab} = 120 MeV.

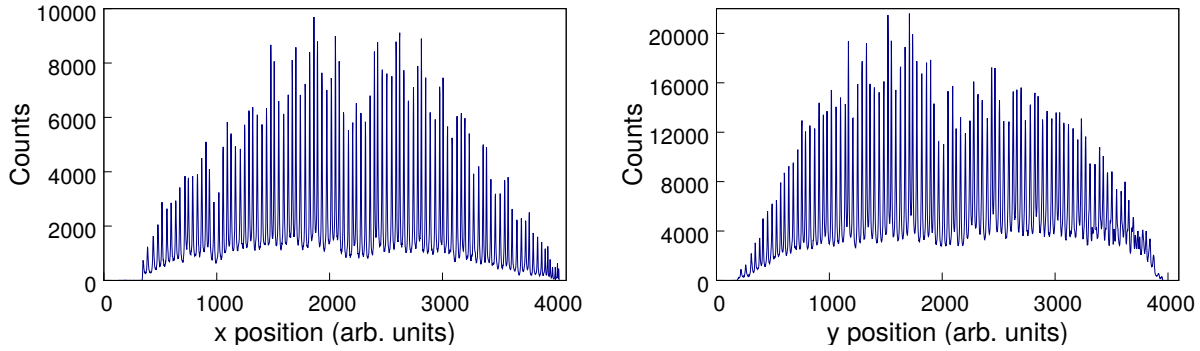

Figure 3.4.: x (left) and y (right) position spectra of the PPAC for the ^{32}S+^{96}Zr reaction at E_{lab} = 120 MeV. The missing counts at $\sim$ 2000 arb. units for both x and y spectra are due to the presence of a mask placed in front of the PPAC for calibration purposes.

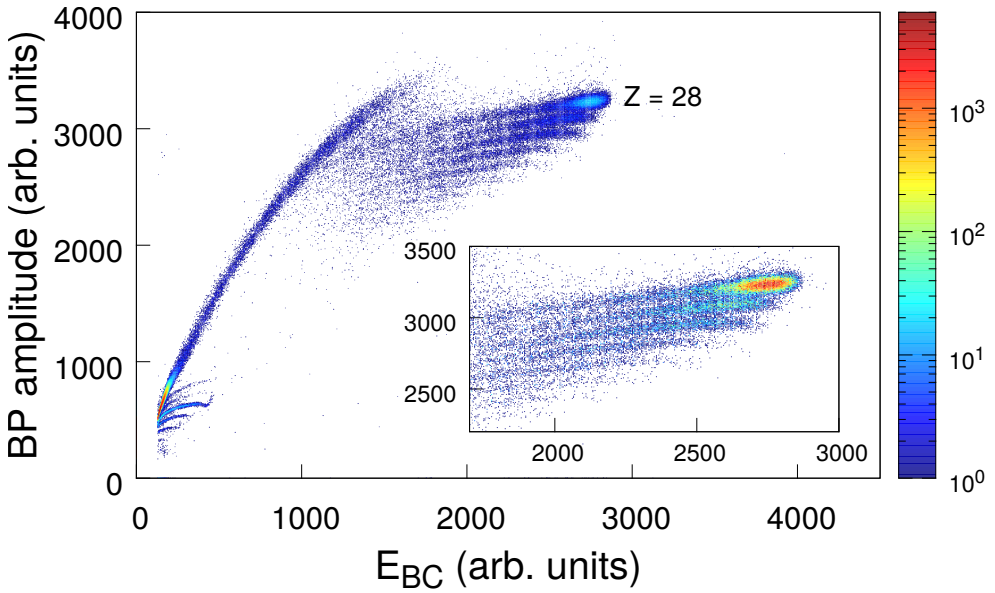

Figure 3.5.: Two-dimensional scatter plot Bragg peak amplitude vs energy measured with the BC for the reaction ^{58}Ni+^{208}Pb at E_{lab} = 400 MeV and θ_{lab} = 65°, using analog electronics.

The BC was operated with CF_4 at pressures of 70, 87 and 100 hPa, depending on the reaction involved. Fragments produced in the reactions ^{58}Ni+^{208}Pb at E_{lab} = 400 MeV were used to estimate the Z resolving power. The result was $\Delta Z/Z \sim 1/50$ around Z = 28. Figure 3.5 shows the matrix BP amplitude vs energy for this reaction, where different proton stripping channel from Ni are visible (in the insert).

3.2. In-beam tests with digital electronics

Digital electronics was also tested for the processing of the BC signal. In particular, the output signal from the charge preamplifier was sent to a CAEN Digitizer V1724 (14-bit resolution, 100 MS/s of sampling rate, 2.25 V_{pp} of dynamic range). The algorithms for the analysis of the signal from the BC were elaborated using the *pClasses*, a library of classes simulating the components of a digitizing system, developed in the ROOT Data Analysis framework [113, 114].

Figure 3.6 shows typical signal shapes from the charge preamplifier (black) and the CR-RC filters applied for energy and Bragg peak amplitude determination.

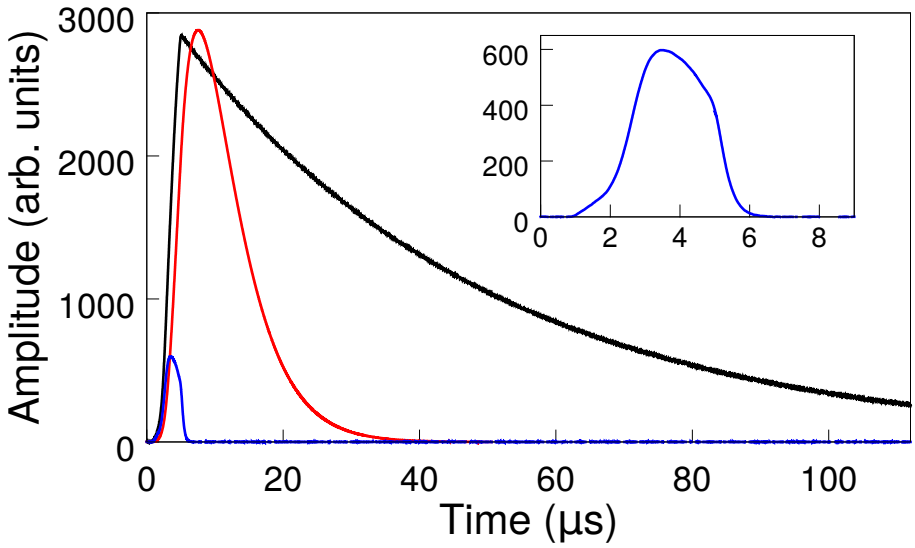

Figure 3.6.: Digitized signal coming from the preamplifier of the BC (black) together with the semigaussian filter with a shaping time of 4 μs for energy determination (red), and the semigaussian filter with a shaping time of 250 ns representing the Bragg curve (blue). The latter is visible in larger scale in the insert.

These semigaussian filters are applied after the subtraction of the baseline of the preamplifier signal and are provided with a pole-zero cancellation algorithm. The long filter (red) has a time constant τ_E = 4 μs to measure the total energy released by the ion in the chamber. The short filter (blue) has a time constant τ_{BP} = 250 ns to measure the amplitude of the BP. We chose these specific values because τ_E represents the time needed by the electrons produced by an incoming ion to cover the active depth of the chamber (33 cm) and to be fully collected, while τ_{BP} is the time needed by the electrons to cover the distance between

the FG and the anode (2 cm). The value of the Bragg peak amplitude for each event is taken as the maximum of the short CR-RC filter.

Among the advantages of employing digital electronics is the possibility to store and visualize the signal and perform different operations on it. We could indeed study in a systematic way the dependence of the Z resolution on the shaping constant of the short filter, τ_{BP}. For each time constant chosen (in the range 50-300 ns) the values of energy E_{BC} and BP amplitude obtained were used to construct bidimensional spectra Bragg peak amplitude vs energy, as shown in Figure 3.7 for the case of $\tau_{BP} = 250$ ns. From a quick comparison between the inserts of Figures 3.5 and 3.7 one can immediately infer the higher performance of the digital system in terms of Z resolution.

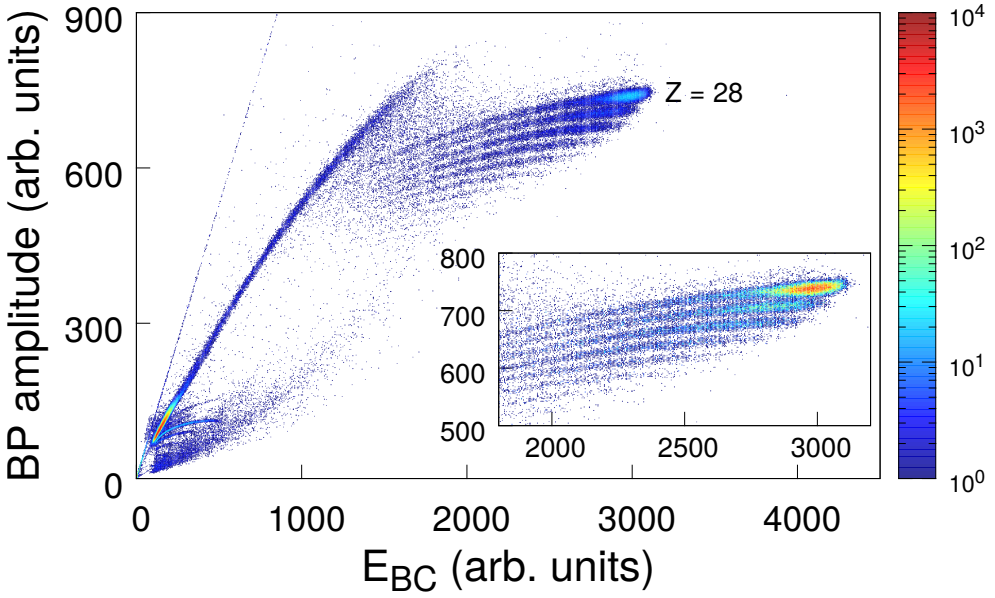

Figure 3.7.: Two-dimensional scatter plot Bragg peak amplitude vs energy measured with the BC for the reaction ^{58}Ni+^{208}Pb at $E_{lab} = 400$ MeV and $\theta_{lab} = 65°$, using digital electronics.

The small dependence of the BP height on the energy for a given Z, resulting in a non-horizontal alignment in the matrix of the structures corresponding to different atomic numbers can be attributed to a small FG inefficiency, as pointed out in Ref. [115]. To determine the Z resolution of the BC we have to align these structures before projecting on the y axis. A routine was developed in order to correct, in an empirical way, the dependency of the BP amplitude on the energy for each gate on Z. Figure 3.8 shows, as an example, the aligned matrix BP amplitude vs energy (left) for $\tau_{BP} = 250$ ns and the projection on the y axis with the multigaussian fit used to determine the Z resolution.

In Figure 3.9 the dependency of the Z resolving power on τ_{BP} is plotted. The trend is almost monotonically increasing but around $\tau_{BP} \sim 200$ ns a plateau is reached around a value $Z/\Delta Z \sim 60$ (for $Z \sim 28$).

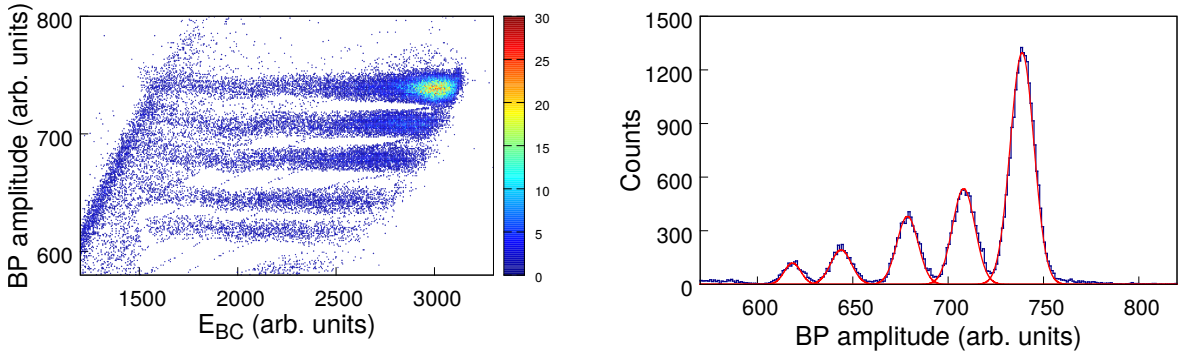

Figure 3.8.: Aligned matrix BP amplitude vs energy (left) and projection on the y axis with the multigaussian fit used to determine the Z resolution (right)

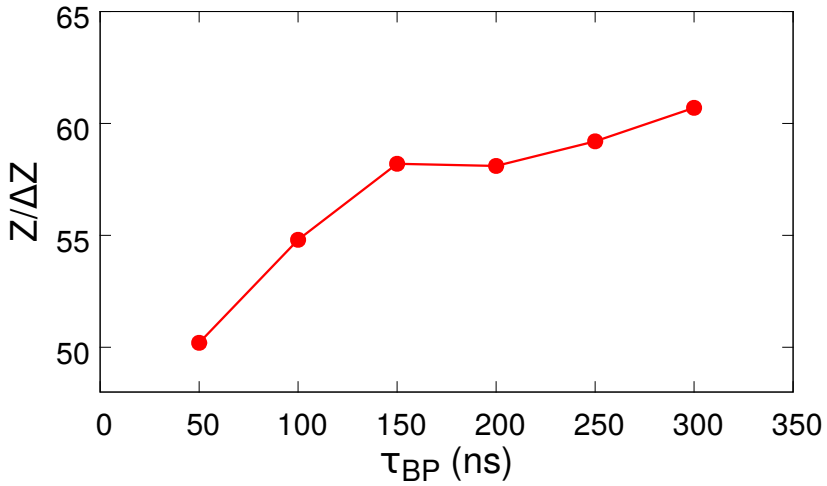

Figure 3.9.: Plot of the resolving power for different shaping times of the short filter τ_{BP}. The red lines are to guide the eye. The errors in the plot are only statistical and do not exceed the size of the points.

For higher shaping times the resolution remains close to this value, although slightly increasing. One could then be led to believe that the best choice for τ_{BP} is a value higher than 300 ns. Nevertheless, increasing τ_{BP}, the Z structures in the matrix BP amplitude vs energy start to bend more and more, approaching the diagonal bisecting the graph. This is of course a consequence of integrating for a longer time interval than the one needed by the electrons to cover the distance between the FG and the anode. In these conditions, although the signal-to-noise ratio increases and the resolving power remains good, the Bragg curve begins to lose its usual shape and the Z identification at low energies becomes more and more difficult. Therefore for usual operations of the BC we consider a wiser choice to use shaping times around 250-300 ns for the short filter in order to keep a good Z resolution and at the same time a good identification also at lower energies.

We conclude this Section by showing some instructive plots that confirm the right operation of the algorithm used to shape the BC signal and the power of the digital systems in terms

of the number of operations it allows to perform on the signal.

Figure 3.10 shows the Bragg curves measured (with τ_{BP} = 250 ns) for fragments with different atomic numbers Z, obtained by setting a thin gate on the energy and looking at the correspondent Bragg curves for different gates on proton stripping channels. The upper insert of Figure 3.10 displays the difference in the BP height for fragments with different atomic numbers. One can also see in the lower insert that the higher is the atomic number of the ion the lower is the time needed for the collection of the charge (length of the Bragg curve), which is related to the range of the ion in the chamber.

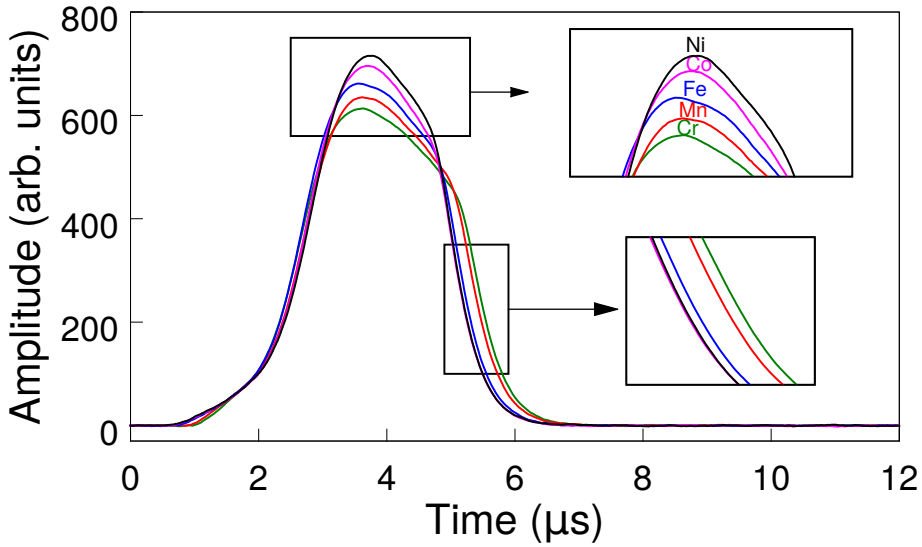

Figure 3.10.: Bragg curves for ions with different Z and very similar energy. Upper insert: zoom on the Bragg peaks and identification of the specific element detected. Lower insert: zoom on the tail of the Bragg curve to highlight the difference in charge collection time for different atomic numbers.

In the in-beam tests with digital electronics here discussed the signals from the PPAC were not included in the digitizer. This prevented us to extract the range of the ions inside the BC. One could anyway relate the temporal length Δt_{BC} of the Bragg curve to the range of the ions. Δt_{BC} is in fact related to the total time needed by the anode to collect the electrons produced in the ionization process by the incoming ion and this time is also related to the energy (and the range) of the ion. We determined Δt_{BC} by applying a Constant Fraction Discriminator (CFD) to the rising and falling part of the Bragg curve; the start and stop value of the curve were taken at the 10% of the rising and falling times, respectively. Figure 3.11 illustrates the relation between the energy and the charge collection time. On the left panel one can see a matrix E_{BC} versus Δt_{BC} where the proportionality between the two quantities shows up; the figure on the right panel has been obtained by setting a gate on a specific nuclear charge in the matrix of Figure 3.7 and plotting the Bragg curves relative to different ranges of energy E_0-E_4, from 1900 to 2900 arb. units, in steps of 200 arb. units. It is evident that the higher is the energy of the ion the longer is the temporal length of the Bragg curve.

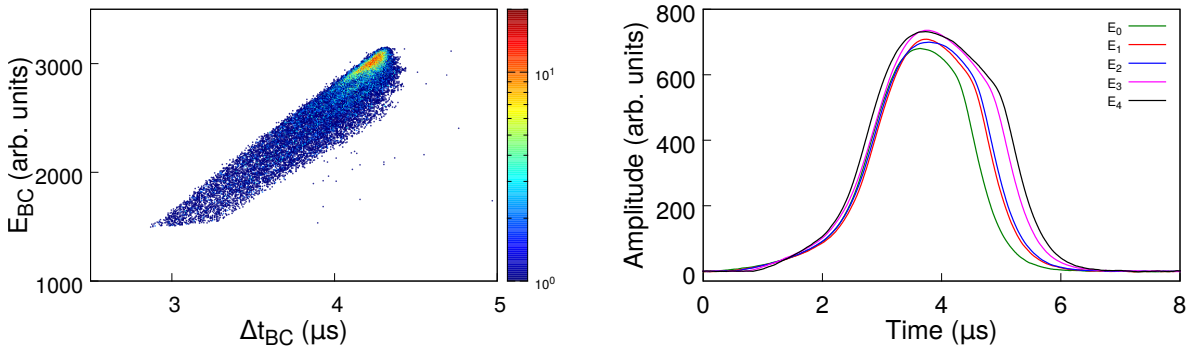

Figure 3.11.: Matrix E_{BC} vs charge collection time Δt_{BC} (left) and Bragg curves (right) relative to the same gate on Z but different ranges of energy E_0-E_4, from 1900 to 2900 arb. units, in steps of 200 arb. units.

In forthcoming tests the possibility to add the PPAC information to the DAQ will allow to extract the true range of the ions. This can be obtained by taking the fast signal from the cathode of the PPAC (see Figure 3.2) as start and the anode signal of the BC as stop. The additional information on the range will provide more details on the nature of the reaction products.

In conclusion, the comparison between in-beam tests performed using analog and digital electronics has pointed out that the use of digital electronics could entail relevant improvement in the Z resolving power and add important information (range, shape of the Bragg curve, etc.) that could not be extracted in a simple way with the usual analog system. On the other hand the implementation of the digitizer in the DAQ is not straightforward, therefore additional work is required to have the system operating for future experiments.

4 Analysis of PRISMA data

In this Chapter we will present the main steps of the procedure that was followed to analyze the data collected with PRISMA, from the calibration of the different detectors to extract the relevant physical information to the final spectra whence we could determine the absolute yields of transfer products and derive the TKEL distributions for Te isotopes. The additional physical quantities measured with the second arm will be presented in Chapter 5.

The raw files from the PRISMA data acquisition (DAQ) system are converted into a proper format for the following analysis using the *femul* package [116]. In the converted files the information coming from the VME crates connected to the different PRISMA detectors are stored in an array. The position of each channel in the array is encoded by a map reported in the so-called *Look-Up Table* (LUT), which relates each channel of the ADC to the corresponding detector. Files converted with *femul* can be analyzed with the *Gammaware* package [117] or similar software. For the present work the ROOT Data Analysis software [113, 114] was employed. We used an already existing version of the software *fastWatchers* [118] and modified it when necessary. FastWatchers feeds the converted files to the *PRISMA libraries* [119], a set of C++ classes initially developed by A. Latina and E. Farnea to analyze PRISMA data, and returns a ROOT tree which contains the relevant information. This tree can be further analyzed with macros created in the ROOT Data Analysis framework.

4.1. The experiment: ^{197}Au+^{130}Te @ 1070 MeV

The experiment presented in this work was performed at the Laboratori Nazionali of Legnaro [120]. A beam of ^{197}Au was accelerated with an energy of 1.07 GeV ($\sim$ 5.5 MeV per nucleon, just $\sim$ 4% above the Bass barrier) by the PIAVE-ALPI accelerator complex and delivered onto a 200 μg/cm^2 (2 mm strip) ^{130}Te target with a purity of 99.6%. To reduce the sputtering effects on the target surface, the Te material was sandwiched between 20 μg/cm^2 C layers. PRISMA was placed at the corresponding grazing angle $\theta_{gr} = 37°$ in the laboratory system, while the second arm at the kinematically correlated angle of -37°. A photograph of the target area, taken before the experiment, is reported in Figure 4.1. In this configuration Te-like recoils entering PRISMA had energies of $\sim$ 5.5 MeV/A, while those of Au-like ions entering into the coincident arm had energies of $\sim$ 2 MeV/A.

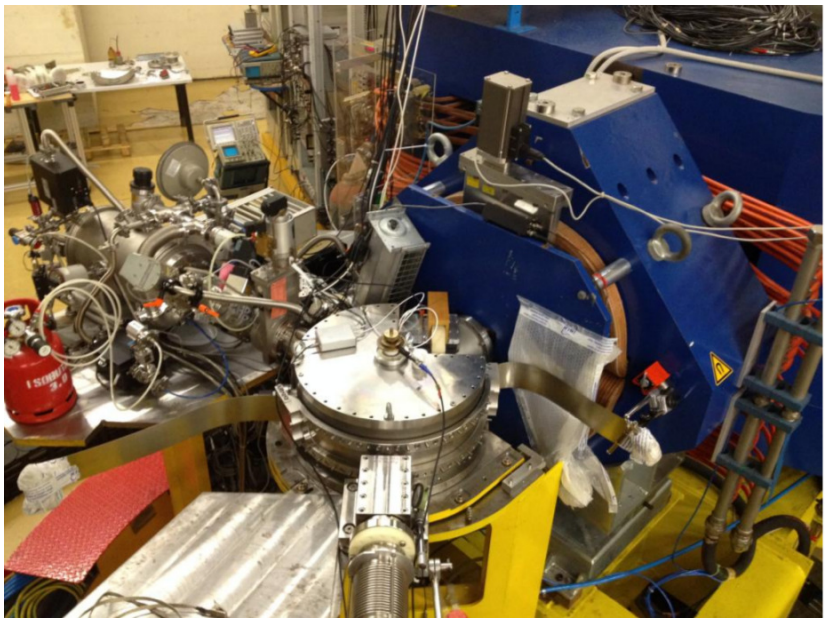

Figure 4.1.: Photograph of the target area for the present experiment. On the right the quadrupole of PRISMA is visible, on the left the second arm; below the sliding-seal scattering chamber is the beam-line.

For most of the collected data the magnetic fields and the gas pressure in the IC of PRISMA were optimized to detect the light partner of the reaction, while the gas pressure in the second arm was set in order to fully stop the heavy (Au-like) fragments. This choice is due to the fact that only in PRISMA we have enough A and Z resolution to resolve neutron- and proton-transfer channels for Te-like ions. The set parameters for the present experiment are reported in Table 4.1.

Quadrupole field	0.782 T
Dipole field	0.850 T
PRISMA IC pressure	91-96 mbar
BC pressure	52.7 mbar

Table 4.1.: Settings of the magnetic fields in PRISMA and the pressures of the ionization chambers for the present experiment.

PRISMA and the second arm were connected to a sliding seal scattering chamber (1 m diameter) inside which two monitor detectors of silicon surface barrier type were placed at $\theta_{\mathrm{lab}} = 61°$ and $\theta_{\mathrm{lab}} = 71°$. The monitors were used to detect Rutherford scattered Te ions for relative normalization between different runs and to control the beam conditions during the measurements. We remind that in inverse kinematics the conditions to have an almost pure Rutherford scattering are met at backward angles (which correspond to forward angles in direct kinematics). For completeness, we also mention that the presence of a limiting angle $\theta_{\mathrm{lim}} = 41°$ for Au-like ions in the present experiment prevents them to reach the monitors.

4.2. Presorting of PRISMA data

PRISMA allows to identify the incoming ions in velocity β, atomic number Z, atomic charge state q and mass A, combining the information coming from the different detectors of which it is composed and which were described in Section 2.3.

1. **Velocity** β. The ions velocity $\beta = \mathrm{v/c}$ is proportional to the ratio between the total length of PRISMA and the measured ToF between the entrance MCP and the MW-PPAC focal plane detector. The trajectory length is calculated on an event-by-event basis, as described in Section 4.2.4.

2. **Atomic number Z**. The atomic number of the ions is measured in the ionization chamber with the E-ΔE method, as described in Section 2.2.

3. **Charge state q**. After selecting a given atomic number, the atomic charge state q can be extracted using the following relation:

$$E_{\mathrm{kin}} = \mathrm{kq}\beta\rho \tag{4.1}$$

   where ρ is the bending radius in the dipole magnetic field, E_{kin} the kinetic energy of the ion measured in the IC and k is a constant. By plotting E_{kin} versus the product $\beta\rho$ one can see the different charge states as straight bands.

4. **Mass A**. For each band (charge state) identified one can obtain an A/q spectrum and, by attributing a correct value of q to each band, integrate over all the charge states to extract a mass spectrum for each element produced in the reaction.

We will now give more details about the calibration procedure for each detector of PRISMA and the analysis of data to obtain the quantities described above; in Section 5.1 a similar procedure for the second arm will be described.

4.2.1. MCP start detector

The entrance MCP detector of PRISMA was described in Section 2.3.1. A proper calibration of its position information is necessary to obtain the true interaction point (x, y) of the incoming ion and determine the velocity vector of the scattered ions event by event. Figure 4.2 (left) shows the bidimensional spectrum of the x and y raw positions on the MCP as they are returned by the ADC. The five reference points of the cross-shaped mask are visible.

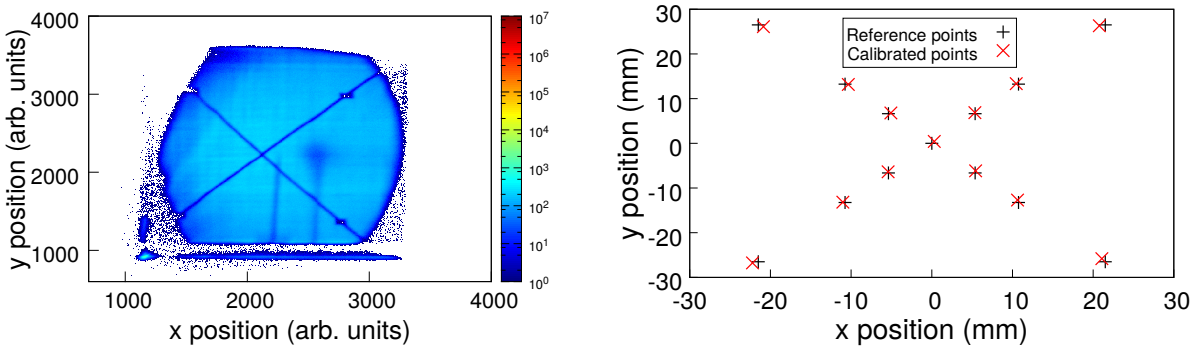

Figure 4.2.: Matrix y vs x raw position of the MCP detector of PRISMA (left) and calibration plot (right).

The calibration procedure is performed with a mixed linear calibration of x and y coordinates to take into account possible deformations of the surface, using the matrix method described in Ref. [121]. First the raw coordinates are "stretched" by multiplying them for a coefficient matrix where the diagonal elements are fixed to 1:

$$\begin{pmatrix} x' \\ y' \end{pmatrix} = \begin{pmatrix} 1 & a \\ b & 1 \end{pmatrix} \begin{pmatrix} x_{raw} \\ y_{raw} \end{pmatrix} \quad .$$

Then the transformed coordinates are calibrated from channels to millimeters by means of quadratic (x) or linear (y) polynomials.

$$\begin{aligned} x'' &= A_x + B_x x' + C_x x'^2 \\ y'' &= A_y + B_y y' \end{aligned}$$

Finally a rotation of $\theta = 45°$ is applied to account for the orientation of the MCP with respect to the optical axis.

$$\begin{pmatrix} x_{cal} \\ y_{cal} \end{pmatrix} = \begin{pmatrix} \cos\theta & \sin\theta \\ -\sin\theta & \cos\theta \end{pmatrix} \begin{pmatrix} x'' \\ y'' \end{pmatrix}$$

It is clear from this discussion that the number of parameters to be determined in the calibration procedure (a, b, A_x, B_x, C_x, A_y, B_y) is larger than the number of reference points (5), therefore additional points in between the center of the cross and the other reference points were used. The value of the parameters was then obtained from a least-square fit of the distance between the reference and the calibrated points. The final agreement is quite satisfactory, as visible in the right panel of Figure 4.2.

After setting a gate to eliminate the spurious signals, we could finally obtain the position distribution of the ions detected by the MCP in calibrated coordinates, both cartesian and polar (Figure 4.3). The transformation to polar coordinates was performed according to the equations in Appendix A of Ref. [122].

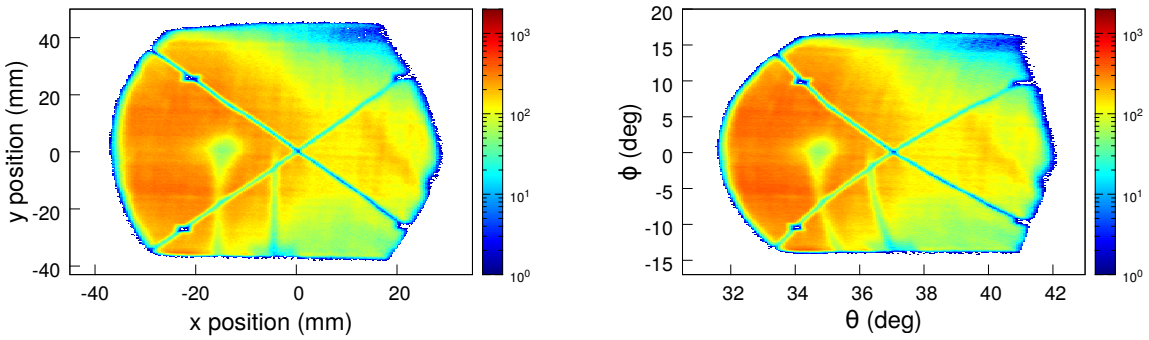

Figure 4.3.: Bidimensional spectra of the calibrated MCP in carthesian (left) and polar (right) coordinates. The cross-shaped mask and the two screws for calibration purpose are visible.

4.2.2. The MWPPAC detector

The MWPPAC focal plane detector of PRISMA was described in Section 2.3.3. There are 50 different signals as output of this detector, 5 signals for each of its 10 sections:

- y_U: y up position;
- y_D: y down position;
- x_R: x right position;
- x_L: x left position;
- x_C: cathode signal;

The cathode signal is also sent to a TAC to measure the Time-of-Flight of the detected ions from the MCP and the MWPPAC detectors.

Position information from the MWPPAC detector

The first two signals, relative to the y position information, are common to all the sections and are used mainly to check the centering of the beam. The combination of the x_R, x_L and x_C signals allows to obtain the position x_{fp} of the detected ions on the focal plane, which is very important for the reconstruction of their trajectory and mass-over-charge ratio. In particular this position is extracted from subtraction between right and left signals.

$$x_{fp} = x_R - x_L \tag{4.2}$$

If one of the two signals is partially or totally missing, it can be reconstructed from the relation:

$$x_C = x_R + x_L \tag{4.3}$$

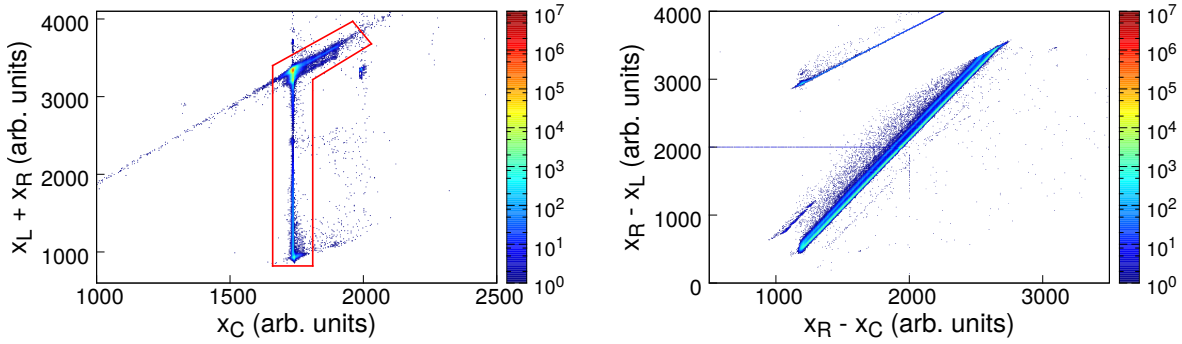

Figure 4.4.: Matrices x_L+x_R versus x_C (left) for one of the central pads of the MWPPAC with a polygonal gate applied to eliminate the noise contribution and $x_R - x_L$ versus $x_R - x_C$ (right) for the same pad for calibration purpose (see text for details).

In order to eliminate the "noise" contribution a polygonal gate, like the one visible in the left panel of Figure 4.4, was applied for each one of the 10 pads. In an ideal detector the matrix x_L+x_R versus x_C should show a simple point structure, according to Eq. 4.3; in a real detector it can happen that for some events the two anodes collect less charge than the cathode. This is reflected, in the matrix of Figure 4.4, in the presence of a vertical structure extending towards lower values of x_L+x_R. The associated events were not rejected in the analysis procedure but instead recovered with a simple calibration procedure where the cathode signal is related to the right and left signals, respectively. The right panel of Figure 4.4 shows the bidimensional plot of $x_R - x_L$ versus $x_R - x_C$ for one of the central pads. The plot with the difference $x_C - x_L$ on the x axis instead of $x_R - x_C$ is very similar.

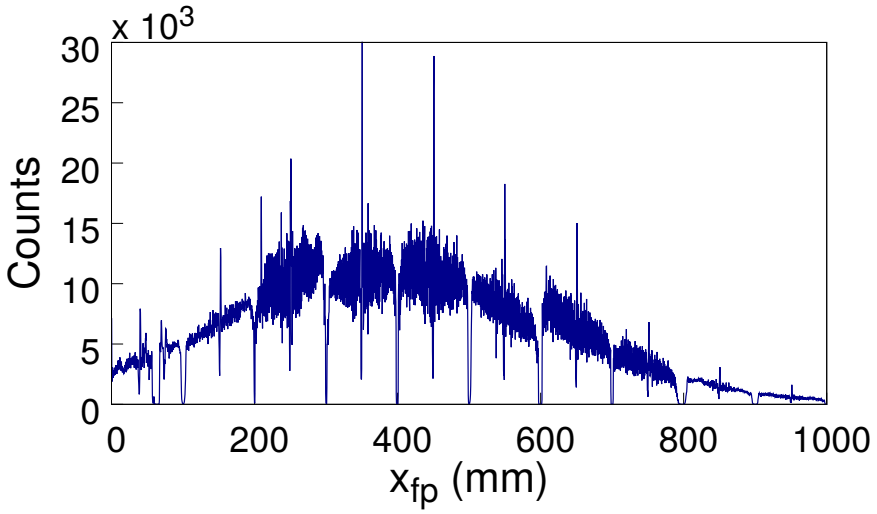

Figure 4.5.: Calibrated spectrum of the position of the detected ions on the MWPPAC detector for the present experiment.

The focal plane position x_{fp} for each section could then be calibrated from ADC channels to millimeters with a first-order polynomial. The final spectrum of the position of the detected

ions on the MWPPAC detector for the present experiment is shown in Figure 4.5. The spaces each 100 mm are due to the separation between the different sections. For each section the two central wires are short-circuited for calibration purposes, therefore the two central channels of each pad should have about twice and half the counts of the other channels, respectively. This is also visible in Figure 4.5.

Timing information from the MWPPAC detector

The timing signal coming from the MWPPAC is used to derive the ToF of the detected ions. This is measured as the time difference between the sections of the MWPPAC (start) and the delayed signal of the MCP (stop). The 10 signals are sent to a TAC, whose output has to be calibrated to obtain the true timing information. The ToFs of the different sections are initially not aligned with respect to each other, therefore an alignment procedure is necessary to use the whole MWPPAC as a single detector for β and A/q determination.

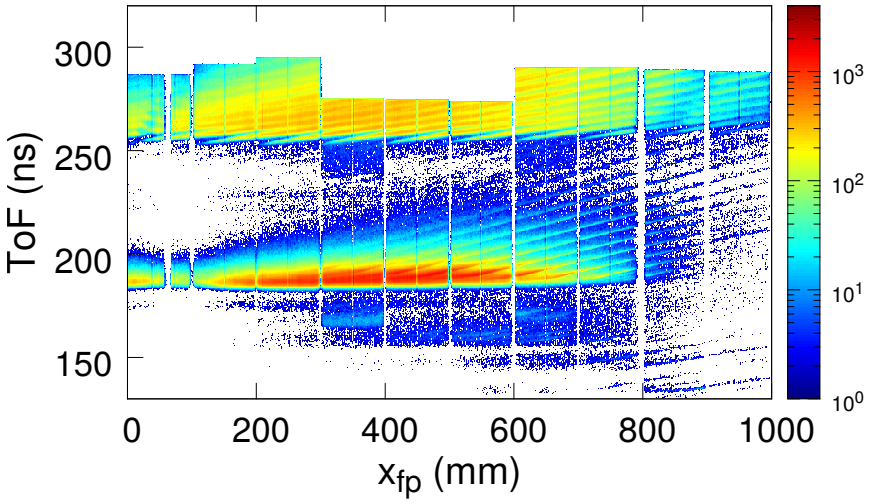

Figure 4.6.: Matrix ToF versus x_{fp} position on the MWPPAC detector after the time alignment between the different sections. Two main structures relative to Te-like ions (around ToF = 190 ns) and Au-like ions (around ToF = 270 ns) are visible.

The resulting matrix of the ToF versus the x_{fp} position of the ions after the alignment procedure is reported in Figure 4.6. Once the sections were aligned one with the respect to the other, a common ToF offset t_0 had to be set in order to determine the velocity distributions of the ions. In many previous experiments PRISMA was coupled with gamma arrays like CLARA [123] and AGATA[124], which allowed to determine t_0 with good precision through the measurement of the Doppler shift for gamma rays emitted in flight by the detected ions (see for example Refs. [118, 122, 125]). In this case no gamma detector was coupled to PRISMA, therefore t_0 had to be calculated as the ratio between the length of the trajectory in PRISMA (L $\simeq$ 5.9 m) and the estimated velocity of the elastically scattered Te-like ions (v $\simeq$ 3.09 cm/ns), so that $t_0 = L/v \simeq 190$ ns. The resulting ToF and β spectra for the

detected ions in the present experiment are reported in Figure 4.7. Light and heavy reaction partners are clearly separated.

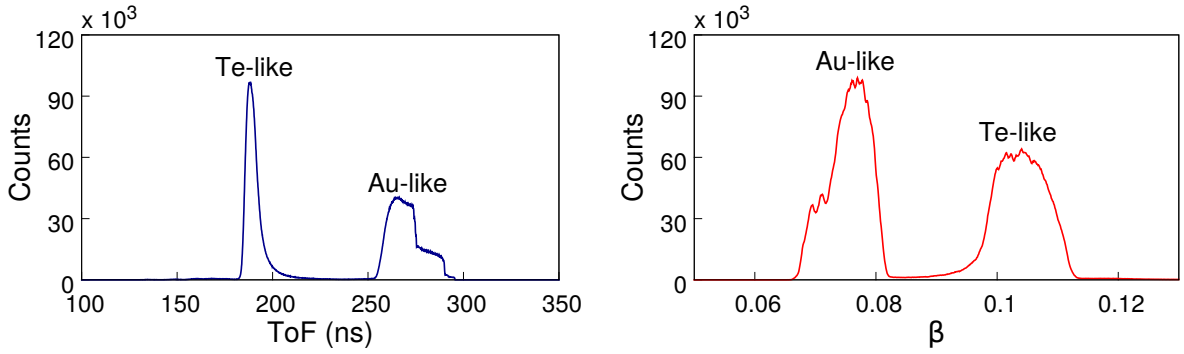

Figure 4.7.: ToF (left) and β (right) distributions. In both figures Te-like (faster) and Au-like (slower) ions can be clearly distinguished.

A finer alignment of the ToF was obtained, in a second step, by looking at the structures in the matrix where the mass-over-charge ratio (A/q) is plotted versus x_{fp} (see Figure 4.8). This ratio is proportional to the ToF, according to the relation:

$$\frac{A}{q} = \frac{B\rho}{L}\, ToF\ . \tag{4.4}$$

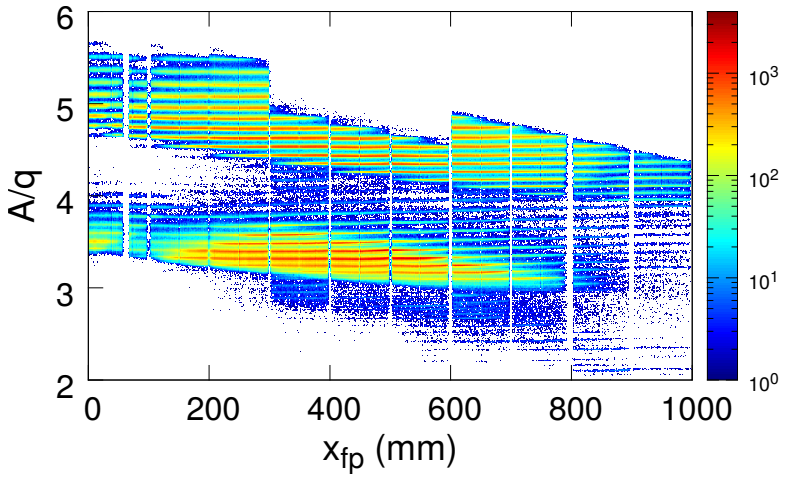

Figure 4.8.: Matrix A/q versus X position on the MWPPAC detector after a finer time alignment between the different sections. Two main structures relative to the light and heavy partners of the reaction are visible.

Equation 4.4 implies that a possible imprecision in the determination of t_0, as previously discussed, is reflected in a proportional imprecision in the absolute A/q values. This may affect the reconstructed atomic charge state distribution in absolute value but has no effect

on the final mass distribution, neither in absolute mass number value nor in the extracted absolute yields.

4.2.3. The ionization chamber

At the end of their trajectory inside the spectrometer the ions are detected and stopped in the ionization chamber, which was described in Section 2.3.4. This last detector is used as a E-ΔE telescope for Z identification (see Section 2.2). The signals of the IC are not calibrated from ADC units to MeV but rather aligned one with respect to the other, matching the gains of the different sections. This *gain matching* procedure is usually carried out before the experiment, sending signals with a pulser inside the 40 pads of the IC and working on the output spectra to obtain the right coefficients for a linear "calibration".

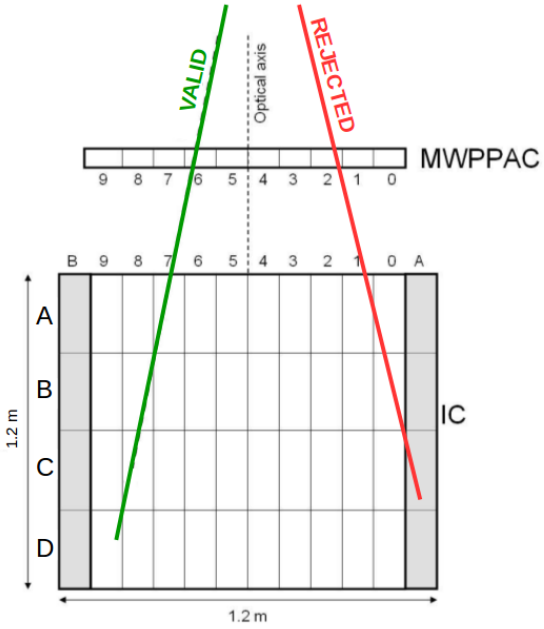

Figure 4.9.: Schematic drawing of the focal plane detectors of PRISMA. The side pads of the IC are in grey. The green line represents a possible valid trajectory of an ion stopped in the IC, while the red line represents the trajectory of an ion that crosses the side pads and is therefore rejected. Adapted from Ref. [122].

In Figure 4.9 a picture of the IC is depicted. On both sides of the IC are two additional rows of pads (shaded areas), called *side pads*, with a veto function: if an ion releases en energy higher than a certain threshold inside one of these pads, the event is rejected (red trajectory). The threshold value can be adjusted independently for each single pad. Ions with trajectories that are too inclined or too far from the central one can release enough energies in the side pads to be vetoed and then discarded from the final analysis. Moreover, events in which the energy loss is not consistent with the reconstructed trajectory are rejected as well. All the other events are considered valid (green trajectory).

The combination of the valid signals coming from the IC can be used to construct the E-ΔE matrix, reported in Figure 4.10.

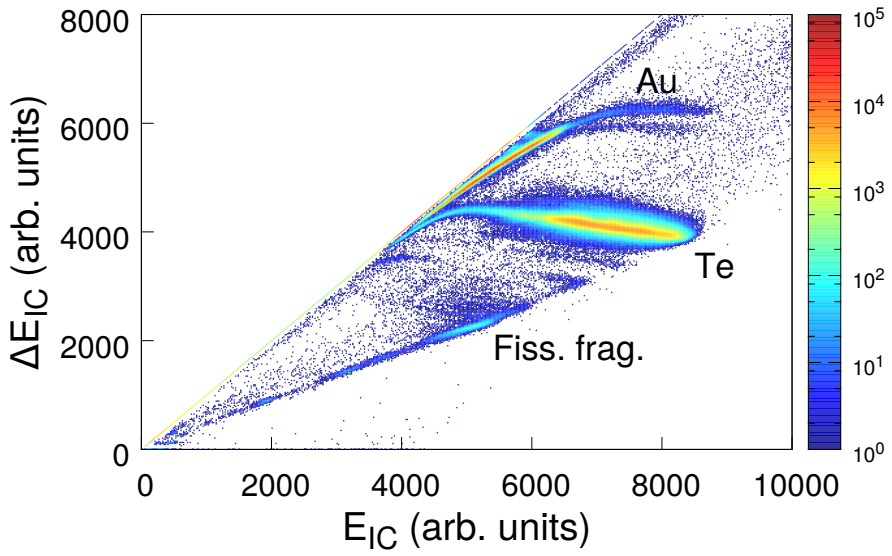

Figure 4.10.: E-ΔE matrix for the present experiment. Te-like and Au-like ions are visible, together with fission fragments around Z ∼ 30-40.

Here the energy ΔE_{IC} lost by the ions in the first two sections of the IC is plotted versus the total energy E_{IC} released in the IC. The different atomic numbers are separated according to Equation 2.2. The most intense band corresponds to Te-like ions. One also observes Au-like ions in the region where ΔE and E merge, since they are almost stopped in the ΔE sections. Around Z ∼ 30-40 are located ions which likely correspond to fission fragments. The punch-through effect due to these non-stopped ions in the IC is visible.

Figure 4.11 shows the calculated (left) and experimental (right) trend of the energy of Te-like and Au-like ions detected in PRISMA as a function of the in-plane scattering angle.

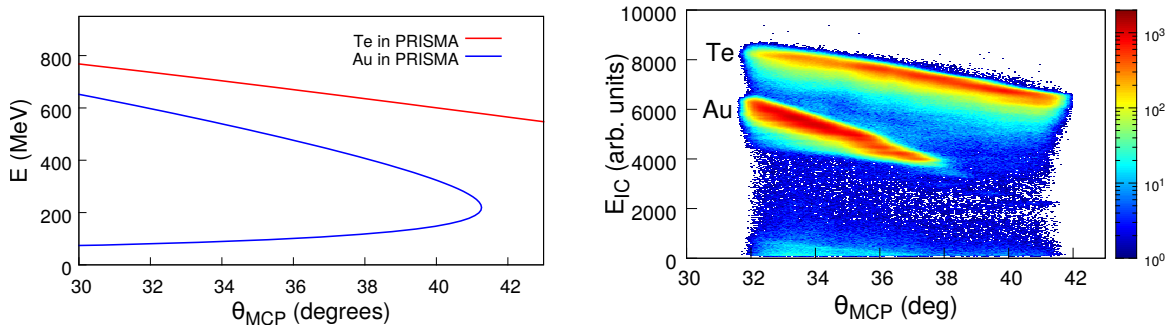

Figure 4.11.: Calculated (left) and experimental (right) trend of the energy of Te-like and Au-like ions detected in PRISMA as a function of the in-plane scattering angle, θ_{MCP}. The magnetic fields of the spectrometer were optimized to detect Te-like ions.

The blue theoretical curve for Au-like ions detected in PRISMA shows the so-called double ("forward" and "backward") solution, typical of inverse kinematics reaction, whereas the same structure is not exactly reproduced in the experimental matrix. We remind that Te-like have a higher magnetic rigidity with respect to Au-like ones, due to their higher velocity, and the magnetic fields of the spectrometer were set to bring the Te ions with maximum yield near the center of the focal plane. Moreover the TACs which measure the ToF between the MCP and the MWPPAC of PRISMA cut the less energetic Au-like ions, as shown in Figure 4.6. For these reasons the Au-like ions in the matrix E_{IC} vs θ_{MCP} are only a fraction of their total yield and the less energetic ones are indeed absent.

4.2.4. The trajectory of the ions in PRISMA

The calibrated quantities extracted from the different detectors are given as input to the Solver routine, included in the PRISMA libraries, to reconstruct the trajectory of the ions and identify them in charge and mass. According to the description given in Ref. [119], trajectories are calculated combining the time and position information from the PRISMA detectors with the equations of motion of a charged particle in a magnetic field.

As a detailed map of the quadrupole and dipole magnetic fields of PRISMA is not available, some approximations are necessary to calculate the trajectory. They are the following:

- magnetic elements are considered to be ideal.
- ions are emitted from the center of the target (the use of a strip target makes this condition an excellent approximation);
- trajectories are supposed to be planar in the xz plane of the PRISMA frame of reference (z is the direction of the incoming ions, as in Figure 4.12);

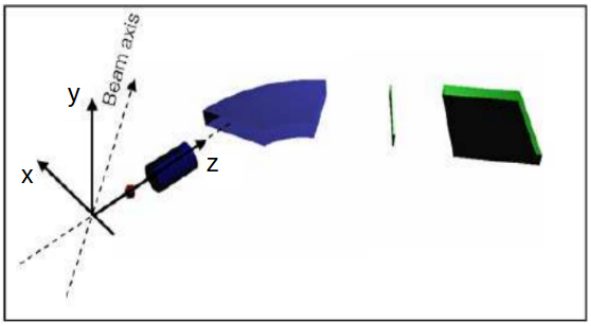

Figure 4.12.: Scheme of the PRISMA spectrometer with a label on the axis as they are used in text. Adapted from Ref. [125].

We will now derive the equations of motion in a dipole and a quadrupole magnetic field. Then we will describe the particular routine used to reconstruct trajectories in PRISMA.

Motion in a quadrupole magnetic field

With reference to Figure 4.12, the quadrupole magnetic field is given by the espression

$$\vec{B} = -\nabla U$$

where

$$U(x,y) = \frac{B_{max}}{\rho} xy$$

and the force acting on a charged particle is given by the Lorentz equation $\vec{F} = q\vec{v} \times \vec{B}$. This force have components only along the xy plane, in particular:

$$F_x \simeq q v_z B_x(x,y)$$
$$F_y \simeq -q v_z B_y(x,y)$$

The final effect of the quadrupole magnetic field is to focus the ions in the vertical (y) direction and defocus them in the horizontal (x) direction with a hyperbolic motion. Central trajectories are not deviated at all.

Motion in a dipole magnetic field

The motion of the ions in a dipole field is even simpler to describe. The Lorentz force acts on the charged particles in a perpendicular direction with respect to the plane formed by their velocity v and the magnetic field B, making the ions travel a circular path of radius ρ. This radius is related to the ratio m/q of the particles according to the relation:

$$\rho = \frac{\mathrm{mv}}{\mathrm{qB}} \tag{4.5}$$

which can be easily derived from the equivalence between the Lorentz force and the centripetal force $m\omega^2\rho$ that keeps the ions on a circular trajectory.

Equation 4.5 is very important because it states one of the fundamental principles for the operation of a magnetic spectrometer. The incoming ions are spread on the focal plane according to their magnetic rigidity, or p/q ratio.

$$\mathrm{B}\rho = \frac{\mathrm{p}}{\mathrm{q}} \tag{4.6}$$

It also sets a limit on the maximum mass and energy that an ion can have to be properly detected, once the maximum magnetic field and bending radius of the spectrometer are fixed in its construction. In the case of PRISMA the maximum magnetic rigidity is 1.2 T·m. In the present experiment PRISMA was almost pushed to the limit of its performance, being the p/q of Te-like ions close to 1.07 T·m.

Trajectory recontruction

Let us now combine measured quantities and equations of motion to reconstruct the total length of the trajectory. We can divide it in five sections, as follows:

- the ion position at the entrance of the quadrupole is perfectly determined under the assumptions that the ion is scattered from the center of the target (see approximations above) and measuring its position on the MCP. The distance target-quadrupole entrance is therefore a straight line of length L_1;

- in the quadrupole the ion travels a hyperbolic path of length L_2;

- from the calculated exit point at the end of the quadrupole the path to the dipole is described by a straight line of length L_3.

- in the dipole the ion travels a circular path of length L_4 in the horizontal dispersion plane.

- from the dipole to the MWPPAC the trajectory is straight with a length L_5.

The total length of the trajectory L_{tot} will be then given by:

$$L_{tot} = \sum_{i=1}^{5} L_i$$

and its value is around 5.8 m.

The Solver routine is an iterative software procedure which is used to reconstruct the trajectory. It starts from the known position of the ion in the MCP and a guess value for $\rho = 120$ cm, corresponding to the central trajectory; following the path described here above, it returns a position of the ion on the focal plane and compares it with the measured one. If the difference between this two positions is less than 1 mm the iteration ends, otherwise it repeats the procedure slightly changing the value of ρ until it reaches a good agreement with the measured value.

As pointed out in Ref. [119], this procedure turns out to be very reliable for central trajectories but starts to fail as the ions cover all the dispersion plane. The difference between true and approximated trajectories turns out to be around 2.4% which is reflected in the maximum mass resolution that one can obtain.

Once the trajectory reconstruction has been performed, the range R of the ion in the IC can be calculated in the following way:

- first the events in the IC that are not compatible with the calculated trajectory are rejected;

- the total energy lost by the ion is calculated by summing the measured contributions ΔE_i in different pads;

- using the ΔE_i as a weight, a weighted distance L_w between the MWPPAC and each IC section is constructed;

- the range R can then be calculated as the difference between L_w and the distance MWPPAC-IC.

4.3. Proton-transfer channels

The routine just described has the final goal to completely identify the incoming ions on an event-by-event basis. The only information from the MWPPAC detector (ToF and x_{fp}) is not sufficient to completely identify the detected ions: one needs first to measure the atomic number Z. With light and medium-mass ions (A < 90-100) at energies around 5 MeV/A this goal can be quite easily accomplished because the Z resolution of the IC allows to separate very clearly the different nuclear charges (see for example Figure 2.4(a)). With heavier ions the IC performance is pushed to its limit and the Z identification becomes more difficult. In γ-spectroscopy experiments usually the bombarding energy is well above the Coulomb barrier, increasing the cross sections of proton transfer channels, and the required coincidence with the γ detector allows to reject the elastic component. Example of E-ΔE matrices where ions with A > 100 were detected in these conditions are reported, for example, in Ref. [126–128].

In the present experiment the bombarding energy was instead close to the Coulomb barrier and no γ detector was in coincidence with PRISMA. As a consequence, in Figure 4.10 one can see the difficulty to clearly separate the different proton transfer channels, which seem to be overwhelmed by the strong component of Te ions including elastic+inelastic+neutron transfer channels.

Looking at the projection of this matrix on the y axis after a proper rotation, reported in Figure 4.13 (left), one can notice that no peak relative to different nuclear charges shows up, since they are completely embedded in the tail of Te ions. It is not straightforward to understand whether this behaviour has to be attributed to a faulty operation of the IC, to an imperfect gain matching between the different IC pads, to the low cross sections for proton transfer channels at this bombarding energy or instead to a combination of more of these factors. To discard the first factor (a faulty operation of the IC) we plotted in Figure 4.13 (right) the projection on the y axis of the E-ΔE matrix in the region of the fission fragments. The presence of well-separated peaks relative to different atomic numbers suggests that the IC was working properly during the experiment. Since the expected Z resolution of the PRISMA IC is $\Delta Z/Z \sim 1/60$, if it is working properly we should be able to partially distinguish the proton transfer channels also in the Te-like region.

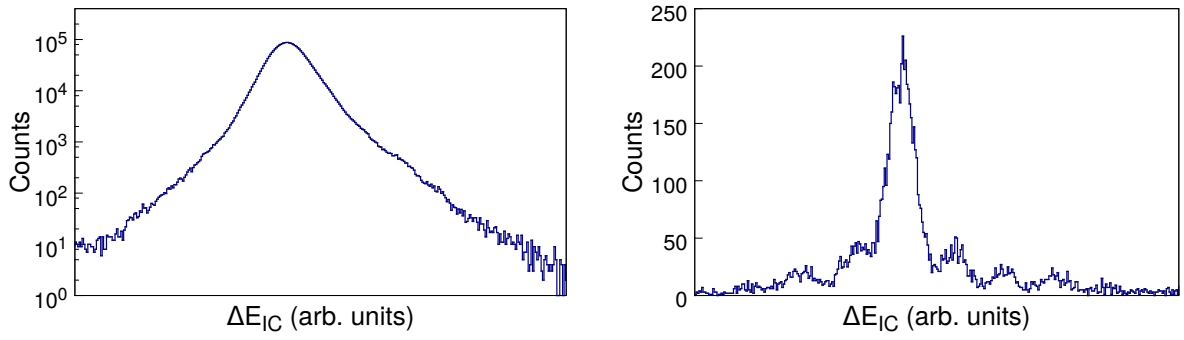

Figure 4.13.: Projection on the y axis of the rotated E-ΔE matrix in the region of Te-like ions (left) and fission fragments (right). The IC resolution seems to be enough to distinguish different atomic numbers of fission fragments around Z = 30-40.

In order to infer the possible presence of an imperfect gain matching between the IC pads we:

- selected, for each of the 10 sections of the MWPPAC and the IC, only the ions which travel straight trajectories without releasing energy in the nearby pads;
- plotted a E-ΔE matrix for each section with the selected events;
- rotated each matrix of a proper angle (the same for all) and projected on the y axis the region of Te-like ions;
- aligned the centroids of the projections with respect to each other introducing a small correction;
- created a new E-ΔE matrix summing all the corrected (and rotated) E-ΔE matrices with the selected events.

Figure 4.14 shows the projection on the y axis of the resulting E-ΔE matrix after the procedure described above. Several peaks are now visible in the tail of the (0p) channel, with an almost constant step in ADC channels. They represent the different mass-integrated proton transfer channels, ranging from (-3p) to (+4p). The red curves represent the multigaussian fit used to extract the absolute yields of these channels. The fit also returns for the Z resolution of the IC a value $\Delta Z/Z \sim 1/65$.

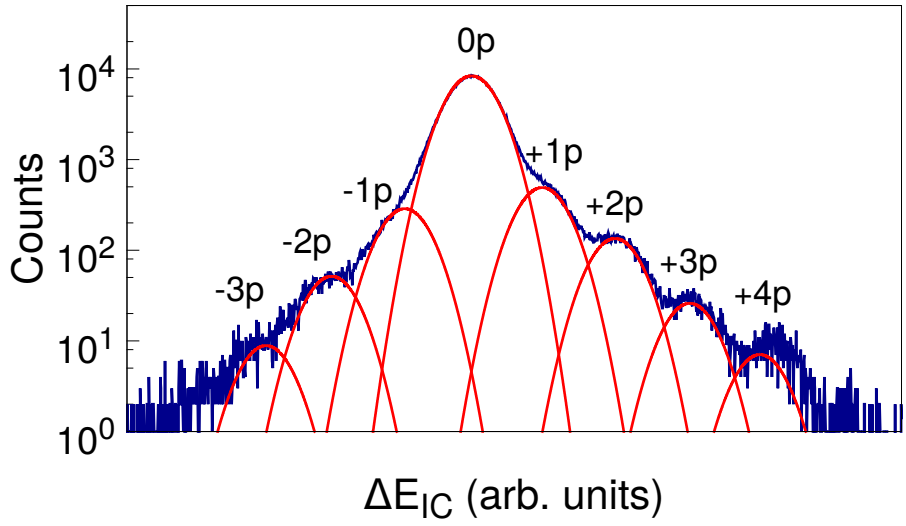

Figure 4.14.: Projection on the y axis of the rotated E-ΔE matrix obtained following the procedure outlined in the text. Peaks corresponding to mass-integrated proton transfer channels, from (-3p) to (+4p) are now visible. The red curves represent the multigaussian fit used to extract the absolute yields for these channels.

From the distribution of Figure 4.14 one can notice that both proton stripping and pick-up channels are present but the latter seems to be the favourite path. We will come back on this point in Chapter 6, comparing the present system with other similar ones previously studied.

More detailed information could be obtained from the study of mass and Q-value distributions of the proton transfer channels but their low cross sections and strong convolution with the tail of the (0p) channel prevented us from extracting full isotopic distributions for the identified Z. We were anyway able to compare the mass-integrated yields with the theoretical predictions of GRAZING, as it will be shown in Chapter 6.

4.4. Neutron transfer channels of Te

Besides proton transfer, the study of neutron transfer channels is of great interest to learn about the possible population of the neutron stripping path which in turn would lead to the population of neutron-rich nuclei in the heavy partner region. We set a thin gate on Te (Z = 52) in the E-ΔE matrix and plotted in Figure 4.15, for the selected events, a bidimensional spectrum with the total energy E_{IC} versus the product $\rho\beta$. The radius ρ is determined through the trajectory reconstruction procedure outlined in Section 4.2.4. According to Equation 4.1, the different charge states show up in this matrix as straight bands.

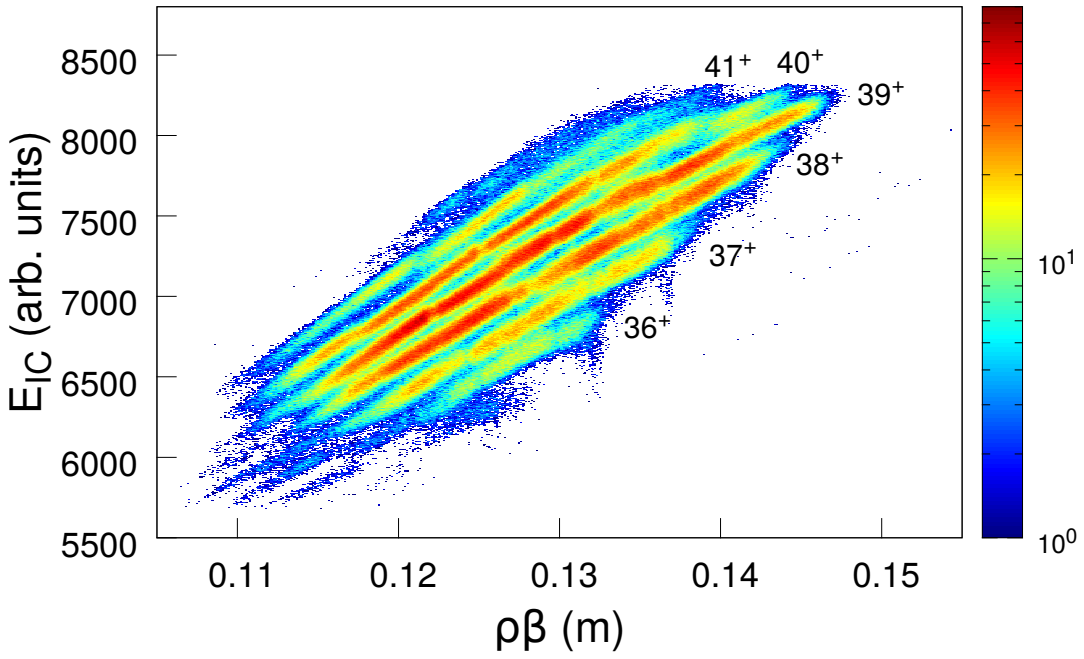

Figure 4.15.: Matrix E_{IC} vs $\rho\beta$ for Te ions in the present experiment. Up to six atomic charge states (labeled) can be identified.

We could reconstruct the Te mass spectrum summing over all the identified atomic charge states q_j (here j = 1, 2, ..., 6). Gating on each q_j, we plotted six A/q spectra and labelled the different isotopes starting from the A = 130 peak. From the position of their centroids, an average value of the charge state q_j (which was not known a priori) was determined in the following way:

$$q_j^{\text{aver}} = \frac{1}{N}\sum_{i=1}^{N}\frac{A_i}{(A/q_j)_i}$$

where N is the number of peaks (masses) in the spectrum and $(A/q)_i$ is the centroid of the i-th peak. These values may not be integer numbers and can be regarded as *effective charge* values. The mass distribution was eventually obtained summing over all the charge states:

$$A = q_j^{\text{aver}}\left(\frac{A}{q_j}\right)_i \qquad \text{for i} = 1, ..., \text{N and j} = 1, ..., 6.$$

In Figure 4.16 the mass spectrum is displayed. The mass resolution is quite poor ($\Delta A/A \sim 1/180$) and the peaks relative to the different neutron transfer channels are not well defined, in such a way that it is very difficult to extract reliable absolute yields. The mass resolution could be improved taking into account the presence of optical aberrations and applying empirical corrections to reduce their effect. This will be discussed in more detail in the following Section.

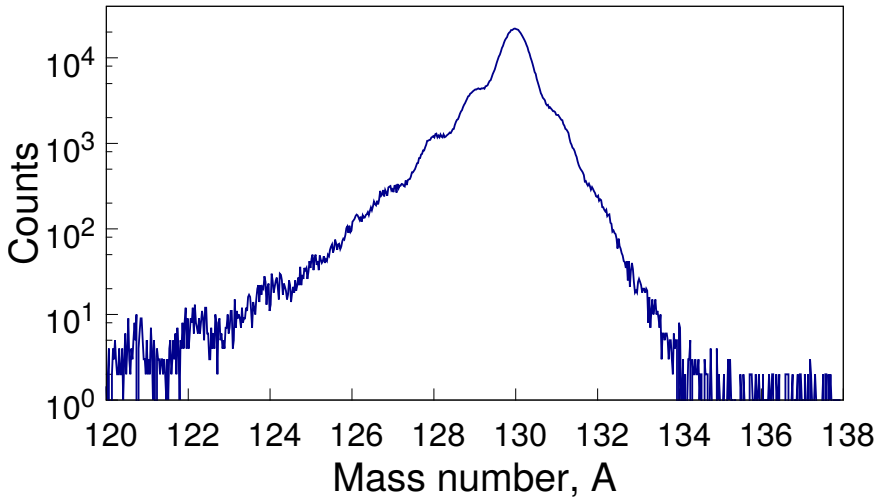

Figure 4.16.: Mass spectrum for Te ions (Z = 52) obtained in the present experiment without any empirical corrections to reduce the effect of optical aberrations.

4.4.1. The improvement of the mass resolution through empirical corrections

In the analysis of neutron transfer channels one has to be aware that mass discrimination of the outgoing reaction products detected in PRISMA becomes more and more critical with very heavy ions. In particular, the mass resolution is affected by the presence of optical aberrations, especially for non-central trajectories, which have to be properly taken into account in the trajectory reconstruction. Aberrations are mainly due to the presence of higher-order magnetic fields and fringe fields which deviate the ions trajectory from the expected behaviour (consisting, in a first-order approximation, of straight lines and a perfect circumference in the dipole). A proper analysis had to be followed in the present work to separate the different isotopes at a level sufficient to be able to derive absolute yields. The

result is an improvement of the final mass resolution and a clearer discrimination of neutron transfer channels.

Effective quadrupole length and distance from target

As a first step we slightly modified the nominal values of the quadrupole length L_Q and the distance target-quadrupole d_{QT} to take into account the presence of fringe fields and higher-order magnetic fields. The optimization was performed by changing iteratively the two values in an interval close around the nominal ones (L_Q = 420 mm; d_{QT} = 500 mm), looking for the values that maximize the A/q resolution. The new values (L_Q = 410 mm and d_{QT} = 540 mm) were then kept fixed for the following analysis.

Alignment of A/q structures with a polynomial

The effect of aberrations could not be completely eliminated with the simple procedure just described. In Figure 4.17 (left) one can notice that the trend of A/q as a function of the entrance x and y position on the MCP and the exit position on the MWPPAC detector is still parabolic. This effect could be reduced fitting and linearizing these structures with a polynomial. Starting from the matrix A/q versus x position on the MCP, for each bin the positions of the A/q centroids were determined in an iterative way and fitted with a n-th order polynomial, with n depending on the specific case (see the blue curves in Figure 4.17 left). The same procedure was then repeated for the matrices A/q versus y position on the MCP and x_{fp} position on the MWPPAC, in this order.

The result of the correction is shown in Figure 4.17 right. The parabolic trend is much reduced and, as a consequence, the A/q resolution increased.

Alignment of A/q structures with a fine correction

One can notice in the bottom panel of Figure 4.17 that the polynomial cannot reproduce the "wavy" structure of the A/q bands, which is probably due to board effects and small disomogenities of the electric field in the different sections of the MWPPAC detector. When computing the final mass value, this structure was of course present also in the matrix mass versus x_{fp}, reported in Figure 4.18 (left), affecting the maximum mass resolution that could be obtained. The need to have the highest possible mass separation with these heavy ions prompted us to apply a further fine correction to reduce this effect:

- after gating on each charge state, six matrices (one for each charge state) A/q vs x_{fp} were plotted;
- each matrix was projected onto the y axis and the position $(A/q)_{tot}$ of the centroid relative to the A = 130 peak was registered;
- x_{fp} was divided in small bins of 5 mm and for each bin the position $(A/q)_{bin}$ of the centroid relative to the A = 130 peak was registered;
- for each bin the quantity δ was defined as the difference $(A/q)_{bin}$-$(A/q)_{tot}$;
- the new A/q value $(A/q)_{new}$ was given by $(A/q)_{new} = (A/q)_{bin} - \delta$.

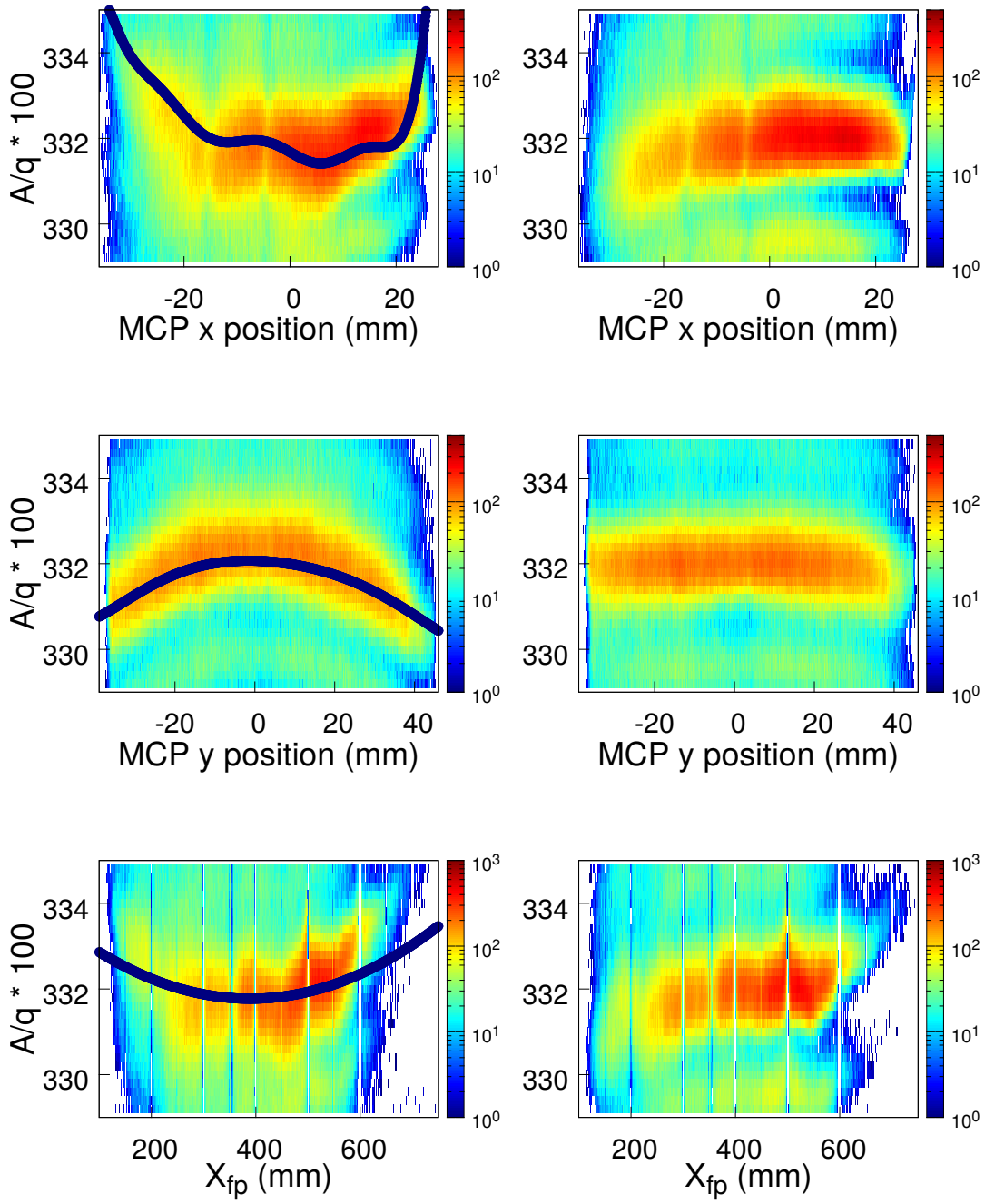

Figure 4.17.: Alignment of the A/q structures with a polynomial: the unaligned matrices (left) of A/q as a function of MCP x (top), MCP y (middle) and MWPPAC x_{fp} (bottom) positions with the fitting curves superimposed and the aligned matrices (right). See text for details.

This procedure was implemented in the *MassCalculator* routine of the PRISMA libraries. The corrections δ_j for each charge state q_j are given as input to the program and the value of $(A/q)_{new}$ for each bin is returned as output.

The final result is shown in Figure 4.18 (right). The fine alignment of A/q for the different charge states is reflected in the mass distribution, with a mass resolution of $\Delta A/A \sim 1/240$, which means an increase of $\sim 35\%$ with respect to the value previously reported in connection with Figure 4.16.

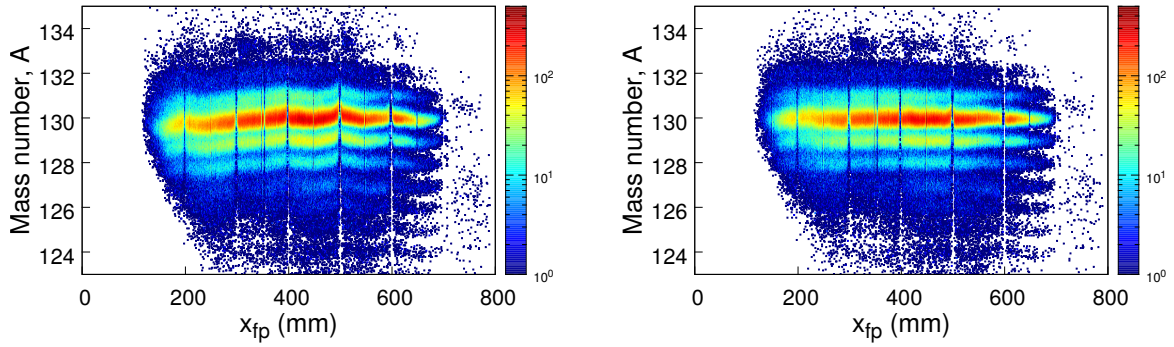

Figure 4.18.: Matrices of Te mass vs x_{fp} position before (left) and after (right) the manual alignment procedure described in the text.

Figure 4.19 shows the unidimensional Te mass spectrum in linear and logarithmic (in the insert) scale, together with the multigaussian fit used to extract the absolute yields for neutron transfer channels.

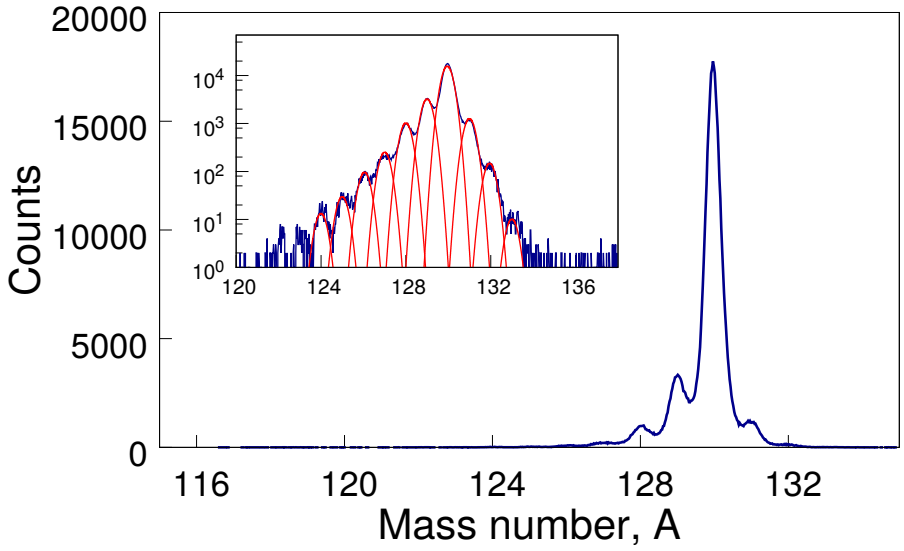

Figure 4.19.: Mass spectrum for Te ions in linear scale. In the insert the same spectrum in logarithmic scale is plotted together with the multigaussian fit used to extract the absolute yields for each transfer channel.

Most of the transfer flux is on the stripping side, visible up to the (-6n) channel, while on the pick-up side the transfer is visible up to the (+3n) channel. This behaviour can be ascribed to the combination of optimum Q-value considerations, which for these neutron-rich system predict also the population of the neutron stripping path, and the effect of neutron evaporation, which tends to shift the yields towards lower mass values. Only the analysis of the Q-value distributions and the comparison with theoretical models can shed light on which of the two processes is dominating. The understanding of the reaction mechanisms involved is necessary to obtain information concerning the possible population of neutron-rich nuclei in the two regions of interest, close to N = 82 and N = 126. We will discuss this topic in more detail in Chapter 6.

Concerning the heavy partner, we also investigated the possibility to determine the full isotopic distribution for these very heavy ions with A $\sim$ 200. In the matrix A/q vs x_{fp} of Figure 4.8 the A/q resolution looks very promising but, on the contrary, the charge state resolution turned out to be insufficient to distinguish reliably the different charge states of Au ions and no mass spectrum could be extracted.

4.4.2. Q-value reconstruction

As anticipated at the end of the previous Section, the study of the Q-value distributions is essential to gain a deeper insight on the reaction mechanisms involved in the transfer process. Narrow Q-value distributions peaked close to the ground-to-ground-state Q value would be an indication that the transfer process has a quasi-elastic character and few energy is dissipated in the reaction; on the other hand, broad Q-value distributions would indicate a shift of the reaction regime towards a deep-inelastic character, usually featuring a large number of transferred nucleons and large kinetic energy losses.

The reaction Q value can be determined using only the information coming from PRISMA under the assumption of pure binary reaction 1 + 2 $\rightarrow$ 3 + 4 (see Figure 4.20).

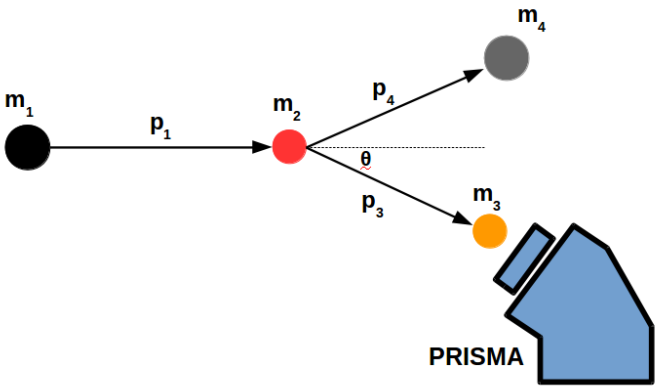

Figure 4.20.: Schematic drawing of a binary reaction 1 + 2 $\rightarrow$ 3 + 4. Particle 3, representing in our case a Te-like ion, is detected in PRISMA.

We remind that the reaction Q value is defined as the difference between the initial and final masses of the reacting nuclei or, equally, by the difference between the final and the initial kinetic energy T of the recoils.

$$Q = \Delta T = E_3 + E_4 - E_1 \tag{4.7}$$

Figure 4.21 shows, as an example, the ground-to-ground-state Q values, Q_{gs}, as a function of the number of transferred neutrons, ΔN, for the indicated proton transfer channels from (-2p) to (+2p). The arrows are placed in correspondence of the optimum Q value, calculated as:

$$Q_{opt} \approx E_{\rm cm}\left(\frac{Z_b Z_B}{Z_a Z_A} - 1\right) \tag{4.8}$$

for a reaction a+A $\rightarrow$ b+B. According to Equation 4.8, only when protons are transferred Q_{opt} can be $\neq 0$. This is of course an approximation of Equation 1.8, obtained by matching the distances of closest approach before and after the reaction.

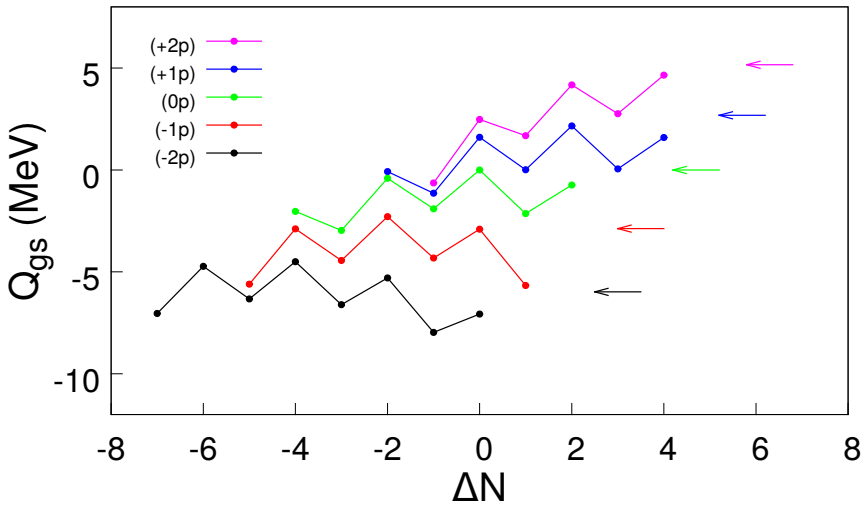

Figure 4.21.: Ground-to-ground-state Q values, Q_{gs}, for the present reaction as a function of the number of transferred neutrons, ΔN, for the indicated proton transfer channels from (-2p) to (+2p). The arrows are placed in correspondence of the optimum Q value, as calculated in Eq. 4.8.

We can combine Eq. 4.7 with the condition of momentum conservation in the collision,

$$\vec{p_1} = \vec{p_3} + \vec{p_4}\ , \tag{4.9}$$

to obtain an expression for Q which depends only on quantities directly measured. One can rearrange and square Eq. 4.9 in the following way:

$$\vec{p_4}^{\,2} = (\vec{p_1} - \vec{p_3})^2 = p_1^2 - 2p_1 p_3 \cos\theta + p_3^2 \tag{4.10}$$

and, reminding that $p^2 = 2mE$, we obtain:

$$E_4 = \frac{m_1 E_1}{m_4} + \frac{m_3 E_3}{m_4} - 2\varepsilon \cos\theta \tag{4.11}$$

where $\varepsilon = \sqrt{E_1 E_3 m_1 m_3}/m_4$. Combining (4.11) and (4.7) we obtain the desired expression for the reaction Q value (cfr. Ref. [129]):

$$Q = \frac{m_3 + m_4}{2m_3 m_4}\ p_3^2 - \frac{m_4 - m_1}{m_4}\ E_1 - \frac{\sqrt{2m_1 E_1}}{m_4}\ p_3 \cos\theta \tag{4.12}$$

It is important to remind that the beam energy E_1 must be corrected for the energy lost in the target, which is estimated using the Northcliffe-Schilling approximation [130] and under the assumption that the reaction takes place in the center of the target: $E_1 = E_{\rm beam} - \Delta E_{\rm loss}$. For the present experiment we used a thin target (200 μg/cm^2) and the effect is therefore very small ($E_{\rm target} \sim 6$ MeV). In typical γ-spectroscopy experiments, where targets can be even 10 times thicker, $\Delta E_{\rm loss}$ can be not negligible at all and this correction would be necessary (see [118] for a more detailed discussion).

Beam particles have $\beta \sim 10\%$, with a Lorentz factor $\gamma = (1-\beta^2)^{-1/2} \sim 1.005$. This means that the correction introduced by using a relativistic approach would be extremely small and for this reason we decided to employ the classic formalism in the derivation of the kinematic equations in this and in the next Chapter.

Figure 4.22 shows the Total Kinetic Energy Loss (TKEL) distributions for neutron transfer channels, obtained with Equation 4.12. We remind that the relation between TKEL and Q value is simply TKEL = -Q. The red lines are placed in corrispondence of the TKEL for the ground-to-ground-state transitions. For few neutron transfers the distributions are peaked at $Q_{\rm gs}$ and confined within 30 MeV. As more neutrons are transferred, the maximum of the distributions is moving away from $Q_{\rm gs}$ and the tail towards larger energy losses is increasing up to 80 MeV. This is an indication that the reaction mechanism is gradually shifting from a quasi-elastic to a more deep-inelastic regime as more neutrons are transferred.

So far no additional information coming from the second arm has been used in the derivation of the TKEL distributions. Employing the second arm, the mass of the binary heavy partner is not simply deduced ma directly measured, although with lower resolution. Therefore we expect that the comparison between the TKEL distributions obtained without and with the kinematic coincidence can give additional information on the character of the reaction. In Chapter 5 we will describe for the first time the analysis procedure for data acquired with the second arm in coincidence with PRISMA and present some interesting results concerning the mass distribution of the heavy partner and the TKEL distributions obtained when both reaction partners are detected.

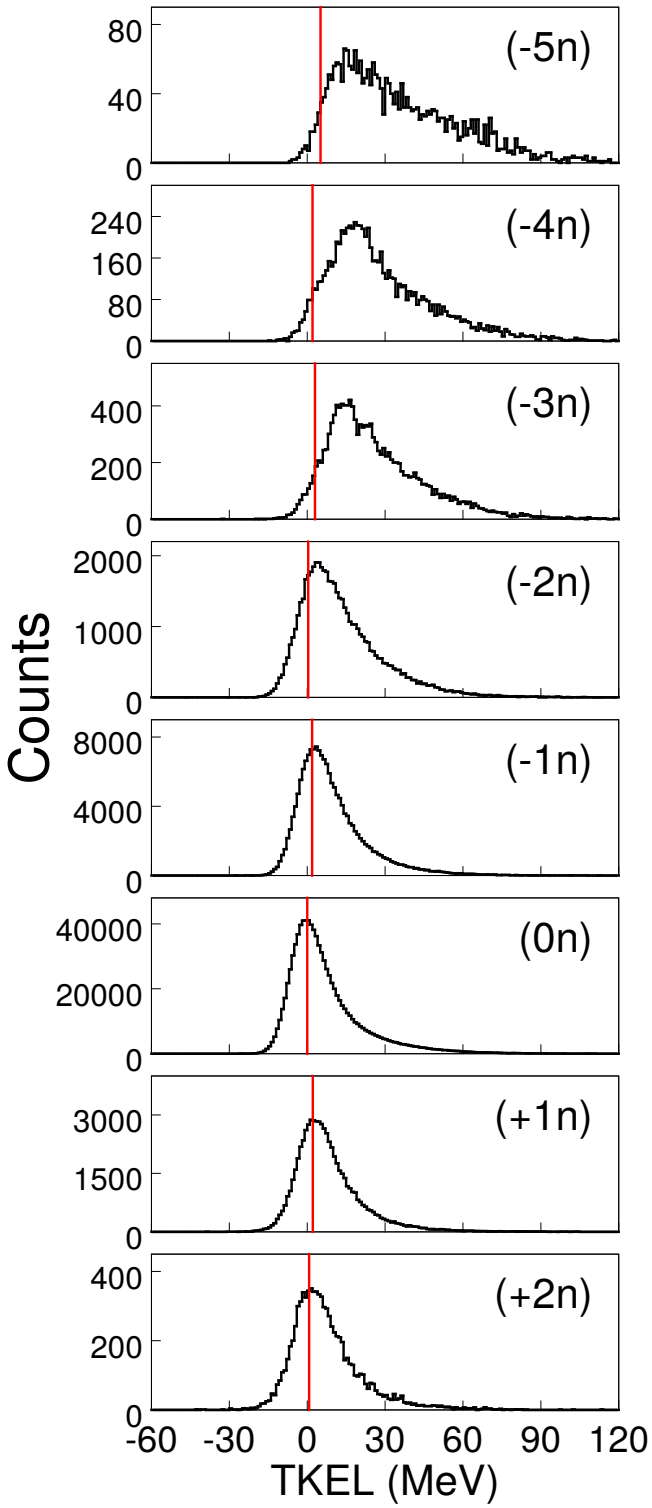

Figure 4.22.: TKEL distributions for the neutron transfer channels from (-5n) to (+2n). The red lines are placed in corrispondence of the TKEL for the ground-to-ground-state transitions, according to Figure 4.21.

5 Analysis of the kinematic coincidence

The kinematic coincidence technique is a powerful tool in heavy ion reactions, in particular for the study of reaction dynamics in elastic, MNT and DIC processes. The method is mainly based on the simultaneous detection of the reaction binary fragments using two different set-ups placed at the kinematically correlated angles. In the present experiment one of the two set-ups is a high-resolution magnetic spectrometer which has allowed to identify one of the reaction partners (the light one) in A and Z. On the coincident second arm the resolutions are lower and we could not achieve a complete A and Z identification of the binary heavy partner. In spite of this, we wanted to obtain information on the behaviour of the heavy partner by measuring its yields and studying the Q-value distributions, obtained by requiring the coincidence condition, as a function of the number of transferred neutrons. This in turn could shed light on the influence of secondary processes on the yields of primary fragments.

In this Chapter we will start by demonstrating the correct operation of the coincidence and present for the first time the calibration procedure to extract physical information from the second arm. Then we will describe the analysis of the data acquired with the second arm to extract relevant results, which will be eventually discussed in Chapter 6.

5.1. Analysis of the second arm data

The second arm of PRISMA has been introduced in Section 2.4, while in Chapter 3 we presented the laboratory and in-beam tests carried out to test its performance and possible future developments. In the present experiment the second arm was used in slave mode, with PRISMA always acting as master trigger. The electronics used to process the signals was composed of a standard analog chain. From the second arm five signals are extracted: two for position determination, one for total energy integration, one for Bragg peak (BP) amplitude measurement and one timing signal for ToF measurement. The corresponding five raw spectra are displayed in Figure 5.1. The x and y position signals come from the delay lines of the PPAC placed before the Bragg chamber (BC); the energy and BP amplitude signals come from the anode of the; the ToF signal (ΔToF) is measured between the MCP of PRISMA (start) and the PPAC of the second arm (stop).

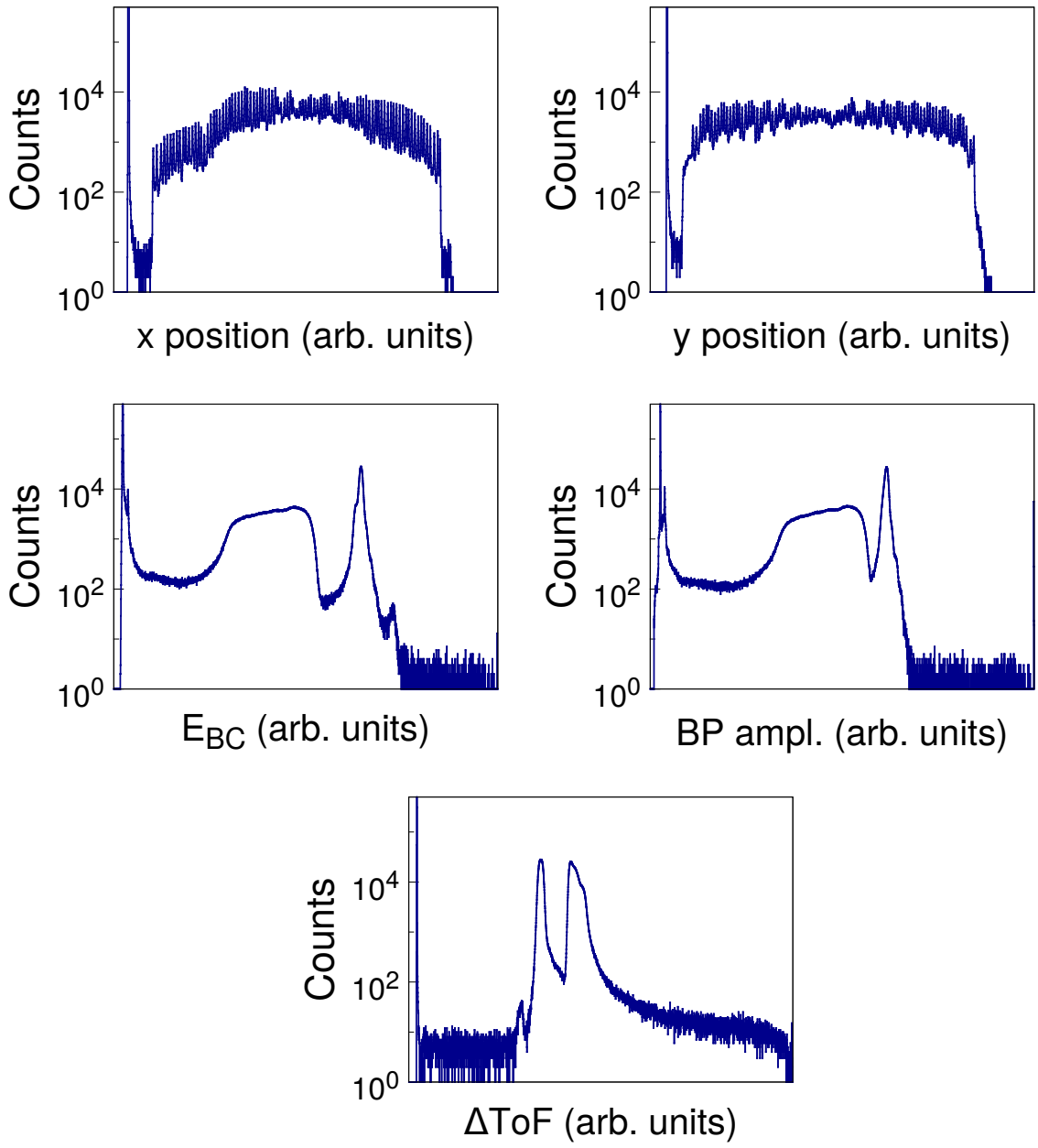

Figure 5.1.: Raw spectra from the second arm. In the top row are the x (left) and y (right) position spectra from the PPAC, in the middle row the energy (left) and the BP amplitude (right) spectra, in the bottom row the ΔToF signal between the MCP of PRISMA and the PPAC of the second arm.

5.1.1. Position information from the PPAC detector

The entrance x and y position of the ions on the PPAC detector are measured through two delay lines and can be calibrated from channels to millimeters with a linear fit. We remind that the PPAC has a diameter of 10 cm and the spacing between the wires is 1 mm. The calibration plot and the resulting calibrated spectra are reported in Figure 5.2, where the parameters of the fitting first-order polynomial y[mm] = A·x[ch]+B are:

	A (mm/ch)	B (mm)
x	-0.05268 ± 0.086 %	62.77 ± 0.096 %
y	-0.05261 ± 0.080 %	60.99 ± 0.093 %

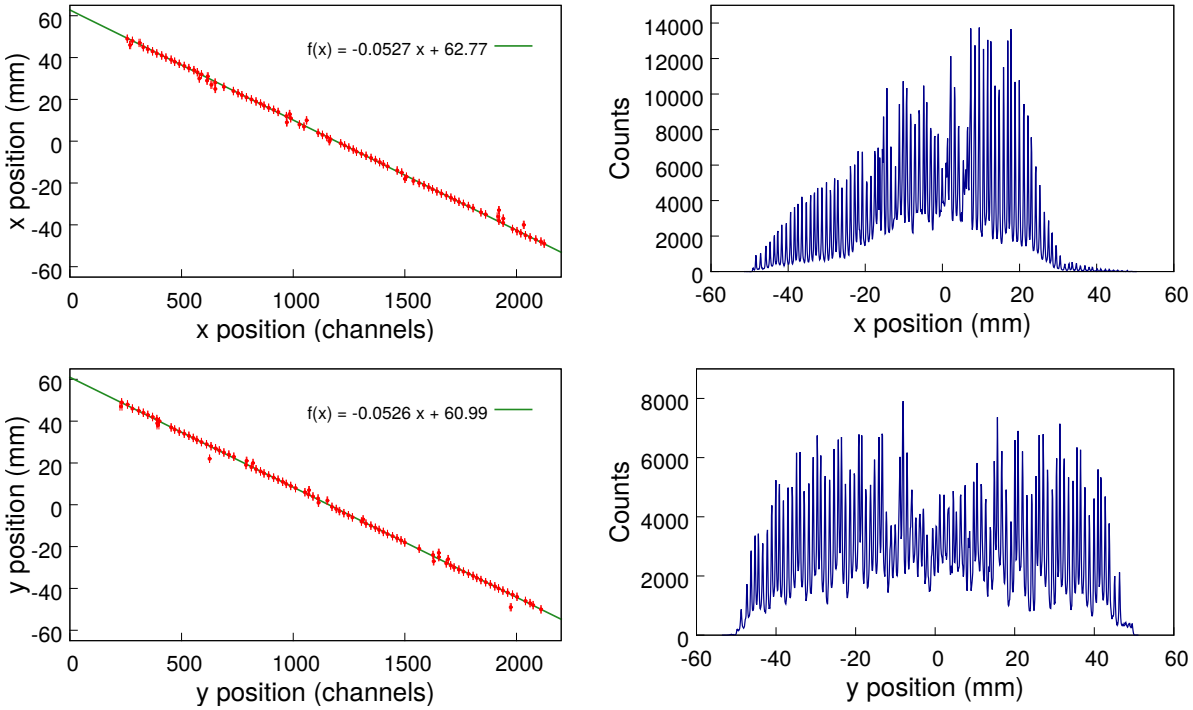

Figure 5.2.: Calibration of the x (top) and y (bottom) position information of the PPAC of the second arm. The calibration plots with the indicated fitting polynomials are on the left panels, the resulting calibrated spectra on the right ones.

The conversion from Cartesian to spherical coordinates was performed coherently with the transformations used for the MCP of PRISMA (see Section 4.2.1). We remind that the second arm is placed at angle of -36.5° with respect to the beam direction at a distance of about 90 cm from the target. Bidimensional position spectra in Cartesian (left) and spherical (right) coordinates are shown in Figure 5.3. The θ angle has been converted to positive for the sake of simplicity.

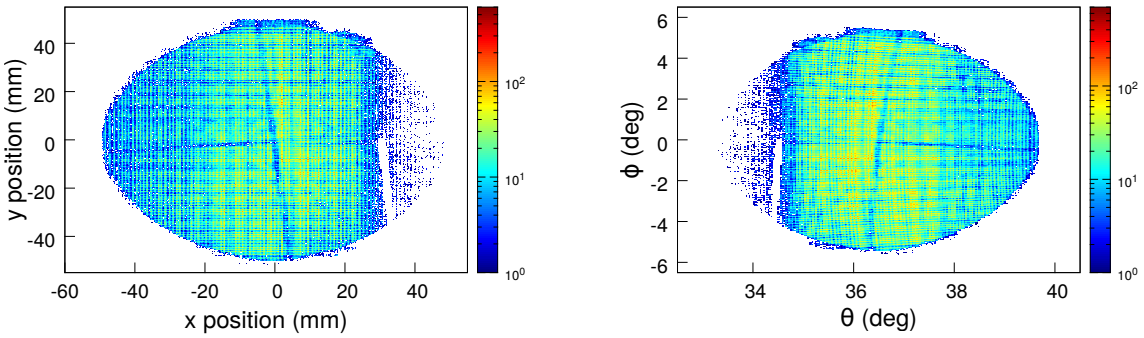

Figure 5.3.: Bidimensional position spectra in Cartesian (left) and spherical (right) coordinates for the second arm PPAC in the present experiment. The cross-shaped mask placed in front of the PPAC for calibration purposes is visible.

Since the PPAC is at the opposite side of the MCP with respect to the beam direction, its lower Cartesian coordinates correspond to higher θ values, and viceversa. This explains why the plots in Cartesian and spherical coordinates are overturned one with respect to the other.

5.1.2. Time information from the PPAC detector

The ΔToF measured between the MCP of PRISMA and the PPAC of the second arm is an essential information to reconstruct the binary partner mass, as will be shown in Section 5.3. It was calibrated from channels to nanoseconds using a time calibrator with a time interval of 10 ns. The delay of the stop signal sent to the TAC from the PPAC was kept fixed at 48 ns, as during the experiment. The calibration plot and the resulting ΔToF spectrum is shown in Figure 5.4.

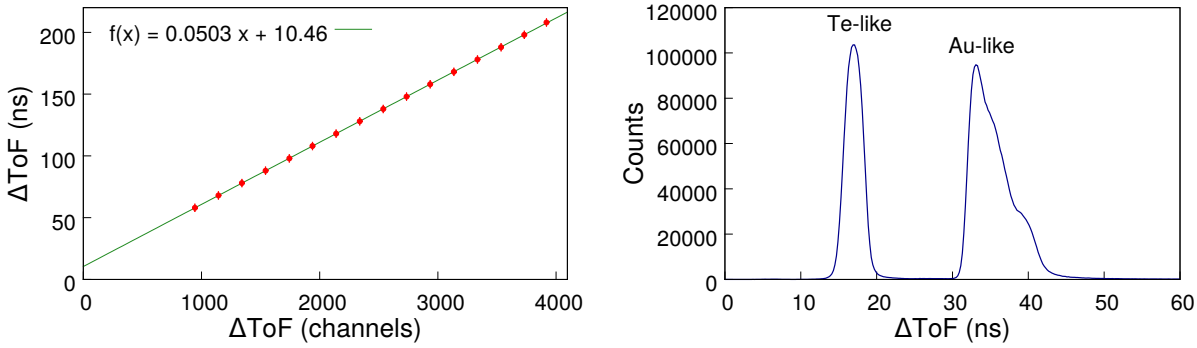

Figure 5.4.: Calibration plot of the ΔToF between the MCP of PRISMA and the PPAC of the second arm with indicated the equation of the linear fit (left) and the resulting calibrated spectrum (right).

The parameters of the fitting first-order polynomial y[ns] = A·x[ch]+B are:

$$A = 0.05028 \text{ ns/ch} \pm 0.086 \%$$
$$B = 10.46 \text{ ns} \pm 1.08 \%$$

Te-like and Au-like ions are very well separated in the spectrum and appear at the expected position according to their respective calculated velocities and the measured distances between target and MCP of PRISMA and between target and PPAC of the second arm.

5.1.3. Z identification in the Bragg chamber

We discussed in Section 2.2 the operating principles of a Bragg chamber and discussed in Chapter 3 the performance of the BC of the second arm with medium-mass ions (Z $\sim$ 28). In that case the Z resolution was Z/ΔZ $\sim$ 50-60 and the different nuclear charges were clearly separated. With heavy ions, like those detected in the present experiment (Z $>$ 50), the identification of proton transfer channels becomes much more challenging. Figure 5.5 (left) shows the matrix BP amplitude versus energy for the present work. The gas pressure in the BC was optimized for the detection of Au-like ions, which show a smooth event distribution, at variance with the Te-like ones, which are not stopped inside the chamber. Light and heavy reaction products are clearly distinguished but no separation between nearby nuclear charges can be achieved. A similar separation is observed also in Figure 5.5 (right) where the timing and energy information from the PPAC and the BC are combined.

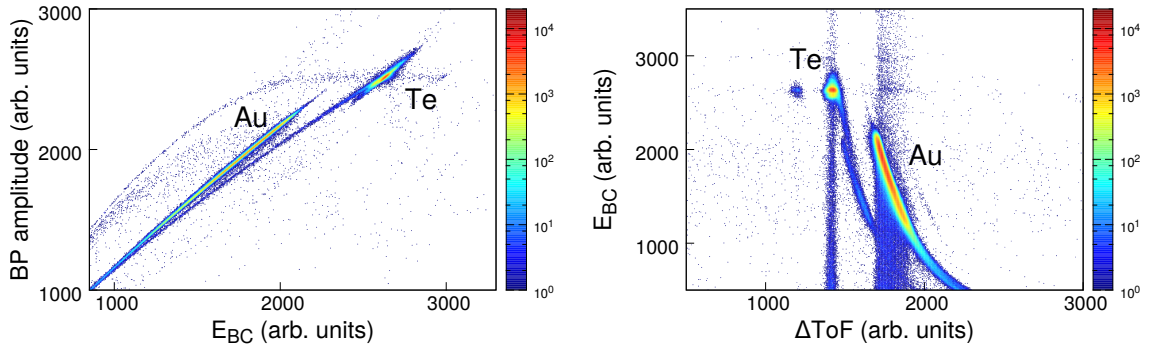

Figure 5.5.: Matrices BP amplitude vs E_{BC} (left) and E_{BC} vs ΔToF (right) for the present experiment. Te-like and Au-like ions are clearly separated.

5.2. Check of the kinematic coincidence

After the calibration of the detectors we checked the right operation of the kinematic coincidence by setting gates and conditions on the spectra produced with quantities measured with PRISMA and plotting the corresponding spectra produced with quantities measured with the second arm. We also checked the angular correlation between the two detectors. Figure 5.6 shows two clarifying examples. In the left panel are plotted two ToF spectra without (blue) and with (red) a condition on Z = 52 in PRISMA. When no condition is

applied, the spectrum displays two peaks associated to both Te-like and Au-like ions; when the condition is applied, only the peak associated to Au ions shows up, as expected.

The right panel shows a comparison between the calculated and the experimental angular correlation between the ions detected in PRISMA (θ_{MCP}) and the associated binary partner in the second arm (θ_{PPAC}). The main branch, labelled in the Figure, corresponds to the case in which the Te-like ions are detected in PRISMA and the Au-like ones in the second arm; the other branch corresponds to the opposite situation. The calculation includes a small excitation of $\sim$ 2.5 MeV for both binary partners, a reasonable value to simulate a contribution from inelastic scattering, which in the inclusive experimental data cannot be disentangled from the pure elastic scattering.

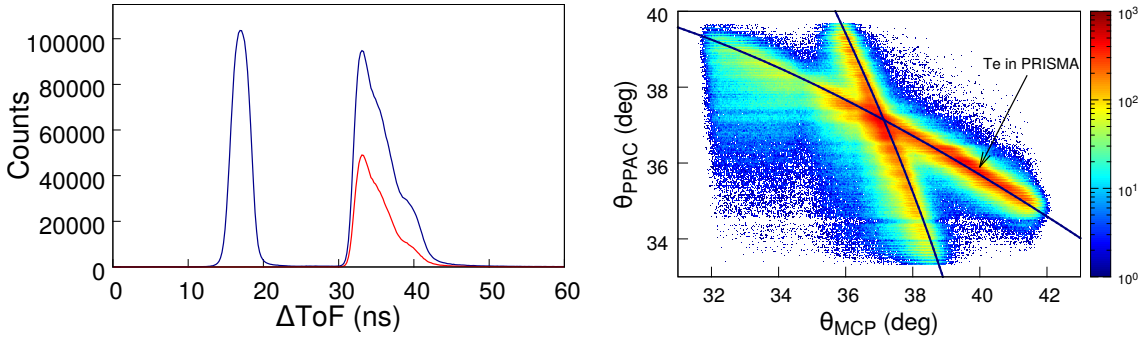

Figure 5.6.: Left: spectra of ΔToF without (blue) and with (red) the condition on Z = 52 in PRISMA. Right: correlation matrix of the in-plane scattering angles of the detected binary partners. The two bands correspond to the two opposite solutions: light partner in PRISMA and heavy partner in the second arm (as labelled in the Figure) and viceversa. The black curves are the results of kinematic calculations where the inelastic excitation of few MeV for both binary partners is included.

Analyzing data collected in coincident detectors and determining coincident yields, one needs to take into account possible limitations of the detection efficiency due to the limited solid angles of the detectors. We show, in Figure 5.7, the calculated angular correlations between light and heavy partner in the case of ground-to-ground states neutron transfers (left) and different Q values involved for the (0n) channel (right).

One can clearly see that the angular correlation is more affected by the Q values involved in the reaction than by the number of transferred nucleons, although it is important to remind that the two quantities are correlated. We discussed in Section 1.1.1 and later showed in Section 4.4.2 how the tails of the Q-value distributions extend towards larger energy losses as more neutrons are transferred. In this context it is interesting to plot, for every neutron transfer channel identified in PRISMA at the scattering angle θ_{MCP}, the corresponding matrices ϕ_{PPAC} versus θ_{PPAC} in the second arm for the associated heavy partner (left panels of Figure 5.8) and the matrices θ_{PPAC} vs θ_{MCP} which correlate the scattering angles of the detected reaction partners (right panels of Figure 5.8).

One can see in both left and right panels that, moving from the (+2n) to the (-5n) channel, the average θ_{PPAC} is slightly decreasing. This behaviour is due to a combination of the neutron

transfers and of the progressively increasing energy loss, as shown in Figure 5.7. For neutron transfer channels the TKEL distributions are not very broad (see Figure 4.22) and the effect of the limited solid angle of the second arm in the present geometry is almost negligible in the determination of the yields in the coincident detectors.

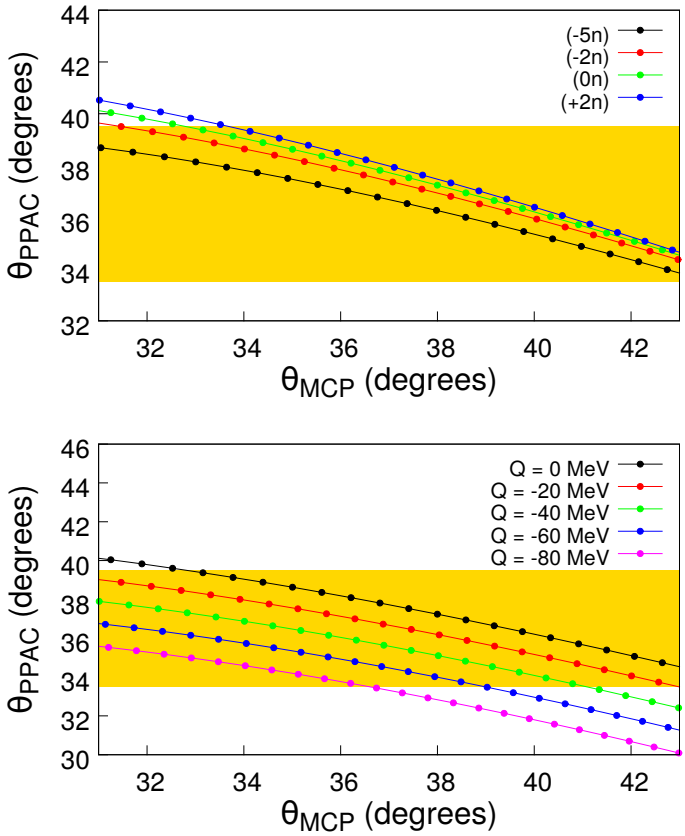

Figure 5.7.: Calculated correlation between in-plane scattering angles for several neutron transfer channels for the ground-to-ground state transitions (top) and by taking into account different Q values (as labeled) in the case of the (0n) channel (bottom). The yellow region indicates the angular region covered by the second arm PPAC.

For proton transfer channels, which are usually associated with larger TKEL, the effect may be more relevant. Since a complete set of Q-value distributions for these channels is not available, as already discussed at the end of Section 4.3, we created Wilczyński plots E_{IC} vs laboratory scattering angle (θ_{MCP}) for the mass-integrated proton transfer channels identified in PRISMA. One can notice how the reaction involves larger and larger kinetic energy losses as more protons are transferred (Figure 5.9 right). This is reflected in a more evident shift of the average θ_{PPAC} of the associated heavy partner detected in coincidence in the second arm, as shown in Figure 5.9 (left). In Figure 5.8 one can also notice a double structure in the (-3n) channel. This has been interpreted as a contamination coming from an A/q repetition of the elastic channel and rejected in the following analysis.

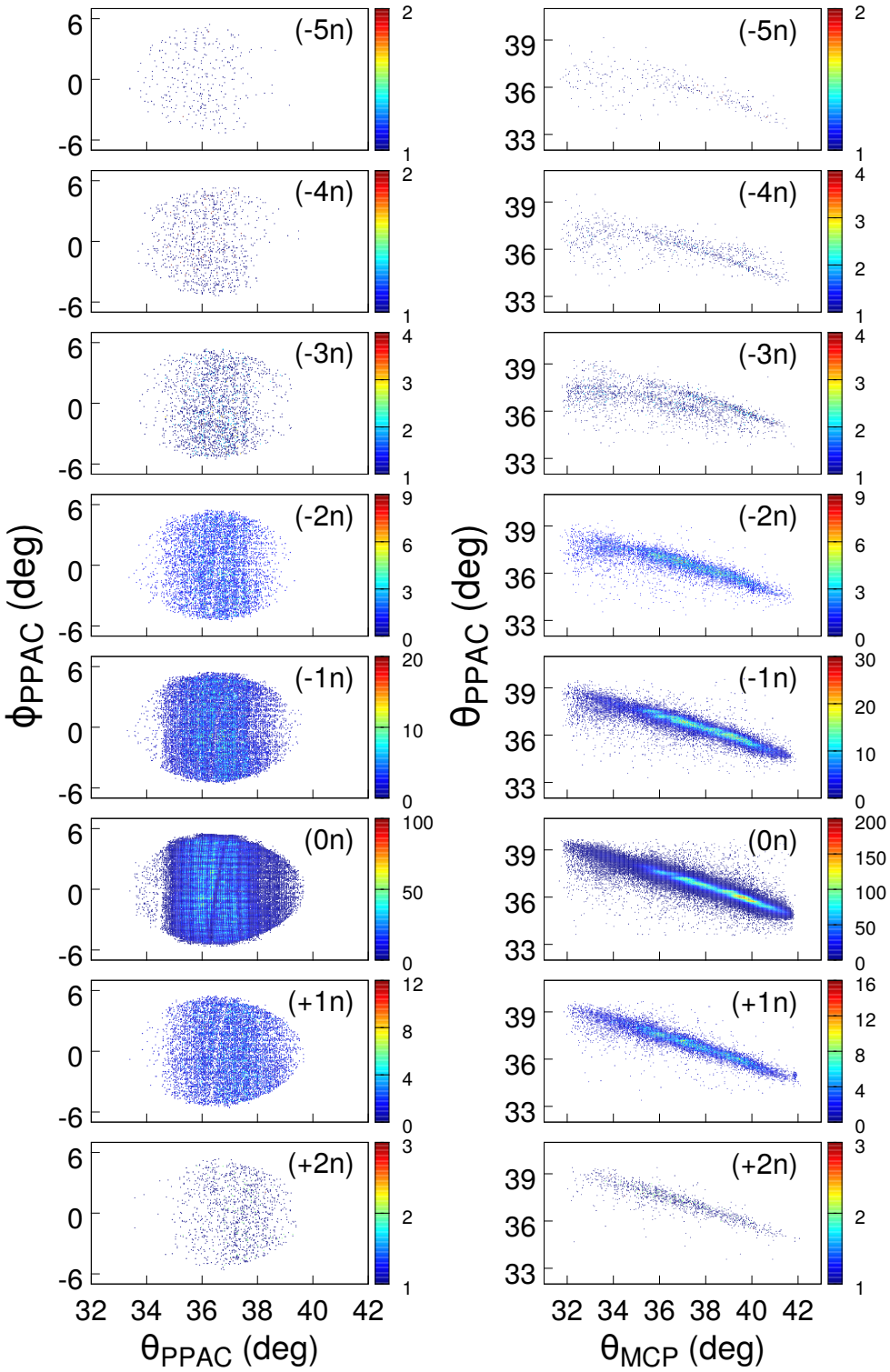

Figure 5.8.: Left panels: detected position of the heavy partner on the PPAC of the second arm. Right panels: correlation between scattering angles of Te ions in PRISMA (θ_{MCP}) and Au ions in the second arm (θ_{PPAC}) for different neutron transfer channels from (-5n) to (+2n).

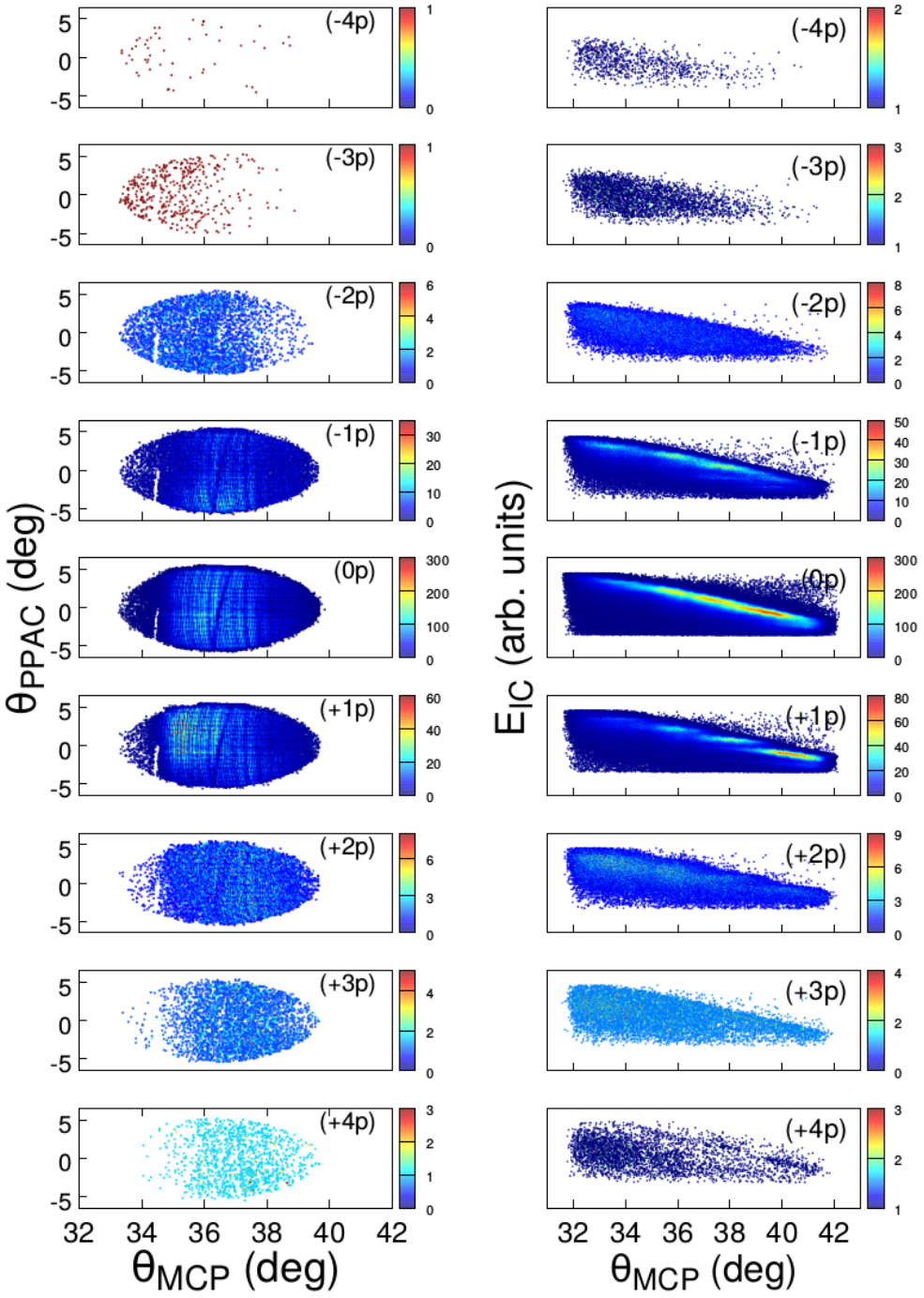

Figure 5.9.: Left panels: detected position of the heavy partner on the second arm PPAC for different proton transfer channels of the light partner, from (-4p) to (+4p). Right panels: Wilczyński plots E_{IC} vs laboratory scattering angle (θ_{MCP}) for the corresponding light partner in PRISMA.

5.3. Mass reconstruction in the second arm

In this Section we will derive several useful relations that have been used to determine the mass of the binary partner in the second arm. When only the scattering angle θ_{MCP} and the ToF in PRISMA are measured, the binary partner mass can be deduced from kinematic expressions derived in the hypothesis of pure binary reaction. The expressions we will now present are determined under the same conditions but the relevant difference is that now the scattering angles and the ToF of the binary partner are not simply deduced but directly measured in the coincident second arm. The onset of secondary processes, which change the pure binary character of the reaction, should then show up as a deviation from the derived equations.

Let us consider once again a binary reaction $1 + 2 \rightarrow 3 + 4$, as depicted in Figure 4.20. By using the kinematic coincidence, m_4 will also be detected (in the second arm) at an angle θ_4. We can define d_3 as the distance between the target and the MCP of PRISMA, d_4 as the distance between the target and the PPAC of the second arm, ToF_3 and ToF_4 the time taken by the particle 3 and 4 to cover d_3 and d_4, respectively, as illustrated in Figure 5.10.

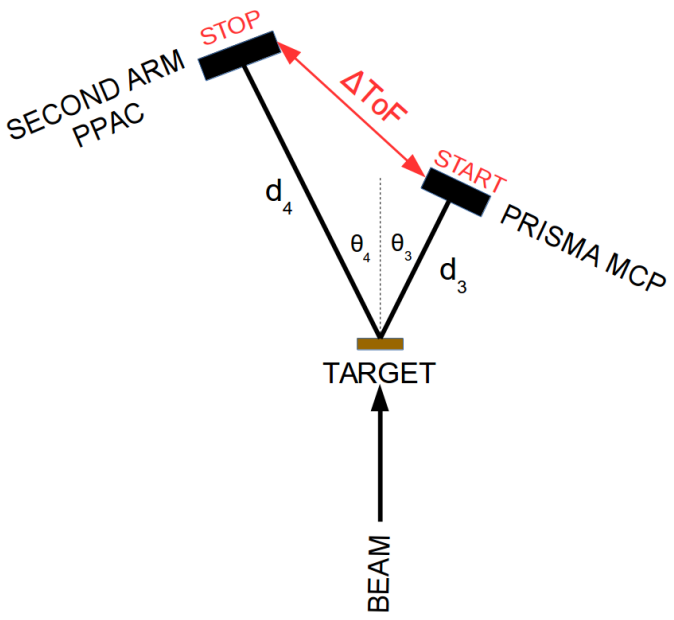

Figure 5.10.: Scheme of the kinematic coincidence. See text for details.

We impose the momentum conservation (see Eq 4.9) and decompose the vector equation onto two axis, one parallel and the other orthogonal to the beam direction:

$$p_1 = p_3 \cos\theta_3 + p_4 \cos\theta_4 \tag{5.1}$$

$$0 = p_3 \sin\theta_3 - p_4 \sin\theta_4 \tag{5.2}$$

where θ_3 and θ_4 are the scattering angles of particles 3 and 4 respectively.

Making explicit p = mv, from (5.2) we have

$$m_1 v_1 = \frac{\sin\theta_4}{\sin\theta_3}\, m_4 v_4$$

We can now substitute in Eq 5.1, reminding that $v_4 = d_4/ToF_4$.

$$p_1 = \frac{m_4\ d_4}{ToF_4}\left(\cos\theta_4 + \frac{\sin\theta_4}{\tan\theta_3}\right) \tag{5.3}$$

We can now solve this equation with respect to m_4 and obtain:

$$m_4 = \frac{p_1}{d_4}\ ToF_4\ \left(\cos\theta_4 + \frac{\sin\theta_4}{\tan\theta_3}\right)^{-1} \tag{5.4}$$

With some easy trigonometric considerations:

$$\begin{aligned}\left(\cos\theta_4 + \frac{\sin\theta_4}{\tan\theta_3}\right)^{-1} &= \frac{\tan\theta_3}{\cos\theta_4\tan\theta_3 + \sin\theta_4} \\ &= \frac{\sin\theta_3}{\cos\theta_4\sin\theta_3 + \cos\theta_3\sin\theta_4} \\ &= \frac{\sin\theta_3}{\sin(\theta_3+\theta_4)}\end{aligned} \tag{5.5}$$

We can then substitute Eq 5.5 in Eq 5.4 and obtain the final relation to determine the binary partner mass (cfr. Ref. [131]):

$$m_4 = \frac{p_1}{d_4}\ \frac{\sin\theta_3}{\sin(\theta_3+\theta_4)}\ ToF_4 \tag{5.6}$$

This simple formula requires the direct measurement of the ToF_4 from the target to the PPAC of the second arm but in the present experiment this information was not available. We could anyway derive it from the other measured quantities in the following way:

- in the hypothesis that the reaction takes place in the center of the target, the distance d_3 was calculated event by event (see Figure 5.11(a));
- the time ToF_3 was calculated as the ratio between d_3 and the velocity $v=\beta c$ measured in PRISMA (see Figure 5.11(b));
- ToF_4 was then given by the sum of the measured ΔToF and the calculated ToF_3 (see Figure 5.11(c)).

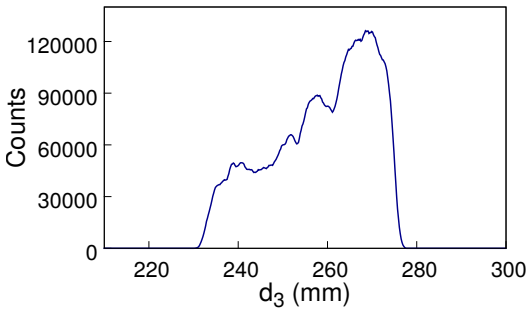

(a) Distance target-MCP of PRISMA.

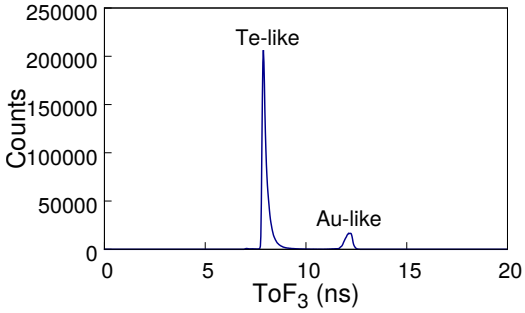

(b) ToF target-MCP of PRISMA.

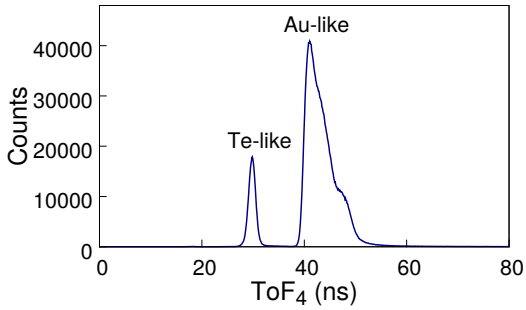

(c) ToF target-PPAC second arm.

Figure 5.11.: Distribution of the distance d_3 between the target and the MCP of PRISMA (top left), the corresponding reconstructed ToF_3 (top right) and the reconstructed ToF_4 between the target and the PPAC of the second arm (see text for details).

Inserting the reconstructed ToF in Equation 5.6, we can determine the mass of the binary partner event by event. Figure 5.12 shows the obtained mass distribution in the second arm. The peaks corresponding to Au-like and Te-like ions are centered around A = 197 and 130, respectively. As expected the mass resolution is rather poor (∼6 a. m. u. FWHM for the heavy partner, $\Delta A/A \sim 1/33$), not sufficient to distinguish the different isotopes.

The mass resolution is mainly determined by the time resolution of the reconstructed ToF_4, being rather small the uncertainties on the angles θ_3, θ_4 and on the distance d_4. As ToF_4 is not measured directly, its resolution is affected by the reconstruction procedure described above and amounts to ∼1 ns. For a value of $ToF_4 \approx 40$ ns for Au-like ions, one can compute a relative uncertainty $\Delta t/t \approx 2.5$ %. From the error propagation formula one obtains for the mass: $\Delta m/m \approx$ 2.5-3 %, which means 5-6 a. m. u. for A∼200. This value is in good agreement with what was observed experimentally.

In the insert of Figure 5.12 a zoom on the heavy partner in logarithmic scale is reported to better illustrate the shape of the mass distribution. One notices that this distribution is not symmetric around A = 197, but displays a tail towards larger values. This higher mass region may be partly populated through a transfer mechanism involving neutron stripping from Te. However, the asymmetry is dominated by other experimental effects, like for instance the tail of the elastic mass peak due to degraded events, the non-linear response of detectors or electronics etc.

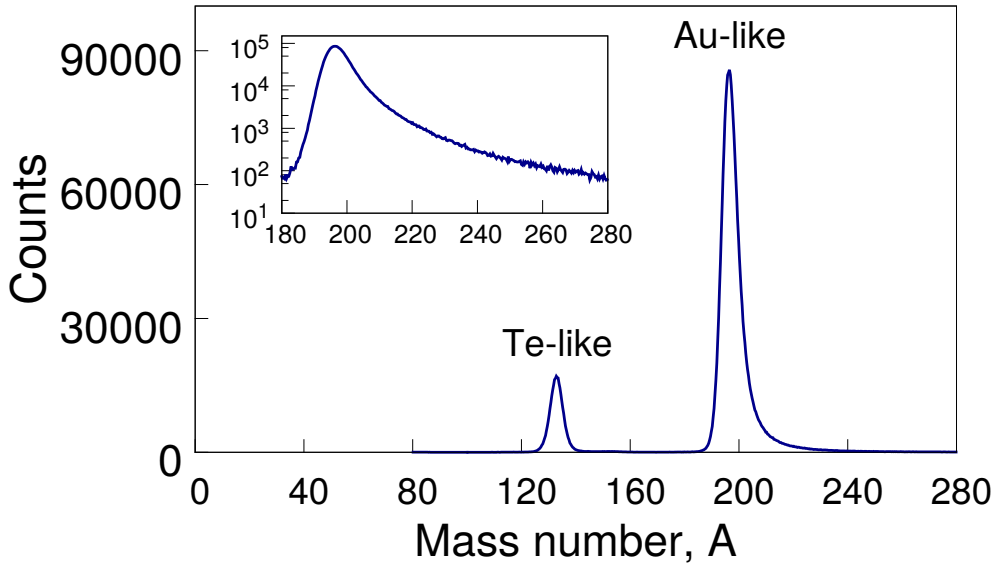

Figure 5.12.: Mass distribution in the second arm obtained with Equation 5.6. Light and heavy reaction products can be clearly distinguished. In the insert is a zoom on the heavy partner in logarithmic scale.

An alternative approach allows to avoid the complicated reconstruction of ToF_4 for the derivation of m_4. Let us define $M = m_1+m_2$ and refer once again to Figure 5.10. We would like to derive an equation for m_4 where ToF_4 does not appear explicitly. From the momentum conservation (Eq. 5.1 and 5.2), reminding that $v_{cm} = p_1/M$, one obtains:

$$p_3 = M v_{\mathrm{cm}} \frac{\sin\theta_4}{\sin(\theta_3+\theta_4)} \tag{5.7}$$

$$p_4 = M v_{\mathrm{cm}} \frac{\sin\theta_3}{\sin(\theta_3+\theta_4)} \tag{5.8}$$

which can be written:

$$ToF_3 = \frac{d_3}{v_3} = \frac{m_3 d_3}{p_3}$$
$$ToF_4 = \frac{d_4}{v_4} = \frac{m_4 d_4}{p_4}$$

This returns for $\Delta ToF = ToF_4\text{-}ToF_3$:

$$\Delta ToF = \frac{m_4 d_4}{p_4} - \frac{m_3 d_3}{p_3} \tag{5.9}$$

This ΔToF is the Time-of-Flight between the MCP of PRISMA and the PPAC of the second arm. We can solve Equation 5.9 for the binary partner mass m_4 and after some easy algebraic passages we obtain:

$$m_4 = \left(M\frac{d_3}{p_3} + \frac{\Delta ToF}{p_3} \right) \left(\frac{d_3}{p_3} + \frac{d_4}{p_4} \right)^{-1} \tag{5.10}$$

We can now subtitute the expressions 5.7 and 5.8 in Equation 5.10 for p_3 and p_4 and we obtain the final expression for the mass in the second arm:

$$m_4 = M \left(\frac{d_3}{\sin\theta_4} + \frac{\Delta ToF \cdot v_{\mathrm{cm}}}{\sin(\theta_3+\theta_4)} \right) \left(\frac{d_3}{\sin\theta_4} + \frac{d_4}{\sin\theta_3} \right)^{-1} \tag{5.11}$$

The use of Eq. 5.11 instead of Eq. 5.6 allows to determine the mass distribution of the binary partner detected in the second arm with improved mass resolution (∼4.5 a. m. u. or $\Delta A/A \sim 1/43$). The comparison between the mass peaks relative to Au-like ions obtained with the first method (black) and the alternative approach (red) is shown in Figure 5.13. Since the integrals of the peaks are the same, the difference in mass resolution is immediately evident.

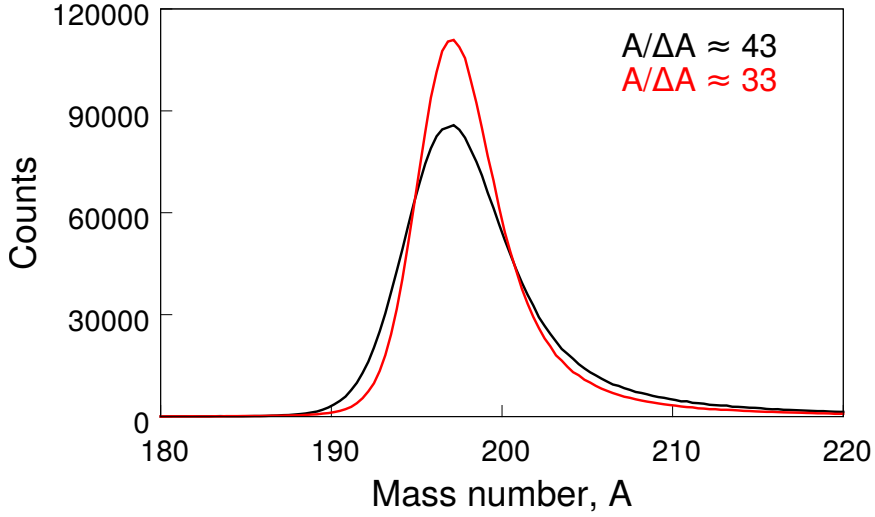

Figure 5.13.: Comparison between the mass peaks relative to Au-like ions obtained with the first method (black) and the alternative approach (red). The corresponding mass resolutions are indicated. See text for details

5.4. Q-value determination using the kinematic coincidence

In the present experiment, which involved two kinematic coincident set-ups, the masses and scattering angles of both binary partners were measured. The relevant difference between this and other measurements performed so far is that in this case the light partner of the reaction is completely identified in A and Z. This has the important consequence that the behaviour of the heavy partner is not deduced on a large scale but directly measured, though with lower resolution, as a function of the number of transferred nucleons. In particular, besides the TKEL distributions reported in Figure 4.22, additional ones could be derived from the coincident information of PRISMA and the second arm. The analysis of such distributions and the comparison with those obtained without exploiting the coincidence can be crucial to better understand whether the reaction maintains its binary character after the transfer of many nucleons.

Starting once again from the equations of energy and momentum conservation and with the same formalism used so far, the reaction Q value can be determined with simple passages. From Equation 5.6 we can solve for v_3 and v_4 and obtain:

$$v_3 = \frac{m_1 v_1}{m_3} \frac{\sin\theta_4}{\sin(\theta_3+\theta_4)}$$
$$v_4 = \frac{m_1 v_1}{m_4} \frac{\sin\theta_3}{\sin(\theta_3+\theta_4)}$$

The following equations are now straightforward:

$$E_3 = \frac{1}{2} m_3 v_3^2 = \frac{m_1 v_1}{m_3} \frac{\sin^2\theta_4}{\sin^2(\theta_3+\theta_4)} \tag{5.12}$$
$$E_4 = \frac{1}{2} m_4 v_4^2 = \frac{m_1 v_1}{m_4} \frac{\sin^2\theta_3}{\sin^2(\theta_3+\theta_4)} \tag{5.13}$$

Substituting 5.12 and 5.13 in Equation 4.7 we finally obtain the desired expression:

$$Q = \frac{m_1 E_1}{m_3 m_4} \frac{m_3 sin^2\theta_3 + m_4 sin^2\theta_4}{sin^2(\theta_3+\theta_4)} - E_1 \quad . \tag{5.14}$$

From Equation 5.14 we see that the Q value in this case depends only on the scattering angles and the detected masses of the binary partners.

The TKEL distributions for the different neutron transfer channels from (-5n) to (+2n) obtained with Equation 5.14 are shown in Figure 5.14. At a first glance these distributions look similar in shape to those of Figure 4.22, where only the information of PRISMA was used. This may suggest that the reaction mantains its binary character also after the transfer of several neutrons. We will come back on the comparison between the two TKEL distributions in Chapter 6.

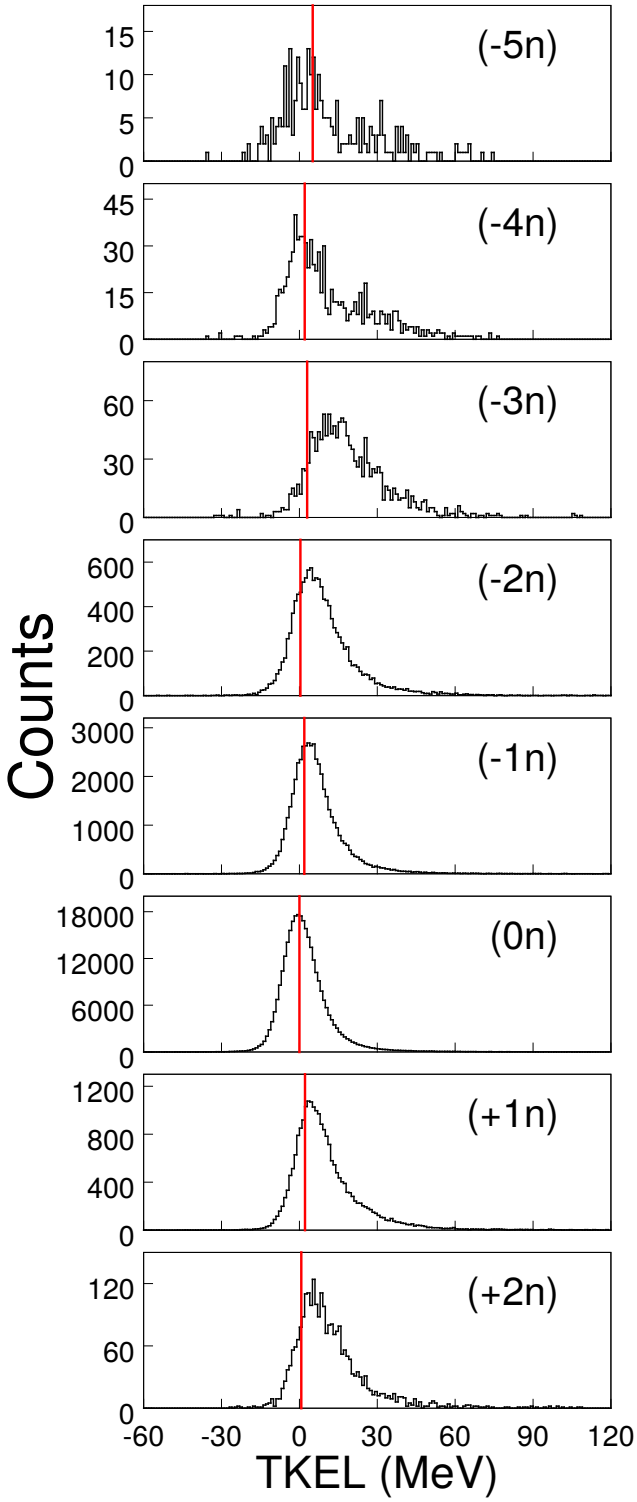

Figure 5.14.: TKEL distributions for Te neutron transfer channels from (-5n) to (+2n) determined through the simultaneous detection of both binary partners in the coincident detectors.

6 Experimental results and discussion

6.1. The light partner

The study of the behaviour of the light partner was the first goal of the experiment. We felt important to investigate whether the use of a neutron-rich "light" target could enhance the neutron stripping process and how important the effect of neutron evaporation is for this medium-heavy system, even when the bombarding energy is slightly above the Coulomb barrier. In Chapter 4 we outlined the procedure to obtain the absolute yields for neutron and proton transfer channels. We could identify neutron transfer channels for Te (Z = 52) down to 6 neutrons in the stripping side and up to 3 neutrons in the pick-up side. Moreover proton transfer channels up to 3-4 protons in both the stripping and pick-up sides could be partially disentangled. For the measured channels most of the transfer flux can be integrated with one magnetic field setting only, given the large acceptance of PRISMA. Due to the grazing character of the reaction, the angular distributions at these bombarding energies are bell-shaped and cover almost the same angular range. This is true in particular for the neutron transfer channels, where the TKEL distributions are weakly channel dependent. Thus in the analysis we assumed that the experimental relative yields are proportional to the total cross sections. To learn more about the character of the final populated channels we compared them with state-of-the-art theoretical models, in particular with the GRAZING code presented in Section 1.2.3.

The experimental yields, extracted with a multigaussian fit of the Te mass spectrum (see Figure 4.19), are shown in Figure 6.1 (points) together with the predictions of GRAZING without (black) and with (red) the inclusion of the effect of neutron evaporation. Since the absolute cross sections have not been measured, we need to normalize the experimental yields to the calculations. In previously measured systems it was demonstrated that GRAZING describes particularly well one-neutron transfer channels (see Section 1.2.3) and the (+1n) channel was usually chosen for the normalization because it is the channel in principle less affected by evaporation. In this work we decided instead to use the (-1n) channel, i.e. ^{129}Te, for the normalization due to the fact that at this low bombarding energy the evaporation does not significantly alter the cross section of one-neutron transfer channels. In addition, the (-1n) channel was better separated and its yield could be determined with higher accuracy (see Fig. 4.19). The normalization has been kept the same for all other transfer channels.

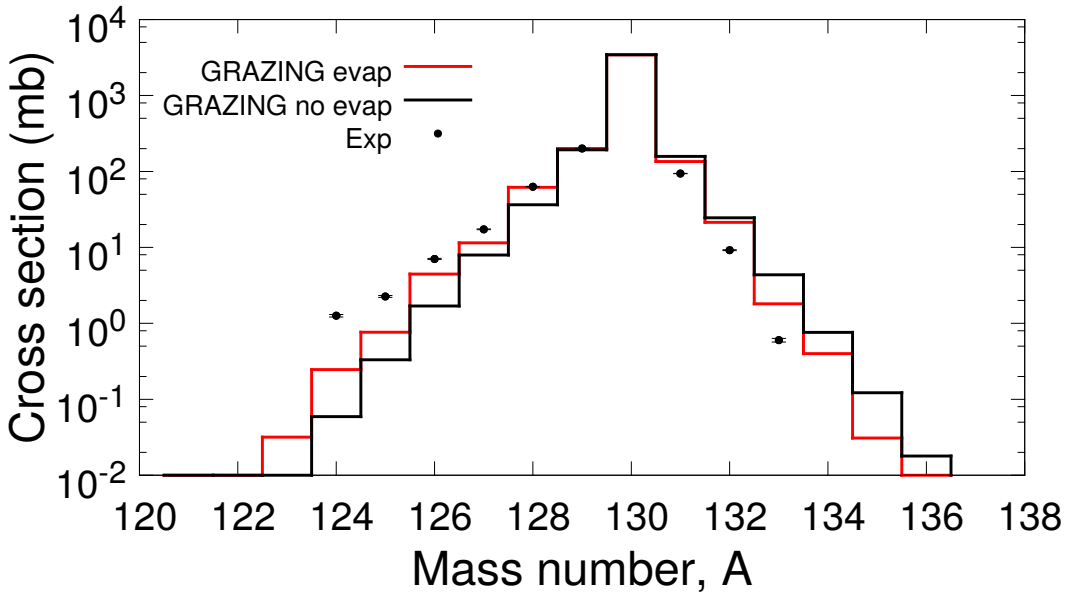

Figure 6.1.: Comparison between experimental data (black points) and GRAZING calculations with (red histogram) and without (black histogram) the inclusion of evaporation. The errors in the plot are only statistical.

Form the comparison shown in Figure 6.1, one can notice that the channels involving few neutron transfers are well reproduced for both pick-up and stripping. In the neutron stripping region, as more neutrons are stripped the experimental cross sections tend to be larger than the GRAZING calculations. When the neutron stripping is involved we have to keep in mind that the neutron evaporation may play a very important role. This is the reason why in Figure 6.1 the GRAZING calculations with and without the effect of evaporation have been plotted. One can see that the cross section of, for example, the (-6n) channel including the effect of the evaporation is factor 2-3 higher than the case without evaporation, still not sufficient to match the experimental cross sections. A similar situation for the neutron stripping channels has been observed in the recently measured ^{136}Xe+^{198}Pt [66] and ^{136}Xe+^{238}U [128] systems, where the most neutron-rich stable ^{136}Xe isotope was used.

To illustrate better similarities and differences between this and our measurements, we report in Table 6.1 bombarding energies in the center-of-mass system and Bass barriers for the three systems, while in Figure 6.2 we show the comparison of the cross sections for the channels involving neutron stripping for the indicated systems. These channels are important for the population of the (primary) neutron-rich heavy partners. We see that the cross sections for the ^{197}Au+^{130}Te system drop off quite regularly, while those of the other two cases tend to flatten out after the transfer of few neutrons. The different behaviour is likely due to the larger energy losses, in turn leading to a larger effect of neutron evaporation, in the ^{136}Xe+^{198}Pt and ^{136}Xe+^{238} systems. Indeed the bombarding energy in the ^{197}Au+^{130}Te case was much closer to the Coulomb barrier. This reflects in lower transfer cross sections but at the same time lower contribution of secondary processes. If this is true also for the heavy partner, the choice of a low bombarding energy could turn out to be very promising to

produce neutron-rich heavy nuclei with higher survival probability to competitive processes.

System	E_{cm} (MeV)	V_B (MeV)	E_{cm}/V_B
^{136}Xe+^{198}Pt	640	415	1.54
^{136}Xe+^{238}U	596	478	1.25
^{130}Te+^{197}Au	424	407	1.04

Table 6.1.: Bombarding energies in the center-of-mass system, E_{cm}, and Bass barriers, V_B, for the indicated systems.

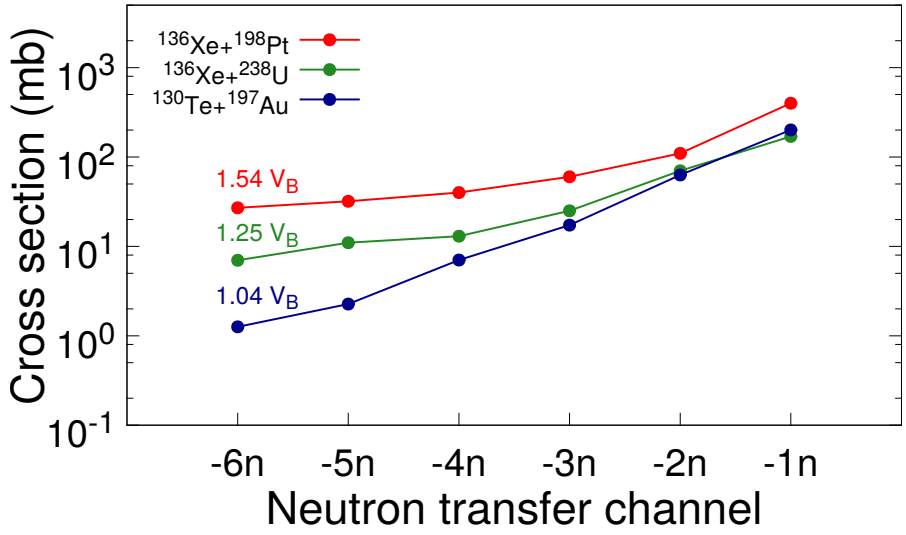

Figure 6.2.: Experimental total cross sections for neutron stripping channels for the systems ^{197}Au+^{130}Te (this work), ^{136}Xe+^{198}Pt (from Ref. [66]) and ^{136}Xe+^{238}U (from Ref. [128]) at the indicated energies in the center-of-mass system. The lines are to guide the eye.

Additional insight can be gained by studying the TKEL distributions, where the excitation energies of both partners are embedded. As outlined in Section 5.4, the TKEL were constructed assuming a pure binary process and imposing the momentum conservation. In Figure 6.3 (left panels) we show the obtained TKEL distributions for the indicated neutron-transfer channels using only the information of PRISMA (taken from Figure 4.22). In the same Figure (right panels) are also shown the TKEL distributions obtained by requiring an additional condition on the kinematic coincidence (taken from Figure 5.14). They display, at least for few neutron transfers, a well defined peak, as expected in a regime where quasi-elastic processes dominate.

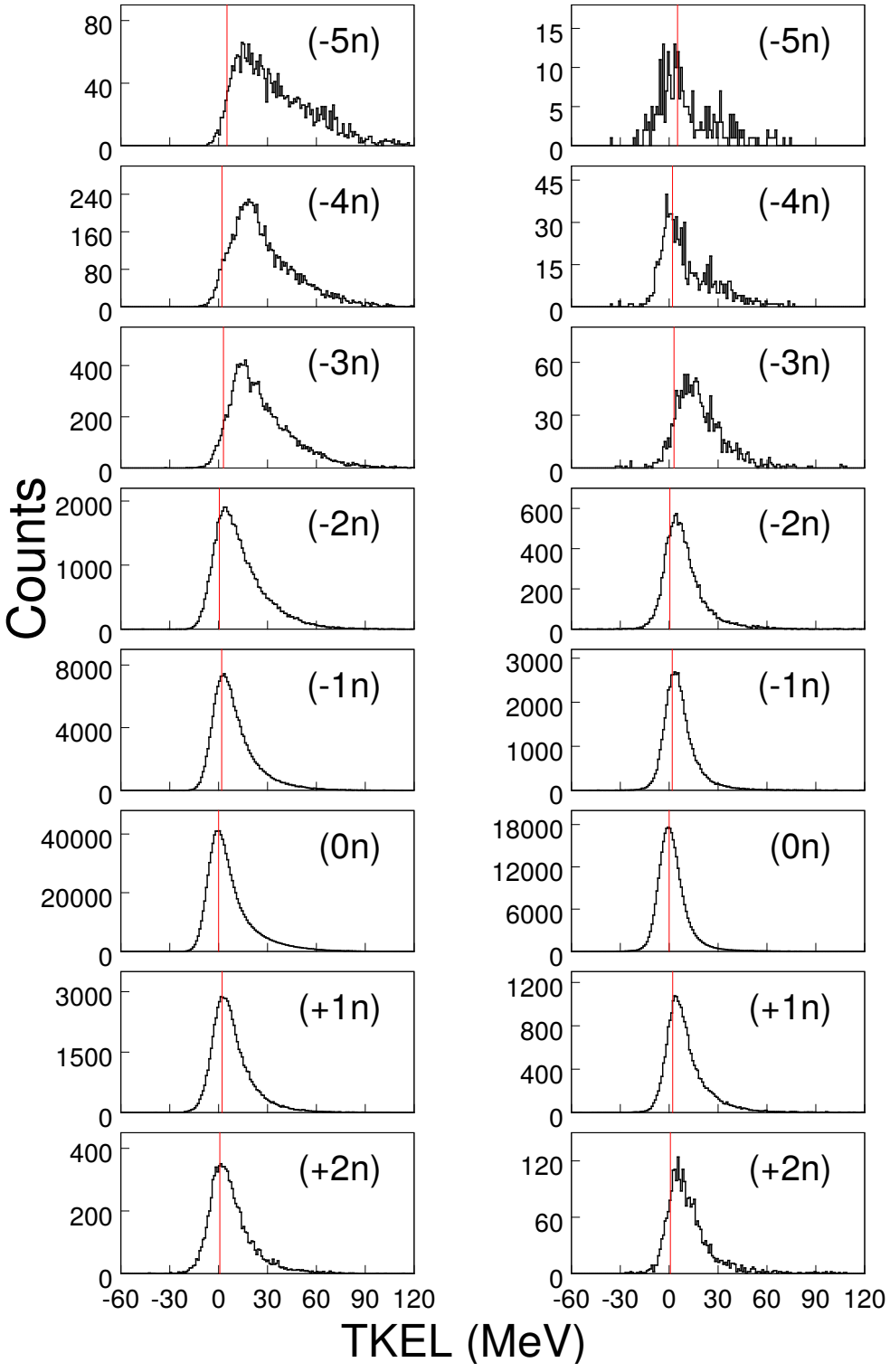

Figure 6.3.: TKEL distributions for neutron-transfer channels of Te (Z = 52) from (-5n) to (+2n) using only the information of PRISMA (left) and using the coincident information of the second arm (right).

As more neutrons are transferred, a tail towards larger energy losses starts to develop and deviations between experimental and theoretical cross sections show up (see Figure 6.1), indicating that secondary processes may play a role. This discussion demonstrates the importance of a careful consideration of the bombarding energy to balance between having high primary cross sections, though strongly affected by secondary processes, or, reversely, preserving most of the primary yields, though at the cost of lower absolute values. This aspect is very relevant in particular when the attention is focused on the behaviour of the corresponding binary heavy partner, in connection with the production of neutron-rich nuclei.

Besides the neutron stripping channels, also the proton pick-up ones are leading to the primary neutron-rich heavy partners. In this context, we extracted the mass-integrated cross sections for each element via a multigaussian fit of the distribution shown in Figure 4.14, and compared them with the GRAZING calculations. The absolute normalization has been kept the same as for (-1n) channel (^{129}Te). The results are shown in Figure 6.4.

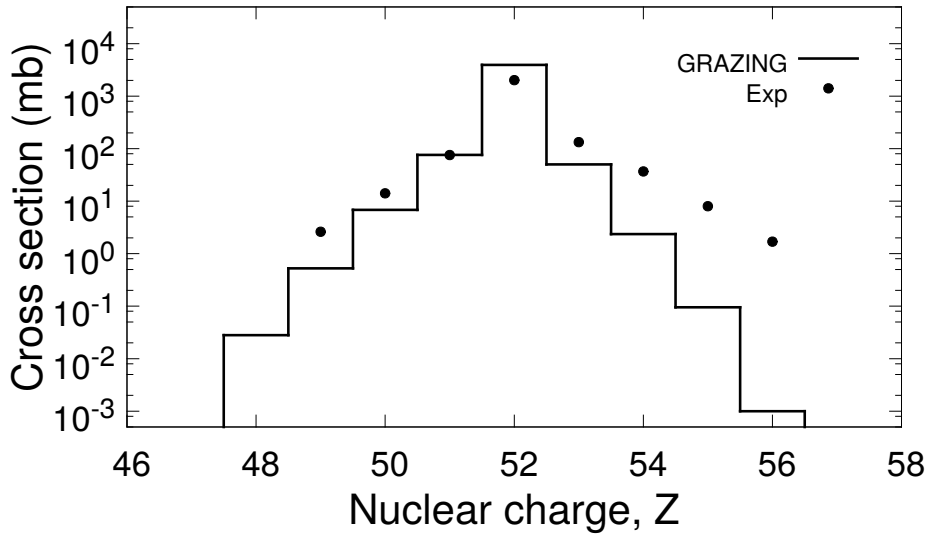

Figure 6.4.: Comparison between experimental data (points) and GRAZING calculations (histogram) for mass-integrated proton transfer channels. The errors in the plot are only statistical and do not exceed the points size.

We showed in Figure 4.21 that the proton stripping path should be favoured with respect to the pick-up one according to optimum Q-value considerations, and this is confirmed by the trend of the GRAZING calculations of Figure 6.4. Experimental data have instead an opposite trend. The proton stripping side behave similarly to what already observed in previously studied systems, i.e. a modest theoretical underprediction for the (-2p) channel with growing differences showing up as more protons are stripped. The (-1p) channel is instead very well reproduced by the calculations, a remarkable result. On the pick-up side the theoretical underpredictions are already present for the (+1p) channels, becoming more pronounced as more protons are added. This is likely due to the fact that proton transfer channels usually involve larger DIC components compared to neutron transfer ones, and these may not be fully taken into account by GRAZING, as discussed in Section 1.2.3 and

1.2.2 in connection with Eq. 1.8. Similar results have been also emphasized in the very few systems studied so far where proton pick-up channels have been identified in high resolution measurements, e.g. in the ^{136}Xe+^{198}Pt[66] and ^{40}Ar+^{208}Pb [23] cases. We stress that proton transfer processes are much less understood than the neutron transfer ones. This is due to the scarce availability of experimental data and to the less studied single particle level density and corresponding form factors, in particular when the treatment of the reaction process involves large modifications of the trajectories of entrance and exit channels.

6.2. The heavy partner

We outlined in Chapter 5 the procedure to analyze the data of the coincident second arm and determine the mass of the heavy binary partner. The mass resolution turned out to be $\Delta A/A \sim 1/43$, which is not sufficient to separate the different Au isotopes. The kind of spectrum shown in Figure 5.12 is what one tipically gets from the information of two detectors set in coincidence where angles and relative timing are measured, but both reaction partners are not identified with high A and Z resolution. We discussed a similar technique in Section 1.4. It is only when a coincidence with a high-resolution spectrometer is set that one can construct a mass-mass correlation matrix and infer about the behaviour of the heavy partner. This is demonstrated in Figure 6.5, where the reconstructed mass of Au-like ions is correlated with that of each Te isotope detected in PRISMA.

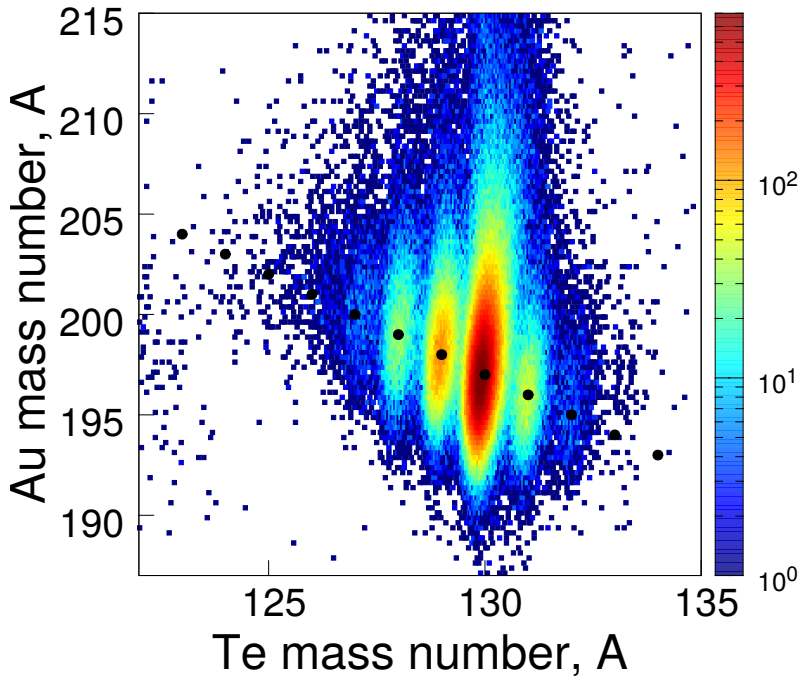

Figure 6.5.: Mass-mass correlation matrix of Te isotopes detected in PRISMA and the heavy partner detected in coincidence with the second arm. The black dots indicate the correlated masses of the primary neutron transfer channels.

In Figure 6.5 one sees that to each Te isotope is associated the correct mass centroid of the corresponding binary partner. In the presence of secondary processes, in particular neutron evaporation which in our case is likely to be dominant compared to other processes, like transfer-induced fission or quasi-fission, one expects that the mass distribution will widen while preserving the position of the centroids. In fact nucleon evaporation induces a spread in the direction of the momentum of the primary heavy recoil around its central value, which is associated to a pure binary process as assumed in Equation 5.11. Therefore the final width of the mass distribution is a convolution of the experimental resolution and the effect of evaporation.

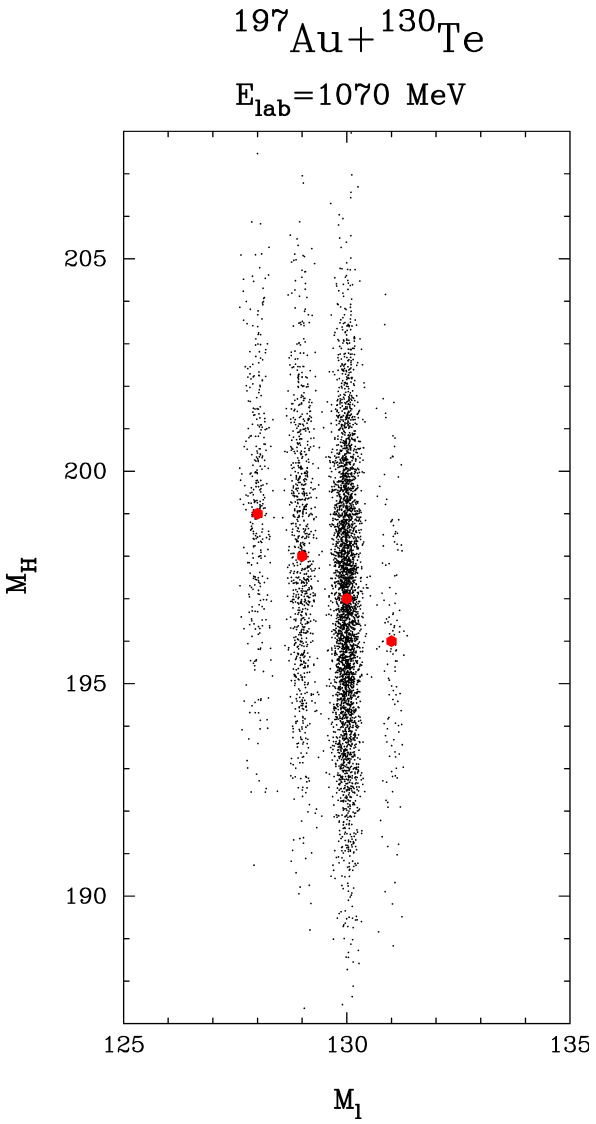

Figure 6.6.: Monte Carlo calculated mass-mass correlation matrix. The red dots indicate the centroids of the distributions.

To extract information on the evaporation one needs to compare the measured distribution with a Monte Carlo calculated one. In the Monte Carlo simulation, the evaporation of neu-

trons has been simulated by assuming a uniform energy distribution with a value of 1.5 MeV, which means that every evaporated neutron carries an energy of 1.5 MeV. It incorporates a successive evaporation of neutrons and takes into account the experimental mass resolution. The results are reported in Figure 6.6. The simulation reproduces the experimental width of the mass distributions with up to three evaporated neutrons. Although we cannot separate the different Au isotopes, we can infer that the masses of the detected heavy products do not differ by more than three units in neutron number from those of the primary ones. On the basis of these findings, the experimental mass distributions (also reported in Figure 6.7) clearly demonstrates that neutron-rich heavy nuclei in the vicinity of ^{197}Au have been detected.

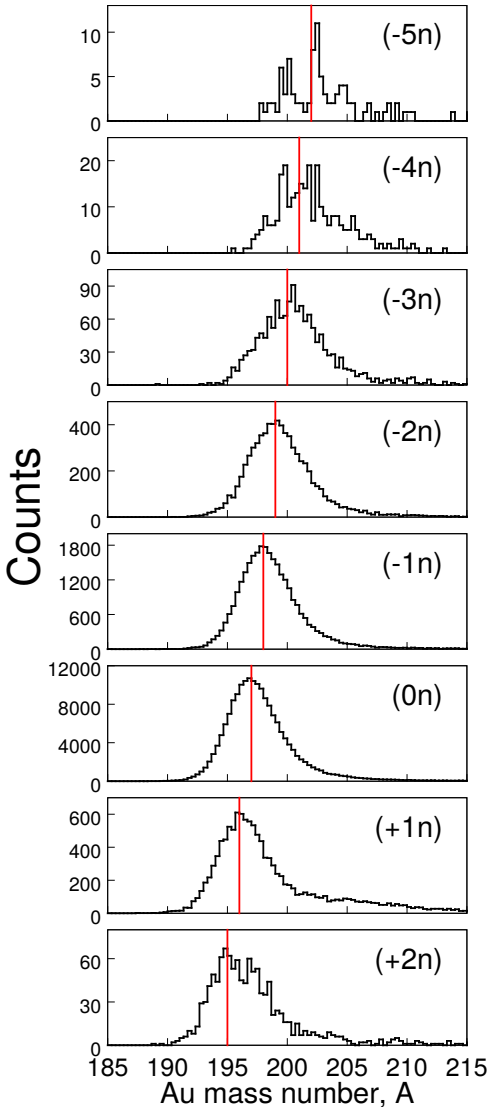

Figure 6.7.: Spectra of mass distributions of the heavy partner gated on each Te isotope (indicated in parenthesis). The red lines are located at the mass of the corresponding primary heavy partner.

In discussing the TKEL spectra of the left part of Figure 6.3 obtained with PRISMA alone we could study their evolution as function of the number of transferred neutrons. These TKEL spectra in general do not provide information on the behaviour of the final heavy partner, i.e. after the transfer process has occurred. By requiring the kinematic coincidence we have the possibility to follow up to what extent these reactions reflect a binary character. In the right part of Figure 6.3 we show the same TKEL spectra for the neutron transfer channels, constructed by requiring such an additional coincidence condition. We point out that the spectra taken in coincidence for the events with very large TKEL are partially affected by the geometrical cuts in the second arm. One sees that the distributions, at least up to the transfer of three neutrons, develop in a similar way and peak roughly at the same centroids as the corresponding ones of PRISMA alone. This strongly supports the binary character of the reaction. Moreover, the tails develop in a similar way in both cases. The development of these tails towards large energy losses when more neutrons are transferred indicates the presence of large deformation in these binary events, characteristic of processes involving the transfer of many nucleons.

In order to have a comparison with GRAZING calculations also for the heavy partner, from the mass-mass correlation matrix of Figure 6.5 we integrated the coincidence yields for each isotope of Te and attributed them to the single mass of the Au isotope determined by the centroid of the mass distributions. These yields have been transformed into absolute cross sections keeping the same normalization constant chosen for the Te isotopes, which was obtained normalizing the (-1n) channel to the GRAZING calculations. The experimental results are displayed in Figure 6.8 together with the GRAZING calculations.

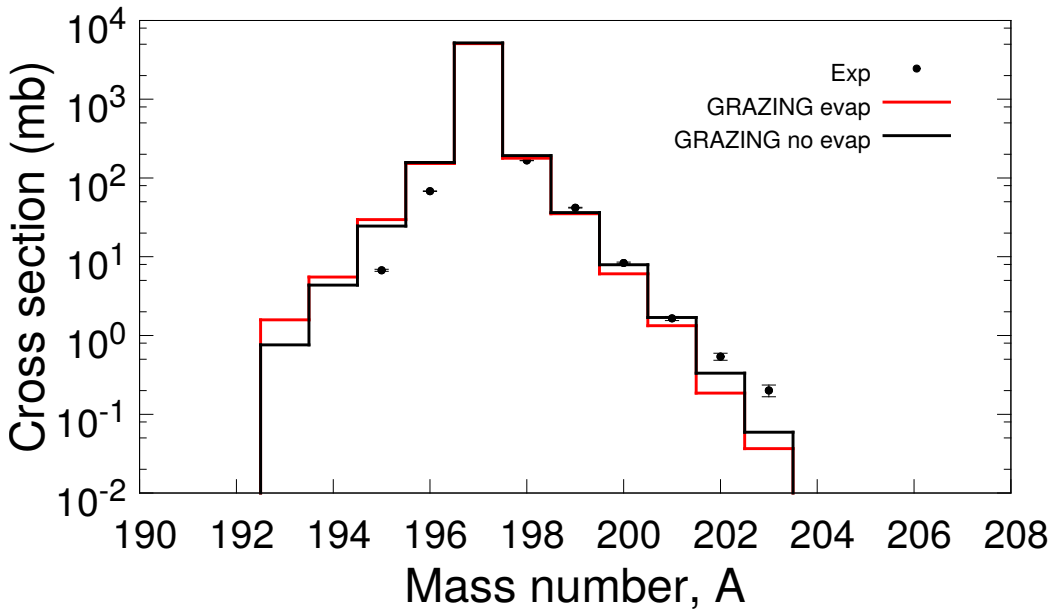

Figure 6.8.: Comparison between experimental yields for the heavy partner (black points) and GRAZING calculations with (red histogram) and without (black histogram) the inclusion of evaporation. Experimental data are normalized to the GRAZING cross section for the (-1n) channel of Te. The errors in the plot are only statistical.

The experimental cross sections on the higher mass region (i.e. neutron stripping from Te) are quite well reproduced by GRAZING, at least up to the transfer of 4 neutrons. We notice also that the data tend to be overestimated on the lower masses (neutron pick-up from Te). The observed good agreements or differences in absolute values between data and calculations may not be the most relevant feature, taking into account the uncertainties in the normalization procedure where the overall efficiency of the two detectors in the kinematic coincidence are embedded in a very complex way. Much more interesting and pertinent to the present discussion is the observation that the slope of the experimental data, especially on the higher mass regions, is well reproduced by the calculations. This fact leads us to conclude that the reaction preservs its main quasi-binary character up to a significant amount of neutron transfers. Any secondary process beyond "simple" evaporation, like a fission mechanism, would have altered significantly the experimental coincident yields and generated a different slope compared to calculations. As already pointed out before, the limited mass resolution for the Au isotopes does not allow to infer about the specific mass distributions generated by the evaporation. However, the fact that GRAZING calculations with and without evaporation do not differ so much toghether with the found similar experimental and theoretical cross sections slopes suggest that the primary mass yields should be quite close to those attributed to the mass centroids of Figure 6.5. This, consistently with the results of the Monte Carlo calculations from which we inferred that the masses of the detected heavy products do not differ by more than three units in neutron number from those of the primary ones.

We finally made an effort to extract the correlation matrix for the channels involving proton transfer. In spite of the fact that the Z separation is quite limited (see also Figure 4.14) and that we integrated over the different isotopes for each nuclear charge, an interesting correlation has been found, as shown in Figure 6.9. The figure is the projected mass distribution from the kinematic coincidence for each nuclear charge identified in PRISMA. The vertical red lines represent the mass of the pure proton transfers. One sees that in the proton pick-up channels from Te, leading to lower Z in the binary heavy partner, the mass distributions are slightly shifted toward neutron numbers higher than the one associated to the pure proton transfers. One also notices that in the proton stripping side from Te, leading to higher Z in the binary heavy partner, most of the transfer flux is associated with its higher mass regions.

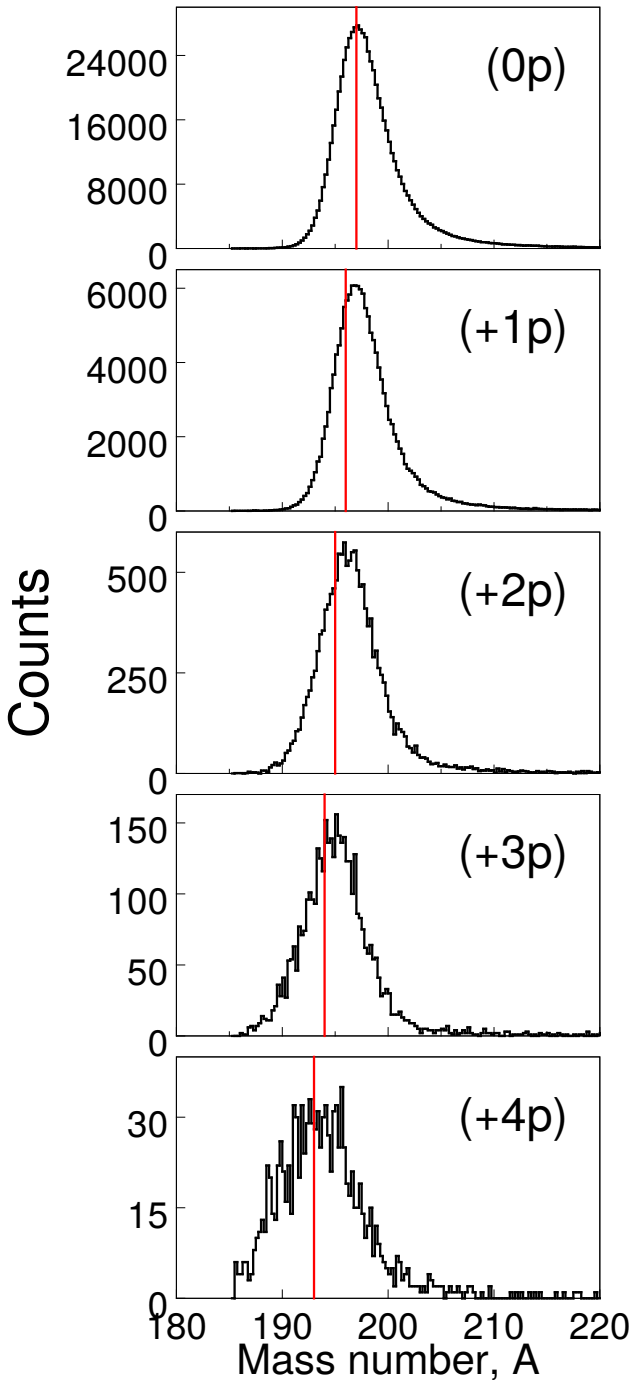

Figure 6.9.: Mass projections of the matrix nuclear charge in PRISMA vs mass in the second arm constructed from the kinematic coincidence. The Z of the transfer channels corresponding to the Te-like ions are indicated. The vertical red lines correspond to the mass of the pure proton transfer channels.

7 Conclusions and further perspectives

In this thesis we studied the multinucleon transfer reaction ^{197}Au+^{130}Te at $E_{lab} = 1.07$ GeV in inverse kinematics to determine A, Z, Q-value distributions and cross sections of the transfer reaction products and compare them with the predictions of theoretical models. With the use of neutron-rich nuclei, besides neutron pick-up and proton stripping channels, also the predicted population of neutron stripping and proton pick-up channels has been experimentally tested. This is an important path leading to the production of neutron-rich heavy nuclei, in particular approaching the N = 126 region of the nuclear chart. We used the full performance of the PRISMA spectrometer to detect, with high resolution and efficiency, the light reaction products. At the same time a kinematical coincident second arm has been employed in order to measure, with lower resolution, the behaviour of the heavy partner in terms of average mass distributions and yields. To have cleaner data and to facilitate their interpretation in the comparison with theoretical predictions, we chose a rather low bombarding energy. In this way the fragments should be produced with quite low excitation energy and the effect of secondary processes consequently reduced, although at the price of modest transfer cross sections, especially for proton transfer channels.

With PRISMA a proper analysis of Te-like ions had to be followed to disentangle neutron and proton transfer channels from the overwhelming elastic+inelastic channel. Empirical corrections were applied in order to achieve a mass resolution of $\Delta A/A \sim 1/240$ which allowed to derive absolute yields for neutron transfer channels from (-6n) to (+3n). For proton transfers, with about 10 times less cross sections, we could extract the mass-integrated yields corresponding to each nuclear charge from (-3p) to (+4p). We compared the experimental yields with the GRAZING model for transfer reactions, which was already successfully applied for lower-mass systems. For neutron transfer the comparison showed a quite good agreement between experimental data and calculations. For proton transfer the model is able to reproduce quite well the stripping channels but largely underestimates the pick-up ones. The PRISMA data have been consistently matched with those of the second arm, where Au-like ions have been detected. This method, which makes use of a particle-particle coincidence in which one of the two devices is a high-resolution mass spectrometer, has been here employed for the first time. The inverse kinematics conditions helped to detect these Au-like ions with energies much higher than for the direct kinematics case at the corresponding grazing angles and to completely distinguish light and heavy reaction products detected in the second arm.

In the analysis we implemented the second arm in the PRISMA software routine and verified the correct functioning of the kinematic coincidence. We reconstructed the mass of the heavy partner by assuming a binary character of the reaction. The obtained mass resolution in the second arm is $\Delta A/A \sim 1/43$ for Au-like ions. We correlated the mass of the Te isotopes identified in PRISMA and the mass distributions of the associated Au-like ions detected in the second arm. We found a good agreement between the experimentally extracted cross sections for the heavy transfer products and the theoretical predictions of GRAZING, from which we could also assess that the reaction maintains its (quasi) binary character up to the transfer of several neutrons, consistently with the behaviour of the TKEL distributions determined with and without imposing the coincidence condition.

The results of the present experiment have shown that the method here employed is very promising for this kind of studies. The simultaneous identification of the light partner of the reaction with high resolution and the detection of the corresponding heavy partner gives the possibility to follow in a comprehensive way the evolution of the reaction mechanism as more nucleons are transferred. From this and from the comparison with other previously measured systems of similar mass, we could infer that the choice of a low bombarding energy reflects in a lower contribution of secondary processes, which is in general a relevant issue for the population of neutron-rich heavy nuclei.

The detection method here used can in principle give quantitative information on the contribution of neutron evaporation as a function of the number of transferred nucleons. In the present experiment the mass resolution in the second arm was not sufficient to distinguish different Au isotopes and the sensitivity to neutron evaporation was limited to 3-4 neutrons. In forthcoming experiments the use of a longer ToF for the binary heavy partner may improve considerably the mass resolution, allowing to improve the sensitivity up to 1-2 neutrons. To this end, it may be relevant to measure the direct ToF between the target and the PPAC of the second arm through the installation of a second MCP detector. It was also demonstrated that the use of digital electronics provides a better Z resolution and the possibility to measure the range of the ions in the BC in a simple way, thus improving the identification of the reaction products.

The use of the present detection set-up is extremely promising for forthcoming experiments involving heavier beams, like for example Pb and U. The study of the evolution of the reaction mechanism and the determination of the production cross sections in these mass regions of the nuclear chart may give important information also on the population of actinides and trans-actinides, which are recently receiving particular attention. Of course very important will be to adapt the present technique for experiments using radioactive beams, like those expected within the next few years from the new facilities like SPES at LNL and SPIRAL2 at GANIL. These studies could also benefit from the use of coincident γ detectors for the investigation of nuclear structure properties. First step in this direction has been recently performed with the installation of a $LaBr_3$:Ce array on the PRISMA scattering chamber which will be soon employed for γ-particle-particle coincidences. When dealing with very heavy ions, the use of a second arm could be useful to "clean" the γ spectra from the effect of secondary processes, at least for channels populated with quite high cross sections.

A

Appendix: implementation of the second arm in the PRISMA analysis routine

In the present analysis the second arm has been included as a PRISMA detector in the *PrismaManager* routine, which processes the information coming from all the PRISMA detectors in a consistent way. In this Appendix we will report the C++ code which was created to implement the second arm inside the *PRISMAlibraries* for the kinematic coincidence. It consists of two files: *BraggChamber.h*, which is the header file where the class BraggChamber is defined together with all its functions and variables, and *BraggChamber.cpp* which contains the main body of the code.

```
1
2  /*    BraggChamber.h
3
4     Author: Franco Galtarossa (franco.galtarossa@lnl.infn.it)    */
5
6  #include <string>
7  #include <vector>
8  #include "SystemsOfUnits.hh"
9  #include "ConfigurationFile.hh"
10 #include "prismaDetector.hh"
11 #include "MassTable.h"
12
13 #ifndef BRAGGCHAMBER_H_
14 #define BRAGGCHAMBER_H_
15 using namespace std;
16 using namespace NuclearPhysicsSystem;
17
18 class BraggChamber: public prismaDetector {
19
20 public:
21     BraggChamber(string="bragg.conf", int=1 , int=6);
22     virtual ~BraggChamber();
23
24 private:
25   int   read_configuration ();
26   void init_data ();
27   const double amu = 931.494061 *MeV;
28
29  public:
30   int   validate_event ( std::vector<detData*>& );
```

```
31    void process_event  ( std::vector<detData*>& );
32
33   private:
34    void get_bragg_angles ();
35    void calc_bragg_mass(double bragg_beta, double theta_mcp_1, double bragg_theta);
36
37    //relevant parameters
38  private:
39    int   bragg_index[6];
40    int   ind_bragg_ppacx;         // x ppac
41    int   ind_bragg_ppacy;     // y ppac
42    int   ind_bragg_ic;        // ionization chamber
43    int   ind_bragg_bp;        // Bragg peak
44    int   ind_bragg_corset;    // corset (not present now)
45    int   ind_bragg_tof;       // TOF
46
47    //Mass table
48    MassTable* MyMassTable;
49
50    // Calibration files
51    private:
52      string  tof_cal_file;
53      string  xppac_cal_file;        // x mcp
54      string  yppac_cal_file;        // y mcp
55
56    // Bananas files
57    private:
58      string ban_file;
59      int    ban_res_x;
60      int    ban_res_y;
61      int    load_banana;
62
63    //Gain and offset
64    private:
65      double  xppac_gain;
66      double  xppac_offs;
67      double  yppac_gain;
68      double  yppac_offs;
69      double  tof_gain;
70      double  tof_offs;
71
72    //Thresholds
73    private:
74      int   ic_lower_threshold;
75      int   bp_lower_threshold;
76      int   ic_upper_threshold;
77      int   bp_upper_threshold;
78
79    private:
80      double bragg_ppacX;
81      double bragg_ppacY;
82      double bragg_tof;
83      double bragg_ppac_target_dist;   // distance from target, 885 mm
84      double bragg_angle;      // 36.5 degrees
85      double beam_energy; // 1070 MeV
86      double beam_mass; // 197Au
87      double beam_zed; //79
88      double bragg_ppac_radius; //50 mm
89      double bragg_target_dist; //calculated event-by-event
90      double bragg_theta;
91      double bragg_phi;
92      double mb;
93      double delay;
```

```
94      double bragg_mass;
95      double bragg_beta;
96      double rotx, roty, rotz;
97      double dx, dy, dz;
98
99    public:
100     inline double get_bragg_ppacX() { return bragg_ppacX; };
101     inline double get_bragg_ppacY() { return bragg_ppacY; };
102     inline double get_bragg_tof() { return bragg_tof; };
103     inline double get_bragg_theta() { return bragg_theta; };
104     inline double get_bragg_phi() { return bragg_phi; };
105     inline double get_bragg_target_dist() { return bragg_target_dist; };
106     inline double get_bragg_mass () { return bragg_target_dist; };
107     inline double get_delay () { return delay; };
108     inline double get_bragg_rotx () { return rotx; };
109     inline double get_bragg_dy () { return dy; };
110 };
111
112 #endif /* BRAGGCHAMBER_H_ */
```

```
/* BraggChamber.cpp

   Author: Franco Galtarossa (franco.galtarossa@lnl.infn.it) */

#include "BraggChamber.h"

BraggChamber::BraggChamber(string conf_file, int ndet, int npar) {

    n_det = ndet;
    n_par = npar;
    //read the configuration and initialize
    theFile = new ConfigurationFile(conf_file.c_str());
    if (this->read_configuration() > 0)
        this->init_data();

}

BraggChamber::~BraggChamber() {
    delete theFile;
    delete theBanManager;
    theCalManager.clear();
    valid.clear();
}


int BraggChamber::read_configuration() {

    valid_conf = 0;

    bragg_index[0] = theFile->get_int("ind_bragg_ppacx",  0);
    bragg_index[1] = theFile->get_int("ind_bragg_ppacy",  1);
    bragg_index[2] = theFile->get_int("ind_bragg_ic",  2);
    bragg_index[3] = theFile->get_int("ind_bragg_bp",  3);
    bragg_index[4] = theFile->get_int("ind_bragg_corset",  4);
    bragg_index[5] = theFile->get_int("ind_bragg_tof",  5);

    ind_bragg_ppacx = bragg_index[0];
    ind_bragg_ppacy = bragg_index[1];
    ind_bragg_ic = bragg_index[2];
    ind_bragg_bp = bragg_index[3];
    ind_bragg_corset = bragg_index[4];
    ind_bragg_tof = bragg_index[5];

    ////////////////////////////////////
    ////  Experiment configurations  ////
    ////////////////////////////////////

    string fileMassTable = theFile->get_string("mass_table_file", "/media/data/↩
        PRISMA/197Au+130Te/local/ConfigFiles/MyCal/massnumbers.cal");
    MyMassTable = new MassTable(fileMassTable);

      ////////////////////////////////
      ////  Geometrical properties  ////
      ////////////////////////////////

    bragg_ppac_target_dist = theFile->get_double( "bragg_ppac_target_dist", 884.5)*↩
        mm;
    bragg_angle = theFile->get_double( "bragg_angle", 36.5)*degree;
    bragg_ppac_radius = theFile->get_double( "bragg_ppac_radius", 50.)*mm;

      ////////////////////////////////
      ////     Calibration files    ////
```

```
61        ////////////////////////////////
62
63      xppac_cal_file = string( theFile->get_string( "xppac_cal_file", "/media/data/↩
            PRISMA/197Au+130Te/local/ConfigFiles/MyCal/bragg_Xppac.cal") );
64      yppac_cal_file = string( theFile->get_string( "yppac_cal_file", "/media/data/↩
            PRISMA/197Au+130Te/local/ConfigFiles/MyCal/bragg_Yppac.cal") );
65      tof_cal_file = string( theFile->get_string( "tof_cal_file", "/media/data/PRISMA↩
            /197Au+130Te/local/ConfigFiles/MyCal/bragg_tof.cal") );
66
67
68
69        ////////////////////////////////
70        ////      Bananas files       ////
71        ////////////////////////////////
72
73      ban_file = string( theFile->get_string( "ppac_banana", "/media/data/PRISMA/197Au↩
            +130Te/local/ConfigFiles/MyBan/bragg_ppac_banana.ban") );
74      ban_res_x = theFile->get_int("ban_res_x",  4096);
75      ban_res_y = theFile->get_int("ban_res_y",  4096);
76
77      load_banana = theFile->get_int("load_banana", 1);
78
79        ////////////////////////////////////
80        ////       Gain and offset        ////
81        ////////////////////////////////////
82
83      xppac_gain = theFile->get_double( "xppac_gain", 1.);
84      xppac_offs = theFile->get_double( "xppac_offs", 0.);
85
86      yppac_gain = theFile->get_double( "yppac_gain", 1.);
87      yppac_offs = theFile->get_double( "yppac_offs", 0.);
88
89      tof_gain = theFile->get_double( "tof_gain", 1.);
90      tof_offs = theFile->get_double( "tof_offs", 0.);
91
92        ////////////////////////////////////
93        //// Thresholds for data validity ////
94        ////////////////////////////////////
95
96      ic_lower_threshold = theFile->get_int("ic_lower_threshold", 0.);
97      bp_lower_threshold = theFile->get_int("bp_lower_threshold", 0.);
98      ic_upper_threshold = theFile->get_int("ic_upper_threshold", 3500.);
99      bp_upper_threshold = theFile->get_int("bp_upper_threshold", 3500.);
100
101     valid_conf = 1;
102     return valid_conf;
103
104 }
105
106 void BraggChamber::init_data() {
107
108     // Bananas
109     theBanManager = new banManager( ban_file, ban_res_x, ban_res_y );
110
111      // Calibrations
112     theCalManager.resize(n_par);
113
114     theCalManager[ind_bragg_tof] = new calManager(tof_cal_file);
115     theCalManager[ind_bragg_ppacx] = new calManager(xppac_cal_file);
116     theCalManager[ind_bragg_ppacy] = new calManager(yppac_cal_file);
117
118     theCalManager[ind_bragg_ppacx]->setGain   ( xppac_gain );
119     theCalManager[ind_bragg_ppacx]->setOffset ( xppac_offs );
```

```
120
121     theCalManager[ind_bragg_ppacy]->setGain   ( yppac_gain );
122     theCalManager[ind_bragg_ppacy]->setOffset ( yppac_offs );
123
124 }
125
126 int BraggChamber::validate_event(std::vector<detData*>& theEvent) {
127
128     int nvalid = 0;
129     int ok_thresh;
130     detData* aData = NULL;
131     err_code = 0;
132
133     // at the beginning, nothing is valid ...
134     valid.clear();
135     processed_event = 0;
136     valid_evt = 0;
137
138     //Dummy values
139     bragg_ppacX = 0.;
140     bragg_ppacY = 0.;
141     bragg_tof = 0.;
142     bragg_theta = 0.;
143     bragg_phi = 0.;
144
145      // empty buffer -> not valid!
146     if( theEvent.size() < 1 ) {
147         err_code = 4;
148         return -1;
149     }
150
151     //bananas
152     if(load_banana == 1){
153             for (int ii = 0; ii < (int) theEvent.size(); ii++) {
154                     aData = theEvent[ii];
155                     if (theBanManager->inside(aData->num_det(), (*aData)[↩
                            ind_bragg_ppacx], (*aData)[ind_bragg_ppacy]) < 1) {
156                         aData->set_valid(0);
157                         nvalid--;
158                         continue;
159                     } else {
160                         aData->set_valid(1);
161                         nvalid++;
162                         valid.push_back(ii);
163                         continue;
164                     }
165             }
166     }
167
168      if( nvalid < 1 ) {
169         err_code = 8;
170         return -1;   // nothing to do...
171      }
172      if( nvalid > 1 ) {
173         err_code = 12;
174         return -1;   // should accept only multiplicity 1
175      }
176
177       // if nvalid == 1: at this point, we can save temporary values of x, y
178      for(int ii=0; ii<(int)valid.size(); ii++) {
179         aData = theEvent[valid[ii]];
180         bragg_ppacX += (*aData)[ind_bragg_ppacx];
181         bragg_ppacY += (*aData)[ind_bragg_ppacy];
```

```
182       }
183
184       nvalid = 0;
185
186         for(int ii=0; ii<(int)theEvent.size(); ii++ ) {
187             aData = theEvent[ii];
188             if( !aData->is_valid() ) continue;  // missing PPAC
189
190             ok_thresh = 0;
191             if( (*aData)[ind_bragg_ic] > ic_lower_threshold && (*aData)[ind_bragg_bp]↩
                    > bp_lower_threshold &&
192               (*aData)[ind_bragg_ic] < ic_upper_threshold && (*aData)[ind_bragg_bp] <↩
                      bp_upper_threshold ) ok_thresh++;
193
194             if(ok_thresh < 1) {
195                 aData->set_valid(0);
196                 nvalid--;
197                 continue;
198             } else {
199                 aData->set_valid(1);
200                 nvalid++;
201             }
202         }
203
204         if( nvalid < 1 ) {
205           err_code = 16;
206           return -1;   // nothing to do...
207         }
208
209         //Just to check, nvalid should be 1
210         if( nvalid > 1 ) {
211               err_code = 20;
212               return -1;   // nothing to do...
213             }
214
215       //se invece Ã¨ valido...
216       valid_evt = nvalid;
217
218       return valid_evt;
219
220 }
221
222 void BraggChamber::process_event(std::vector<detData*>& theEvent) {
223
224     int ii, run = 0;
225     detData* aData = NULL;
226     double dummy_tof;
227     delay = 48.+16.26/* * ns*/;
228
229     bragg_tof = 0.;
230
231     for(ii=0; ii<(int)valid.size(); ii++) {
232
233         aData = theEvent[valid[ii]];
234         dummy_tof = theCalManager[ind_bragg_tof]->getCalValue( run, aData->num_det()↩
                , (*aData)[ind_bragg_tof]/* * ns */) - delay;
235         bragg_tof += dummy_tof;
236
237       }
238
239       bragg_tof = tof_gain * bragg_tof + tof_offs;
240
241       for(ii=0; ii<(int)valid.size(); ii++) {
```

```
242
243             aData = theEvent[valid[ii]];
244             aData->set( ind_bragg_ppacx, theCalManager[ind_bragg_ppacx]->getCalValue( ↩
                    run, aData->num_det(), (*aData)[ind_bragg_ppacx]) * mm );
245             aData->set( ind_bragg_ppacy, theCalManager[ind_bragg_ppacy]->getCalValue( ↩
                    run, aData->num_det(), (*aData)[ind_bragg_ppacy]) * mm );
246         }
247
248         bragg_ppacX = 0.;
249         bragg_ppacY = 0.;
250
251          for(int ii=0; ii<(int)valid.size(); ii++ ) {
252              aData = theEvent[valid[ii]];
253              bragg_ppacX += (*aData)[ind_bragg_ppacx];
254              bragg_ppacY += (*aData)[ind_bragg_ppacy];
255          }
256
257          this->get_bragg_angles();
258
259          processed_event = 1;
260 }
261
262 void BraggChamber::get_bragg_angles() {
263
264     // y -> beam direction
265     // Bragg chamber at 36.5 with respect to the beam.
266
267     rotx = 0.; roty = 0.; rotz = 0.;
268          dx = 0.; dy = 0.; dz = 0.;
269     double new_x = 0., new_y = 0., new_z = 0.;
270     Vector3D dummy;
271
272     new_x = bragg_ppacX/mm;
273     new_y = -dummy.Z();
274     new_z = bragg_ppacY/mm;
275
276     rotx = cos(bragg_angle/rad)*new_x + sin(bragg_angle/rad)*new_y;
277     roty = sin(bragg_angle/rad)*new_x + cos(bragg_angle/rad)*new_y;
278     rotz = 0.;
279
280     dx = bragg_ppac_target_dist/mm * sin(bragg_angle/rad) - rotx;
281     dy = bragg_ppac_target_dist/mm * cos(bragg_angle/rad) + roty;
282     dz = new_z + rotz;
283
284     dummy = Vector3D( dx, dy, dz );
285     bragg_target_dist = sqrt(pow(dx,2) + pow(dy,2) + pow(dz,2));
286
287     bragg_theta = acos(dy/bragg_target_dist); //in rad
288     bragg_phi = M_PI - atan(dz/dx); //in rad
289
290 }
```

B

Appendix: test of digitizers for γ spectroscopy with HPGe detectors

In parallel with the data analysis presented in this thesis, a study of the performances of different CAEN digitizers for γ-spectroscopy measurements with HPGe detectors was performed in collaboration with CAEN [132]. This work led to the writing of an application note that we report here.

Introduction

The most recent arrays for nuclear γ-ray spectroscopy are mainly composed of high-purity Germanium (HPGe) detectors, since they have proved to be the best detectors in terms of energy resolution, thus allowing to distinguish also nuclear levels that differ in energy for just few keVs. Resolution is not only affected by the particular detector and the specific experimental conditions but also by the electronics employed for signal read-out. In recent years more and more facilities have started to employ digital electronics, due to the large number of potential benefits it can provide with respect to the analog one. FPGA can indeed simulate the behaviour of a complex electronic chain (amplifier, discriminator, ADC, etc.) by means of dedicated algorithms for the signal processing: this of course reduces the number of electronic modules needed to perform the measurement, thus simplifying the integration of the acquisition system. Moreover the use of digital electronics can facilitate the synchronisation of more acquisition channels, therefore it is particularly suitable when working with segmented detectors (see for example Ref. [124]), and allows to operate at higher counting rates with respect to analog electronics.

CAEN has developed different spectroscopy solutions in very compact desktop digital pulse processing devices for gamma and X-ray spectroscopy. In collaboration with the INFN Laboratori Nazionali of Legnaro (LNL), one of the four Italian national laboratories, the performances in terms of energy resolution of two Multi-Channel Analyzers (MCA) and two digitizers have been compared.

CAEN Multi-Channel Analyzers are mainly conceived as devices for high-resolution energy measurements: they are provided with 14-bit resolution ADCs with adjustable dynamic ranges, low sampling rate and high impedance (1 kΩ). Digitizers on the other hand have

higher sampling rate and lower impedance (50 Ω), even if the other characteristics of the ADCs are the same.

Experimental setup

We start by briefly reporting some other specifications of the devices used in this comparison (additional information can be found in Ref. [132]):

- **DT5780**: MCA integrating 2 independent 16k-channels digital MCA and HV/LV power supply capabilities. Sampling rate: 100 Ms/s. Available dynamic ranges: 0.6, 1.4, 3.7 and 9.5 V.

- **DT5770**: MCA integrating a 16k-channels digital MCA and a LV power supply capability. Sampling rate: 100 Ms/s. Available dynamic ranges: 1.25 and 2.5 V.

- **DT5725**: digitizer integrating 8 independent 16k-channels digital MCA. Sampling rate: 250 Ms/s. Available dynamic ranges: 0.5 and 2.0 V.

- **DT5730**: digitizer integrating 8 independent 16k-channels digital MCA. Sampling rate: 500 Ms/s. Available dynamic ranges: 0.5 and 2.0 V.

The characterization of MCAs and digitizers and the study of their behaviour with the change of several parameters and experimental conditions was performed making use of a large set of HPGe detectors which are currently used in nuclear physics experiments at LNL. These devices could also be compared with analog electronics thanks to the presence in our laboratory of a full analog chain composed of high and low voltage, shaping amplifier and MCA. Figure B.1 shows a picture with the typical set-up for measurements in our dedicated laboratory. From the left to the right we can see detector 1 with a radioactive source, detector 2 (for description of detectors see text below), the two MCAs, the laptop with the MC2A software for acquisition and analysis of spectra, the rack with all the modules of the analog electronic chain.

In this specific comparison we used the following set-up.

Detectors

- **Detector 1**: n-type HPGe detector with an intrinsic efficiency of 78.8%;

- **Detector 2**: n-type HPGe detector with an intrinsic efficiency of 36% shielded by a Beryllium window 0.5 mm thick. This detector is more suitable for measurements with low-energy γ rays.

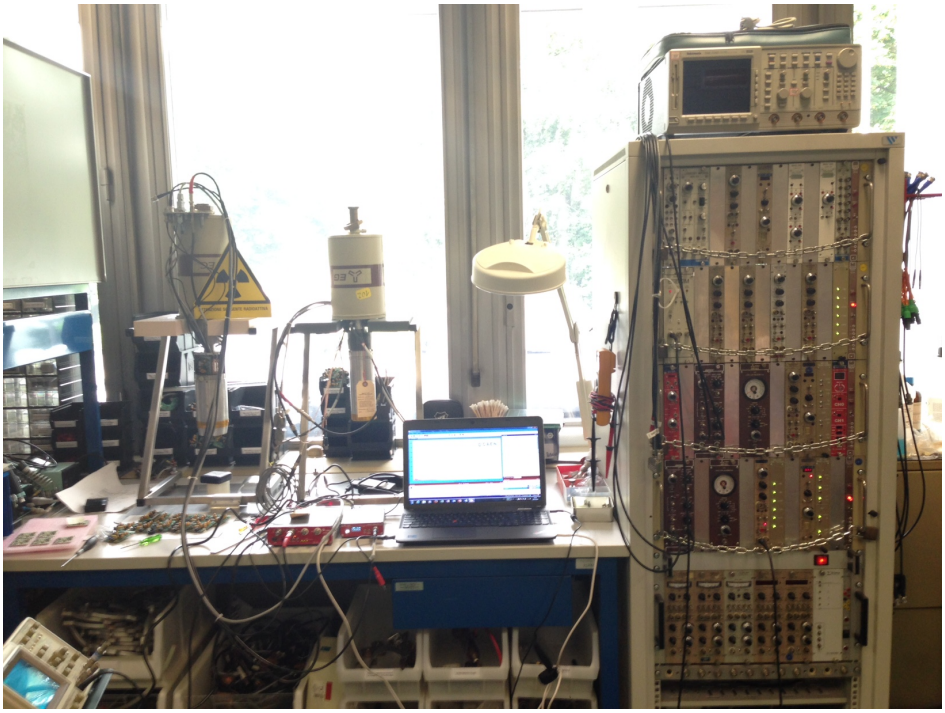

Figure B.1.: Experimental set-up for the measurements described in this application note. See text for details.

Sources

- a low-intensity ^{60}Co source (nominal activity = 1 μCi)
- a high-intensity ^{60}Co source (nominal activity = 10 μCi);
- a high-intensity ^{133}Ba source (nominal activity = 10 μCi);

In Figure B.2 two typical spectra obtained with the two sources used in these measurements are reported.

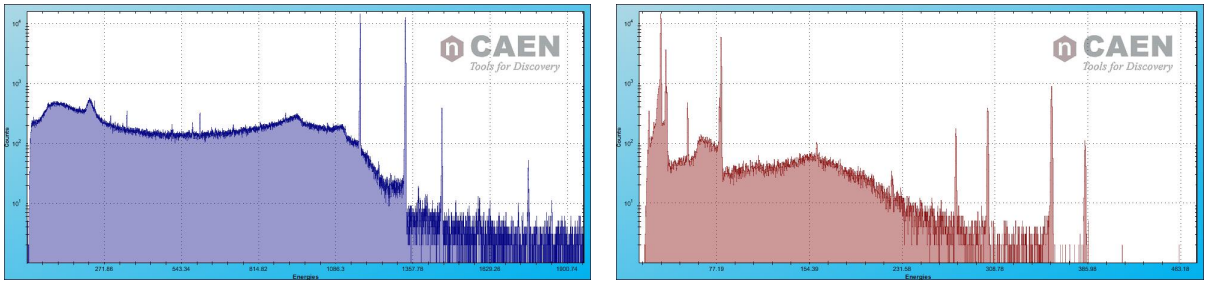

Figure B.2.: On the left: ^{60}Co spectrum acquired with detector 1. On the right: ^{133}Ba spectrum acquired with detector 2. Both spectra are plotted in logarithmic scale. For the ^{133}Ba spectrum the x-axis range has been reduced to the low-energy region.

Acquisition parameters and measurements

The aim of the analysis is to determine which of the four spectroscopy devices has the best performance in terms of energy resolution and it is therefore necessary to choose properly the acquisition parameters. When the counting rate on the detector is not too high (< 10 kHz) and the signals from the preamplifier have an amplitude of about 150 mV, which is usually the case in these kind of applications, the best resolution can be obtained with the smallest ADC input range available and with both long shaping times (rise time of the trapezoid filter = 9 μs and flat top = 1.5 μs) and high number of samples to calculate the mean value of the baseline (N = 4096). At this rates the shaping time in the analog amplifier can be set to 6 μs.

In these conditions we performed a specific comparison between the two MCAs DT5780 and DT5770 and the two digitizers DT5725 and DT5730 in a wide energy range of the γ radiation going from few tens of keV to about 3 MeV, with the two detectors described above. We will now present the main results of this analysis, while in the next Section we will discuss which are the proper acquisition parameters to set in order to mantain a good resolution also in high counting rate measurements.

Comparison between the two MCAs: DT5780 and DT5770

To compare the performances of the two MCAs we started with detector 1 (see previous Section for details). When connected to the analog chain, in low counting rate conditions ($\sim$ 700 Hz) with the low-intensity ^{60}Co source, we obtained a resolution of 2.21 keV for the peak at 1332 keV.

We supplied the high and low voltage from the DT5780 and analysed the output spectra from the readout channels of the DT5780 and the DT5770. The relevant acquisition parameters were set as explained above; the only setting that was changed during the tests was the trapezoid gain, which allows to spread the spectrum over more channels, thus exploiting all the dynamic range of the ADC. The trapezoid gain for the two MCAs were set in order to have the Cobalt peaks around the central channels of the full spectrum range and at nearly the same position for both the DT5780 and the DT5770. The resulting resolutions at 1332 keV are reported in Table B.1.

	Trap. Gain	FWHM (keV)
DT5780	3	2.050 $\pm$ 0.003
DT5770	4	2.223 $\pm$ 0.004

Table B.1.: FWHM at 1332 keV obtained for the two MCAs with the best parameters for resolution measurements.

The DT5770 gives a result that is comparable with the resolution obtained with the analog system, while the DT5780 is almost 10% better. The increase in trapezoid gain with respect to the default value of 1 results in a substantial improvement of the resolution for both the MCAs (about 0.1 keV). The slight difference between the two may arise from the different input ranges of the ADCs (1.25 V for the DT5770 versus 0.6 V for the DT5780).

The comparison was carried out also in the low-energy range using detector 2 and the ^{133}Ba source (counting rate on the detector ∼1 kHz). The parameters for the acquisition were left as in the previous measurements, except for the input range of the DT5780 that was increased to 1.4 V to have an end point of the spectra at 2.5-3 MeV. In Table B.2 one can see the resolutions FWHM obtained for some low-energy lines of ^{133}Ba with the two MCAs and the analog system.

	Analog	DT5780	DT5770
FWHM @ 35 keV	(512 ± 8) eV	(532 ± 8) eV	(551 ± 5) eV
FWHM @ 53 keV	(553 ± 10) eV	(606 ± 16) eV	(624 ± 10) eV
FWHM @ 81 keV	(643 ± 10) eV	(611 ± 6) eV	(661 ± 1) eV
FWHM @ 356 keV	(931 ± 11) eV	(970 ± 8) eV	(979 ± 7) eV

Table B.2.: FWHM at some low-energy lines of ^{133}Ba obtained for the two MCAs.

The resolutions obtained with the two MCAs are very similar also in the low-energy range and definitely comparable with those obtained with the analog system.

Comparison between the two digitizers: DT5725 and DT5730

As in the previous analysis, we started by using detector 1 with the low-intensity ^{60}Co source. The input range of both the ADCs was set to 0.5 V, the other parameters exactly as before. Also in this case the trapezoid gain was increased to spread the spectrum over more channels. The resulting resolutions for the peak at 1332 keV are reported in Table B.3.

	Trap. Gain	FWHM (keV)
DT5725	4	2.344 ± 0.004
DT5730	4	2.401 ± 0.005

Table B.3.: FWHM at 1332 keV obtained for the two digitizers with the best parameters for resolution measurements.

The resolution obtainable with these digitizers is always slightly worse with respect to the MCAs. This result was expected since their performances are not addressed to the best energy resolution.

As in the previous case, we compared the two digitizers also in the low-energy range with detector 2 and the ^{133}Ba source (counting rate on the detector ∼1 kHz), increasing the input range of the ADCs to 2.0 V and leaving the other parameters unchanged. In Table B.4 the resolutions for some γ lines are reported.

	Analog	DT5725	DT5730
FWHM @ 35 keV	(512 ± 8) eV	(532 ± 15) eV	(572 ± 4) eV
FWHM @ 53 keV	(553 ± 10) eV	(633 ± 24) eV	(659 ± 4) eV
FWHM @ 81 keV	(643 ± 10) eV	(636 ± 15) eV	(696 ± 5) eV
FWHM @ 356 keV	(931 ± 11) eV	(936 ± 12) eV	(1042 ± 5) eV

Table B.4.: FWHM at some low-energy lines of ^{133}Ba obtained for the two digitizers.

The two digitizers have very similar performances, even though the resolutions obtained with the DT5725 are always slightly better. We remind that the main difference between the two devices is the different sampling rate (higher for the DT5730 with respect to the DT5725). Moreover at these low energies the difference between MCA and digitizers seems much more reduced: they both give good results, fully comparable with each other.

Comparison at high counting rate

It is also interesting to test the performances of the digitizers when the counting rate (CR) on the detector is increased. In typical low-energy nuclear physics experiments the maximum CR on a detector rarely exceed 15-20 kHz. The comparison was carried out between the analog system and the MCA and the digitizer which give the best results in terms of resolution, namely the DT5780 and the DT5725. We used detector 1 and the two ^{60}Co sources. The shaping time of the shaping amplifier, the rise time of the trapezoid and the number of samples to calculate the mean value of the baseline had to be lowered as the counting rate increased over 10 kHz in order to avoid as much as possible the pile-up contribution and the consequent deterioration of resolution [99]. In Table B.5 are the two different sets of parameters that were changed from low-rate to high-rate measurements.

	CR $<$ 10 kHz	CR $\geq$ 10 kHz
Analog shaping time (μs)	6	3
Rise time (μs)	9	6
Baseline mean (samples)	4096	1024
Peak holdoff (μs)	5	10

Table B.5.: Parameters for high-resolution measurements in condition of low and high counting rates.

The resolutions obtained in these conditions are reported in Table B.6 after being normalized to the resolution at 1332 keV in the lowest counting rate conditions. This makes it easier to compare the different performances with the change of CR independently of the specific characteristics of each device, as it can be seen in Figure B.3.

CR (kHz)	Analog	DT5780	DT5725
0.5	1.000	1.000	1.000
1	1.009	0.999	1.005
5	1.067	1.017	1.048
10	1.040	1.036	1.058
15	1.071	1.058	1.107

Table B.6.: Normalized resolutions obtained in the comparison between analog, MCA and digitizer in different counting rate conditions. See text for details.

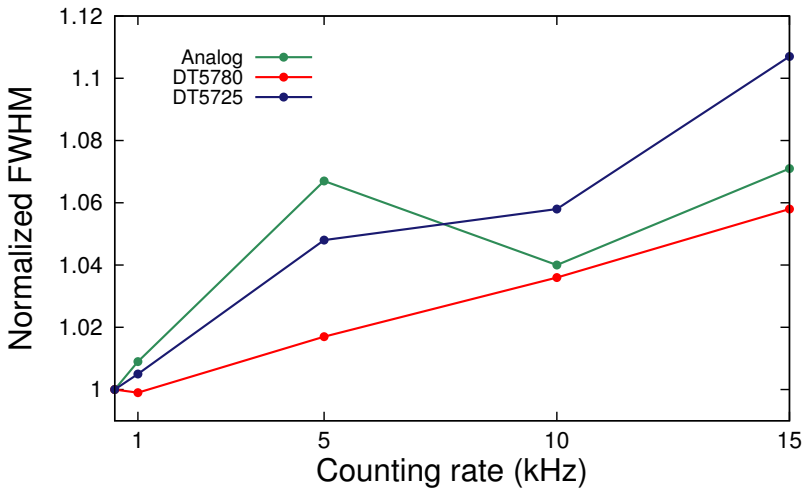

Figure B.3.: Trend of the resolution at 1332 keV for analog system (green), MCA (red) and digitizer (blue) normalized to the FWHM obtained with the lowest counting rate for each device.

The DT5780 shows the best (relative) performance at high counting rates, whereas the DT5725 does not manage yet to do better than the analog system. It is important to notice, anyway, that also in the case of the DT5725 the variation in resolution between the lowest and the highest CR does not exceed 11% (corresponding in our case to $\sim$ 0.2 keV). Further developments to diminish (and possibly invert) this gap are still under analysis.

Bibliography

[1] L. Corradi, G. Pollarolo, and S. Szilner. Multinucleon transfer processes in heavy-ion reactions. *Journal of Physics G: Nuclear and Particle Physics*, 36:113101–113143, 2009.

[2] Norman K. Glendenning et al. *Direct nuclear reactions*. World Scientific, 1983.

[3] Ricardo A. Broglia and Aage Winther. Heavy ion reactions. 1991.

[4] A. Winther. Dissipation, polarization and fluctuation in grazing heavy-ion collisions and the boundary to the chaotic regime. *Nuclear Physics A*, 594(2):203–245, 1995.

[5] D. R. Bes, R. A. Broglia, O. Hansen, and O. Nathan. Isovector pairing vibrations. *Physics Reports*, 34(1):1–53, 1977.

[6] M. Igarashi, K. Kubo, and K. Yagi. Two-nucleon transfer reaction mechanisms. *Physics Reports*, 199(1):1–72, 1991.

[7] W. Reisdorf. Heavy-ion reactions close to the Coulomb barrier. *Journal of Physics G: Nuclear and Particle Physics*, 20(9):1297, 1994.

[8] S. Szilner, L. Corradi, G. Pollarolo, S. Beghini, B. R. Behera, E. Fioretto, A. Gadea, F. Haas, A. Latina, G. Montagnoli, F. Scarlassara, A. M. Stefanini, M. Trotta, A. M. Vinodkumar, and Y. Wu. Multinucleon transfer processes in ^{40}Ca+^{208}Pb. *Physical Review C*, 71(4):044610, 2005.

[9] R. Bass. Nuclear reactions with heavy ions. 1980.

[10] L. Corradi, A. M. Stefanini, C. J. Lin, S. Beghini, G. Montagnoli, F. Scarlassara, G. Pollarolo, and A. Winther. Multinucleon transfer processes in ^{64}Ni+^{238}U. *Physical Review C*, 59(1):261, 1999.

[11] K. E. Rehm, A. M. van den Berg, J. J. Kolata, D. G. Kovar, W. Kutschera, G. Rosner, G. S. F. Stephans, and J. L. Yntema. Transition from quasi-elastic to deep-inelastic reactions in the ^{48}Ti+^{208}Pb system. *Physical Review C*, 37(6):2629, 1988.

[12] J. Wilczyński. Nuclear molecules and nuclear friction. *Physics Letters B*, 47(6):484–486, 1973.

[13] R. Bock. Heavy ion collisions, vol. 2. *IINorth-Holland, Amsterdam*, 1980.

[14] R. Krücken, W.-T. Chou, J. R. Cooper, C. W. Beausang, C. J. Barton, M. A. Caprio, R. F. Casten, A. A. Hecht, J. R. Novak, N. Pietralla, A. Wolf, and N. V. Zamfir. Lifetimes in neutron-rich fission fragments using the differential recoil distance method. *Physical Review C*, 64(1):017305, 2001.

[15] W. Von Oertzen, H. G. Bohlen, B. Gebauer, R. Künkel, F. Pühlhofer, and D. Scühll. Quasi-elastic neutron transfer and pairing effects in the interaction of heavy nuclei. *Zeitschrift für Physik A Atomic Nuclei*, 326(4):463–481, 1987.

[16] D. Montanari, L. Corradi, S. Szilner, G. Pollarolo, E. Fioretto, G. Montagnoli, F. Scarlassara, A. M. Stefanini, S. Courtin, A. Goasduff, F. Haas, D. Jelavić Malenica, C. Michelagnoli, T. Mijatović, N Soić, C. A. Ur, and M. Varga Pajtler. Neutron Pair Transfer in ^{60}Ni+^{116}Sn Far below the Coulomb Barrier. *Physical review letters*, 113(5): 052501, 2014.

[17] J. J. Valiente-Dobón, D. Mengoni, A. Gadea, E. Farnea, S. M. Lenzi, S. Lunardi, A. Dewald, Th. Pissulla, S. Szilner, R. Broda, et al. Lifetime Measurements of the Neutron-Rich N = 30 Isotones ^{50}Ca and ^{51}Sc: Orbital Dependence of Effective Charges in the fp Shell. *Physical review letters*, 102(24):242502, 2009.

[18] W. Von Oertzen and A. Vitturi. Pairing correlations of nucleons and multi-nucleon transfer between heavy nuclei. *Reports on Progress in Physics*, 64(10):1247, 2001.

[19] J. M. Quesada, G. Pollarolo, R. A. Broglia, and A. Winther. A simple parametrization of one-particle transfer form factors for heavy-ion reactions. *Nuclear Physics A*, 442 (2):381–396, 1985.

[20] L. Corradi, A. M. Vinodkumar, A. M. Stefanini, E. Fioretto, G. Prete, S. Beghini, G. Montagnoli, F. Scarlassara, G. Pollarolo, F. Cerutti, and A. Winther. Light and heavy transfer products in ^{58}Ni+^{208}Pb at the Coulomb barrier. *Physical Review C*, 66 (2):024606, 2002.

[21] A. Winther. GRAZING. `http://personalpages.to.infn.it/~nanni/grazing/`.

[22] A. Winther. Grazing reactions in collisions between heavy nuclei. *Nuclear Physics A*, 572(1):191–235, 1994.

[23] T. Mijatović, S. Szilner, L. Corradi, D. Montanari, G. Pollarolo, E. Fioretto, A. Gadea, A. Goasduff, D. Jelavić Malenica, N. Mărginean, M. Milin, G. Montagnoli, F. Scarlassara, N. Soić, A. M. Stefanini, C. A. Ur, and J. J. Valiente-Dobón. Multinucleon transfer reactions in the ^{40}Ar+^{208}Pb system. *Physical Review C*, 94(6):064616, 2016.

[24] J. Knoll and R. Schaeffer. Extended Seminar on Nuclear Physics. *ICTP, Heavy-Ion, High-Spin States and Nuclear Structure, Trieste, Italy*, 1, 1973.

[25] L. Corradi, A. M. Stefanini, D. Ackermann, S. Beghini, G. Montagnoli, C. Petrache, F. Scarlassara, C. H. Dasso, G. Pollarolo, and A. Winther. Multinucleon transfer reactions in ^{32}S+^{208}Pb close to the Coulomb barrier. *Physical Review C*, 49(6):R2875, 1994.

[26] E. Vigezzi and A. Winther. On the application of complex trajectories to direct heavy-ion reactions. *Annals of Physics*, 192(2):432–486, 1989.

[27] R. A. Broglia, G. Pollarolo, and A. Winther. On the absorptive potential in heavy ion scattering. *Nuclear Physics A*, 361(1):307–325, 1981.

[28] G. Pollarolo, R. A. Broglia, and A. Winther. Calculation of the imaginary part of the heavy ion potential. *Nuclear Physics A*, 406(2):369–389, 1983.

[29] V. V. Volkov. Deep inelastic transfers and complete fusion of complex nuclei. The new approach to the process of nuclear fusion. *Izv. Akad. Nauk SSSR, Ser. Fiz*, 50:1879, 1986.

[30] Z.-Q. Feng, G.-M. Jin, and J.-Q. Li. Production of heavy isotopes in transfer reactions by collisions of ^{238}U+^{238}U. *Physical Review C*, 80(6):067601, 2009.

[31] L. Zhu, Z.-Q. Feng, and F.-S. Zhang. Production of heavy neutron-rich nuclei in transfer reactions within the dinuclear system model. *Journal of Physics G: Nuclear and Particle Physics*, 42(8):085102, 2015.

[32] M.-H. Mun, G. G. Adamian, N. V. Antonenko, Y. Oh, and Y. Kim. Production cross section of neutron-rich isotopes with radioactive and stable beams. *Physical Review C*, 89(3):034622, 2014.

[33] M.-H. Mun, G. G. Adamian, N. V. Antonenko, Y. Oh, and Y. Kim. Toward neutron-rich nuclei via transfer reactions with stable and radioactive beams. *Physical Review C*, 91(5):054610, 2015.

[34] N. V. Antonenko, E. A. Cherepanov, A. K. Nasirov, V. P. Permjakov, and V. V. Volkov. Compound nucleus formation in reactions between massive nuclei: Fusion barrier. *Physical Review C*, 51(5):2635, 1995.

[35] G. G. Adamian, N. V. Antonenko, and W. Scheid. Model of competition between fusion and quasifission in reactions with heavy nuclei. *Nuclear Physics A*, 618(1):176–198, 1997.

[36] G. G. Adamian, N. V. Antonenko, W. Scheid, and V. V. Volkov. Treatment of competition between complete fusion and quasifission in collisions of heavy nuclei. *Nuclear Physics A*, 627(2):361–378, 1997.

[37] G. G. Adamian, N. V. Antonenko, W. Scheid, and V. V. Volkov. Fusion cross sections for superheavy nuclei in the dinuclear system concept. *Nuclear Physics A*, 633(3): 409–420, 1998.

[38] G. G. Adamian, N. V. Antonenko, and W. Scheid. Characteristics of quasifission products within the dinuclear system model. *Physical Review C*, 68(3):034601, 2003.

[39] G. G. Adamian, N. V. Antonenko, and W. Scheid. Feature of production of new superheavy nuclei in actinide-based complete-fusion reactions. *The European Physical Journal A*, 41(2):235–241, 2009.

[40] N. Wang, Z. Li, and X. Wu. Improved quantum molecular dynamics model and its applications to fusion reaction near barrier. *Physical Review C*, 65(6):064608, 2002.

[41] N. Wang, X. Wu, and Z. Li. Dynamic study of fusion reactions for ^{40,48}Ca+^{90,96}Zr around the Coulomb barrier. *Physical Review C*, 67(2):024604, 2003.

[42] N. Wang, Z. Li, X. Wu, J. Tian, Y. Zhang, and M. Liu. Further development of the improved quantum molecular dynamics model and its application to fusion reactions near the barrier. *Physical Review C*, 69(3):034608, 2004.

[43] J. Tian, X. Wu, K. Zhao, Y. Zhang, and Z. Li. Properties of the composite systems formed in the reactions of ^{238}U+^{238}U and ^{232}Th+^{250}Cf. *Physical Review C*, 77(6): 064603, 2008.

[44] K. Zhao, Z. Li, X. Wu, and Y. Zhang. Production probability of superheavy fragments at various initial deformations and orientations in the ^{238}U+^{238}U reaction. *Physical Review C*, 88(4):044605, 2013.

[45] K. Zhao, Z. Li, N. Wang, Y. Zhang, Q. Li, Y. Wang, and X. Wu. Production mechanism of neutron-rich transuranium nuclei in ^{238}U+^{238}U collisions at near-barrier energies. *Physical Review C*, 92(2):024613, 2015.

[46] N. Wang, K. Zhao, and Z. Li. Fusion and quasi-fission dynamics in nearly-symmetric reactions. *Science China Physics, Mechanics & Astronomy*, 58(11):1–9, 2015.

[47] V. I. Zagrebaev and W. Greiner. Unified consideration of deep inelastic, quasi-fission and fusion–fission phenomena. *Journal of Physics G: Nuclear and Particle Physics*, 31 (7):825, 2005.

[48] V. I. Zagrebaev, Yu. Ts. Oganessian, M. G. Itkis, and W. Greiner. Superheavy nuclei and quasi-atoms produced in collisions of transuranium ions. *Physical Review C*, 73(3): 031602, 2006.

[49] V. I. Zagrebaev and W. Greiner. Shell effects in damped collisions: a new way to superheavies. *Journal of Physics G: Nuclear and Particle Physics*, 34(11):2265, 2007.

[50] V. I. Zagrebaev and W. Greiner. Production of New Heavy Isotopes in Low-Energy Multinucleon Transfer Reactions. *Physical review letters*, 101(12):122701, 2008.

[51] V. I. Zagrebaev and W. Greiner. Synthesis of superheavy nuclei: A search for new production reactions. *Physical Review C*, 78(3):034610, 2008.

[52] V. I. Zagrebaev and W. Greiner. Production of heavy and superheavy neutron-rich nuclei in transfer reactions. *Physical Review C*, 83(4):044618, 2011.

[53] V. I. Zagrebaev and W. Greiner. Production of heavy trans-target nuclei in multinucleon transfer reactions. *Physical Review C*, 87(3):034608, 2013.

[54] V. I. Zagrebaev, B. Fornal, S. Leoni, and W. Greiner. Formation of light exotic nuclei in low-energy multinucleon transfer reactions. *Physical Review C*, 89(5):054608, 2014.

[55] V. I. Zagrebaev and W. Greiner. New way for the production of heavy neutron-rich nuclei. *Journal of Physics G: Nuclear and Particle Physics*, 35(12):125103, 2008.

[56] K.i Sekizawa and K. Yabana. Time-dependent Hartree-Fock calculations for multinucleon transfer processes in ^{40,48}Ca+^{124}Sn, ^{40}Ca+^{208}Pb, and ^{58}Ni+^{208}Pb reactions. *Physical Review C*, 88(1):014614, 2013.

[57] T. H. R. Skyrme. CVII. The nuclear surface. *Philosophical Magazine*, 1(11):1043–1054, 1956.

[58] K. Sekizawa and K. Yabana. Time-dependent Hartree-Fock calculations for multinucleon transfer and quasifission processes in the ^{64}Ni+^{238}U reaction. *Physical Review C*, 93(5):054616, 2016.

[59] P. Bonche, S. Koonin, and J. W. Negele. One-dimensional nuclear dynamics in the time-dependent Hartree-Fock approximation. *Physical Review C*, 13(3):1226, 1976.

[60] L. Corradi, J. H. He, D. Ackermann, A. M. Stefanini, A. Pisent, S. Beghini, G. Montagnoli, F. Scarlassara, G. F. Segato, G. Pollarolo, C. H. Dasso, and A. Winther. Multinucleon transfer reactions in ^{40}Ca+^{124}Sn. *Physical Review C*, 54(1):201, 1996.

[61] T. Kurtukian-Nieto, J. Benlliure, K.-H. Schmidt, L. Audouin, F. Becker, B. Blank, E. Casarejos, F. Farget, M. Fernandez-Ordonez, J. Giovinazzo, D. Henzlova, B. Jurado, J. Pereira, and O. Yordanov. Production cross sections of heavy neutron-rich nuclei approaching the nucleosynthesis r-process path around A = 195. *Physical Review C*, 89(2):024616, 2014.

[62] H. Alvarez-Pol, J. Benlliure, E. Casarejos, L. Audouin, D. Cortina-Gil, T. Enqvist, B. Fernandez-Dominguez, A. R. Junghans, B. Jurado, P. Napolitani, J. Pereira, F. Rejmund, K.-H. Schmidt, and O. Yordanov. Production of new neutron-rich isotopes of heavy elements in fragmentation reactions of ^{238}U projectiles at 1 A GeV. *Physical Review C*, 82(4):041602, 2010.

[63] J. Kurcewicz, F. Farinon, H. Geissel, S. Pietri, C. Nociforo, A. Prochazka, H. Weick, J. S. Winfield, A. Estrade, P. R. P. Allegro, et al. Discovery and cross-section measurement of neutron-rich isotopes in the element range from neodymium to platinum with the FRS. *Physics Letters B*, 717(4):371–375, 2012.

[64] C. H. Dasso, G. Pollarolo, and A. Winther. Systematics of isotope production with radioactive beams. *Physical review letters*, 73(14):1907, 1994.

[65] R. Broda. Spectroscopic studies with the use of deep-inelastic heavy-ion reactions. *Journal of Physics G: Nuclear and Particle Physics*, 32(6):R151, 2006.

[66] Y. X. Watanabe, Y. H. Kim, S. C. Jeong, Y. Hirayama, N. Imai, H. Ishiyama, H. S. Jung, H. Miyatake, S. Choi, J. S. Song, E. Clement, G. de France, A. Navin, M. Rejmund, C. Schmitt, G. Pollarolo, L. Corradi, E. Fioretto, D. Montanari, M. Niikura, D. Suzuki, H. Nishibata, and J. Takatsu. Pathway for the Production of Neutron-Rich Isotopes around the N = 126 Shell Closure. *Physical review letters*, 115(17):172503, 2015.

[67] J. Simpson, F. Azaiez, G. De France, J. Fouan, J. Gerl, R. Julin, W. Korten, P. J. Nolan, B. M. Nyako, G. Sletten, P. M. Walker, and the EXOGAM Collaboration. The EXOGAM array: a radioactive beam gamma-ray spectrometer. *Acta Physica Hungarica, New Series, Heavy Ion Physics*, 11:159–188, 2000.

[68] H. Geissel, P. Armbruster, K. H. Behr, A. Brünle, K. Burkard, M. Chen, H. Folger, B. Franczak, H. Keller, O. Klepper, et al. The GSI projectile fragment separator (FRS): a versatile magnetic system for relativistic heavy ions. *Nuclear Instruments and Methods in Physics Research Section B: Beam Interactions with Materials and Atoms*, 70(1):286–297, 1992.

[69] H. Geissel, H. Weick, M. Winkler, G. Münzenberg, V. Chichkine, M. Yavor, T. Aumann, K.H. Behr, M. Böhmer, A. Brünle, et al. The Super-FRS project at GSI. *Nuclear Instruments and Methods in Physics Research Section B: Beam Interactions with Materials and Atoms*, 204:71–85, 2003.

[70] T. Kubo, M. Ishihara, N. Inabe, H. Kumagai, I. Tanihata, K. Yoshida, T. Nakamura, H. Okuno, S. Shimoura, and K. Asahi. The RIKEN radioactive beam facility. *Nuclear Instruments and Methods in Physics Research Section B: Beam Interactions with Materials and Atoms*, 70(1):309–319, 1992.

[71] T. Kubo. In-flight RI beam separator BigRIPS at RIKEN and elsewhere in Japan. *Nuclear Instruments and Methods in Physics Research Section B: Beam Interactions with Materials and Atoms*, 204:97–113, 2003.

[72] G. N. Knyazheva, E. M. Kozulin, R. N. Sagaidak, A. Yu Chizhov, M. G. Itkis, N. A. Kondratiev, V. M. Voskressensky, A. M. Stefanini, B. R. Behera, L. Corradi, E. Fioretto, A. Gadea, A. Latina, S. Szilner, M. Trotta, S. Beghini, G. Montagnoli, F. Scarlassara, F. Haas, N. Rowley, P. R. S. Gomes, and A. Szanto de Toledo. Quasifission processes in ^{40,48}Ca+^{144,154}Sm reactions. *Physical Review C*, 75(6):064602, 2007.

[73] M. G. Itkis, I. M. Itkis, G. N. Knyazheva, and E. M. Kozulin. Fusion-fission and quasifission of superheavy systems in heavy-ion induced reactions. *Nuclear Physics A*, 834(1):374c–377c, 2010.

[74] E. M. Kozulin, E. Vardaci, G. N. Knyazheva, A. A. Bogachev, S. N. Dmitriev, I. M. Itkis, M. G. Itkis, A. G. Knyazev, T. A. Loktev, K. V. Novikov, E. A. Razinkov, O. V. Rudakov, S. V. Smirnov, W. Trzaska, and V. I. Zagrebaev. Mass distributions of the

system ^{136}Xe+^{208}Pb at laboratory energies around the Coulomb barrier: A candidate reaction for the production of neutron-rich nuclei at N = 126. *Physical Review C*, 86 (4):044611, 2012.

[75] E. M. Kozulin, G. N. Knyazheva, I. M. Itkis, M. G. Itkis, A. A. Bogachev, E. V. Chernysheva, L. Krupa, F. Hanappe, O. Dorvaux, L. Stuttgé, W. H. Trzaska, C. Schmitt, and G. Chubarian. Fusion-fission and quasifission of superheavy systems with Z = 110–116 formed in ^{48}Ca-induced reactions. *Physical Review C*, 90(5):054608, 2014.

[76] E. M. Kozulin, G. N. Knyazheva, S. N. Dmitriev, I. M. Itkis, M. G. Itkis, T. A. Loktev, K. V. Novikov, A. N. Baranov, W. H. Trzaska, E. Vardaci, S. Heinz, O. Beliuskina, and S. V. Khlebnikov. Shell effects in damped collisions of ^{88}Sr with ^{176}Yb at the Coulomb barrier energy. *Physical Review C*, 89(1):014614, 2014.

[77] E. M. Kozulin, G. N. Knyazheva, K. V. Novikov, I. M. Itkis, M. G. Itkis, S. N. Dmitriev, Yu. Ts. Oganessian, A. A. Bogachev, N. I. Kozulina, I. Harca, W. H. Trzaska, and T. K. Ghosh. Fission and quasifission of composite systems with Z = 108-120: Transition from heavy-ion reactions involving S and Ca to Ti and Ni ions. *Physical Review C*, 94(5): 054613, 2016.

[78] E. M. Kozulin, A. A. Bogachev, M. G. Itkis, I. M. Itkis, G. N. Knyazheva, N. A. Kondratiev, L. Krupa, I. V. Pokrovsky, and E. V. Prokhorova. The CORSET time-of-flight spectrometer for measuring binary products of nuclear reactions. *Instruments and Experimental Techniques*, 51(1):44–58, 2008.

[79] I. M. Itkis, E. M. Kozulin, M. G. Itkis, G. N. Knyazheva, A. A. Bogachev, E. V. Chernysheva, L. Krupa, Yu. Ts. Oganessian, V. I. Zagrebaev, A. Y. Rusanov, F. Goennenwein, O. Dorvaux, L. Stuttgé, F. Hanappe, E. Vardaci, and E. de Goés Brennand. Fission and quasifission modes in heavy-ion-induced reactions leading to the formation of Hs. *Physical Review C*, 83(6):064613, 2011.

[80] H. Grawe, K. Langanke, and G. Martínez-Pinedo. Nuclear structure and astrophysics. *Reports on Progress in Physics*, 70(9):1525, 2007.

[81] E. M. Burbidge, G. R. Burbidge, W. A. Fowler, and F. Hoyle. Synthesis of the elements in stars. *Reviews of modern physics*, 29(4):547, 1957.

[82] S. Zemlyanoy, V. I. Zagrebaev, E. Kozulin, Y. Kudryavtsev, V. Fedosseev, R. Bark, Z. Janas, and H. Othman. GALS–setup for production and study of heavy neutron rich nuclei. In *EPJ Web of Conferences*, volume 86, page 00067. EDP Sciences, 2015.

[83] K. Novikov, E. M. Kozulin, I. M. Harca, S. Dmitriev, A. Flueras, P. Greenlees, F. Hanappe, S. V. Khlebnikov, T. Loktev, J. Maurer, A. Di Nitto, J. Pakarinen, P. Ruotsalainen, M. Sandzelius, J. Sorri, M. Sin, W. H. Trzaska, E. Vardaci, and V. I. Zagrebaev. Production and investigation of neutron-rich Osmium isotopes with and around N = 126 using gas flow transport method. In *Journal of Physics: Conference Series*, volume 515, page 012016. IOP Publishing, 2014.

[84] S. C. Jeong, N. Imai, H. Ishiyama, Y. Hirayama, H. Miyatake, and Y. X. Watanabe. KISS: KEK isotope separation system for β-decay spectroscopy. *KEK Report*, 2, 2010.

[85] Y. Hirayama, Y. X. Watanabe, N. Imai, H. Ishiyama, S. C. Jeong, H. Miyatake, M. Oyaizu, S. Kimura, M. Mukai, Y. H. Kim, T. Sonoda, M. Wada, M. Huyse, Yu. Kudryavtsev, and P. Van Duppen. Laser ion source for multi-nucleon transfer reaction products. *Nuclear Instruments and Methods in Physics Research Section B: Beam Interactions with Materials and Atoms*, 353:4–15, 2015.

[86] Y. Hirayama, Y. X. Watanabe, N. Imai, H. Ishiyama, S. C. Jeong, H. S. Jung, H. Miyatake, M. Oyaizu, S. Kimura, M. Mukai, Y. H. Kim, T. Sonoda, M. Wada, M. Huyse, Yu. Kudryavtsev, and P. Van Duppen. On-line experimental results of an argon gas cell-based laser ion source (KEK Isotope Separation System). *Nuclear Instruments and Methods in Physics Research Section B: Beam Interactions with Materials and Atoms*, 376:52–56, 2016.

[87] S. Kimura, H. Ishiyama, H. Miyatake, Y. Hirayama, Y. X. Watanabe, H. S. Jung, M. Oyaizu, M. Mukai, S. C. Jeong, and A. Ozawa. Development of the detector system for β-decay spectroscopy at the KEK Isotope Separation System. *Nuclear Instruments and Methods in Physics Research Section B: Beam Interactions with Materials and Atoms*, 376:338–340, 2016.

[88] A. Pisent and M. Comunian. Complete simulation of the heavy ion Linac PIAVE. In *Particle Accelerator Conference, 1997. Proceedings of the 1997*, volume 1, pages 1132–1134. IEEE, 1997.

[89] A. Lombardi, G. Bassato, A. Battistella, M. Bellato, G. Bezzon, L. Bertazzo, C. Bisoffi, E. Bissiato, S. Canella, M. Cavenago, F. Cervellera, A. Chiurlotto, M. Comunian, A. Facco, P. Favaron, G. Fortuna, S. Gambalonga, M. Lollo, M. S. Moisio, V. Palmieri, R. Pengo, A. Pisent, M. Poggi, A. M. Porcellato, F. Scarpa, and L. Ziomi. The new positive ion injector PIAVE at LNL. In *Particle Accelerator Conference, 1997. Proceedings of the 1997*, volume 1, pages 1129–1131. IEEE, 1997.

[90] A. Lombardi. The Superconducting Radio Frequency Quadrupole Structures Review. *Part. Accel.*, 62:91–102, 1998.

[91] R. A. Ricci and C. Signorini. On the 16 MV XTU tandem of the laboratori nazionali di legnaro. *Nuclear Instruments and Methods in Physics Research*, 184(1):35–47, 1981.

[92] C. Signorini, G. Bezzon, F. Cervellera, P. Spolaore, and R. A. Ricci. Acceptance tests of the Legnaro XTU tandem. *Nuclear Instruments and Methods in Physics Research*, 220(1):30–36, 1984.

[93] C. Signorini, F. Cervellera, and G. Bezzon. Status report of the Legnaro XTU tandem. *Nuclear Instruments and Methods in Physics Research Section A: Accelerators, Spectrometers, Detectors and Associated Equipment*, 244(1):27–30, 1986.

[94] G. Bassato, G. P. Buso, F. Cervellera, A. Dainelli, A. Facco, P. Favaron, G. Fortuna, J. D. Larson, V. Palmieri, R. Pengo, A. M. Porcellato, K. Rudolph, B. Tiveron, I. Ben-Zvi, and J. S. Sikolowski. The Alpi project at the Laboratori Nazionali di Legnaro. In *European particle accelerator conference*, 1988.

[95] G. Fortuna, R. Pengo, G. Bassato, I. Ben-Zvi, J. D. Larson, J. S. Sokolowski, L. Badan, A. Battistella, G. Bisoffi, G. Buso, M. Cavenago, F. Cervellera, A. Dainelli, A. Facco, P. Favaron, A. Lombardi, S. Marigo, M. S. Moisio, V. Palmieri, A. M. Porcellato, K. Rudolph, R. Preciso, and B. Tiveron. The ALPI project at the Laboratori Nazionali di Legnaro. *Nuclear Instruments and Methods in Physics Research Section A: Accelerators, Spectrometers, Detectors and Associated Equipment*, 287(1):253–256, 1990.

[96] G. Fortuna, A.M. Porcellato, G. Bassato, A. Battistella, M. Bellato, L. Bertazzo, G. Bezzon, G. Bisoffi, G. Buso, S. Canella, M. Cavenago, F. Cervellera, A. Chiurlotto, A. Dainelli, N. Dainese, M. De Lazzari, A. Facco, P. Favaron, M. Lollo, A. Lombardi, S. Marigo, M. S. Moisio, V. Palmieri, R. Pengo, M. Poggi, J. S. Sokolowski, L. Badan, M. Barbadillo, R. Pegoraro, R. Preciso, and F. Scarpa. Completion of the medium-β section of the ALPI SC-booster at LNL. *Nuclear Instruments and Methods in Physics Research Section A: Accelerators, Spectrometers, Detectors and Associated Equipment*, 328(1):236–241, 1993.

[97] A. Dainelli, G. Bassato, A. Battistella, M. Bellato, A. Beltramin, L. Bertazzo, G. Bezzon, G. Bisoffi, L. Boscagli, S. Canella, D. Carlucci, F. Cervellera, A. Chiurlotto, T. Contran, M. De Lazzari, A. Facco, P. Favaron, G. Fortuna, S. Gustafsson, M. Lollo, A. Lombardi, S. Marigo, M. S. Moisio, V. Palmieri, R. Pengo, A. Pisent, M. Poggi, F. Poletto, A. M. Porcellato, and L. Ziomi. Commissioning of the ALPI post-accelerator. *Nuclear Instruments and Methods in Physics Research Section A: Accelerators, Spectrometers, Detectors and Associated Equipment*, 382(1):100–106, 1996.

[98] D. Shapira, T. A. Lewis, and L. D. Hulett. A fast and accurate position-sensitive timing detector based on secondary electron emission. *Nuclear Instruments and Methods in Physics Research Section A: Accelerators, Spectrometers, Detectors and Associated Equipment*, 454(2):409–420, 2000.

[99] G. F. Knoll. Radiation detection and measurement. *New York, John Wiley and Sons, Inc.*, 1, 1979.

[100] M. S. Livingston and H. A. Bethe. Nuclear physics c. nuclear dynamics, experimental. *Reviews of modern physics*, 9(3):245, 1937.

[101] H.-D. Betz. Charge states and charge-changing cross sections of fast heavy ions penetrating through gaseous and solid media. *Reviews of Modern Physics*, 44(3):465, 1972.

[102] C. R. Gruhn, M. Binimi, R. Legrain, R. Loveman, W. Pang, M. Roach, D. K. Scott, A. Shotter, T. J. Symons, J. Wouters, M. Zisman, R. Devries, Y. C. Peng, and W. Sondheim. Bragg curve spectroscopy. *Nuclear Instruments and Methods in Physics Research*, 196(1):33–40, 1982.

[103] R. Barna, V. Bollini, A. Bubak, A. Budzanowski, D. De Pasquale, D. Filges, S. V. Förtsch, F. Goldenbaum, A. Heczko, H. Hodde, et al. PISA–an experiment for fragment spectroscopy at the Internal Beam of COSY: application of an Axial Ionization Chamber. *Nuclear Instruments and Methods in Physics Research Section A: Accelerators, Spectrometers, Detectors and Associated Equipment*, 519(3):610–622, 2004.

[104] A. M. Stefanini, L. Corradi, G. Maron, A. Pisent, M. Trotta, A. M. Vinodkumar, S. Beghini, G. Montagnoli, F. Scarlassara, G. F. Segato, A. De Rosa, G. Inglima, D. Pierroutsakou, M. Romoli, M. Sandoli, G. Pollarolo, and A. Latina. The heavy-ion magnetic spectrometer PRISMA. *Nuclear Physics A*, 701(1):217–221, 2002.

[105] S. Szilner, C. A. Ur, L. Corradi, N. Mărginean, G. Pollarolo, A. M. Stefanini, S. Beghini, B. R. Behera, E. Fioretto, A. Gadea, et al. Multinucleon transfer reactions in closed-shell nuclei. *Physical Review C*, 76:024604, 2007.

[106] L. Corradi, S. Szilner, G. Pollarolo, D. Montanari, E. Fioretto, A. M. Stefanini, J. J. Valiente-Dobón, E. Farnea, C. Michelagnoli, G. Montagnoli, F. Scarlassara, C. A. Ur, T. Mijatović, D. Jelavić-Malenica, N. Soić, and F. Haas. Multinucleon transfer reactions: Present status and perspectives. *Nuclear Instruments and Methods in Physics Research Section B: Beam Interactions with Materials and Atoms*, 317:743–751, 2013.

[107] H. Savajols. VAMOS: A variable mode high acceptance spectrometer for identifying reaction products induced by SPIRAL beams. *Nuclear Instruments and Methods in Physics Research Section B: Beam Interactions with Materials and Atoms*, 204:146–153, 2003.

[108] M. Rejmund, B. Lecornu, A. Navin, C. Schmitt, S. Damoy, O. Delaune, J.M. Enguerrand, G. Fremont, P. Gangnant, L. Gaudefroy, et al. Performance of the improved larger acceptance spectrometer: VAMOS++. *Nuclear Instruments and Methods in Physics Research Section A: Accelerators, Spectrometers, Detectors and Associated Equipment*, 646(1):184–191, 2011.

[109] A. Cunsolo, F. Cappuzzello, A. Foti, A. Lazzaro, A. L. Melita, C. Nociforo, V. Shchepunov, and J. S. Winfield. Technique for 1st order design of a large-acceptance magnetic spectrometer. *Nuclear Instruments and Methods in Physics Research Section A: Accelerators, Spectrometers, Detectors and Associated Equipment*, 481(1):48–56, 2002.

[110] G. Montagnoli, A. M. Stefanini, M. Trotta, S. Beghini, M. Bettini, F. Scarlassara, V. Schiavon, L. Corradi, B. R. Behera, E. Fioretto, A. Gadea, A. Latina, S. Szilner, L. Donà, M. Rigato, N. A. Kondratiev, A. Yu. Chizhov, G. Kniajeva, E. M. Kozulin, I. V. Pokrovskiy, V. M. Voskressensky, and D. Ackermann. The large-area microchannel plate entrance detector of the heavy-ion magnetic spectrometer PRISMA. *Nuclear Instruments and Methods in Physics Research Section A: Accelerators, Spectrometers, Detectors and Associated Equipment*, 547(2):455–463, 2005.

[111] S. Beghini, L. Corradi, E. Fioretto, A. Gadea, A. Latina, G. Montagnoli, F. Scarlassara, A. M. Stefanini, S. Szilner, M. Trotta, and A. M. Vinodkumar. The focal plane detector

of the magnetic spectrometer PRISMA. *Nuclear Instruments and Methods in Physics Research Section A: Accelerators, Spectrometers, Detectors and Associated Equipment*, 551(2):364–374, 2005.

[112] E. Fioretto, L. Corradi, S. Szilner, D. Montanari, C. Michelagnoli, T. Mijatović, G. Montagnoli, F. Scarlassara, A. M. Stefanini, C. A. Ur, G. Pollarolo, and N. Soić. Sub-barrier transfer reactions studied with the magnetic spectrometer PRISMA. In *Journal of Physics: Conference Series*, volume 533, page 012006. IOP Publishing, 2014.

[113] ROOT - A Data Analysis Framework. URL `https://root.cern.ch/drupal`.

[114] R. Brun, F. Rademakers, S. Panacek, I. Antcheva, and D. Buskulic. The ROOT Users Guide. *CERN, http://root.cern.ch*, 03 2011.

[115] J. M. Asselineau, J. Duchon, M. L'Haridon, P. Mosrin, R. Regimbart, and B. Tamain. Performance of a Bragg curve detector for heavy ion identification. *Nuclear Instruments and Methods in Physics Research*, 204(1):109–115, 1982.

[116] femul subversion repository. `svn://gamma01.lnl.infn.it/agata/trunk/narval_emulator`.

[117] GammaWare - Agata Data Analysis. http://agata.in2p3.fr.

[118] Philipp Rudolf John. *Study of shape evolution in the neutron-rich osmium isotopes with the advanced gamma-tracking array AGATA*. PhD thesis, Università di Padova, 2015.

[119] A. Latina. *Study of Heavy-Ion Reactions with the Magnetic Spectrometer PRISMA: On-line and Off-line Data Analysis*. PhD thesis, Università degli Studi di Torino, 2005.

[120] Laboratori Nazionali di Legnaro Website. http://www.lnl.infn.it, 2014.

[121] P.-A. Söderström. *Collective structure of neutron-rich rare-earth nuclei and development of instrumentation for gamma-ray spectroscopy*. PhD thesis, Acta Universitatis Upsaliensis, 2011.

[122] D. Montanari. *Reaction dynamics of neutron rich nuclei in Ca isotopes with heavy ions and gamma spectroscopy*. PhD thesis, Università degli Studi di Milano, 2009.

[123] A. Gadea, N. Mărginean, L. Corradi, S. M. Lenzi, C. A. Ur, E. Farnea, G. De Angelis, E. Fioretto, D. R. Napoli, A. M. Stefanini, et al. The CLARA-PRISMA setup installed at LNL: first results. *Journal of Physics G: Nuclear and Particle Physics*, 31(10):S1443, 2005.

[124] S. Akkoyun, A. Algora, B. Alikhani, F. Ameil, G. De Angelis, L. Arnold, A. Astier, A. Ataç, Y. Aubert, C. Aufranc, et al. Agata—advanced gamma tracking array. *Nuclear Instruments and Methods in Physics Research Section A: Accelerators, Spectrometers, Detectors and Associated Equipment*, 668:26–58, 2012.

[125] T. Mijatović. *Study of heavy-ion reactions with large solid angle magnetic spectrometers*. PhD thesis, Ruder Bosković Institute, 2015.

[126] B. Birkenbach. *Gamma ray tracking with the AGATA demonstrator - A novel approach for in-beam spectroscopy.* PhD thesis, Universiät zu Köln, 04 2014.

[127] A. G. H. Vogt. In-Beam Gamma-Ray Spectroscopy of Neutron-Rich Actinides after Multi-Nucleon Transfer Reactions. Master's thesis, Universiät zu Köln, 06 2014.

[128] A. Vogt, B. Birkenbach, P. Reiter, L. Corradi, T. Mijatović, D. Montanari, S. Szilner, D. Bazzacco, M. Bowry, A. Bracco, et al. Light and heavy transfer products in ^{136}Xe+^{238}U multinucleon transfer reactions. *Physical Review C*, 92(2):024619, 2015.

[129] A. B. Brown, C. W. Snyder, W. A. Fowler, and C. C. Lauritsen. Excited States of the Mirror Nuclei, ^{7}Li and^{7}Be. *Physical Review*, 82(2):159, 1951.

[130] L. C. Northcliffe and R. F. Schilling. Range and stopping-power tables for heavy ions. *Atomic Data and Nuclear Data Tables*, 7(3):233–463, 1970.

[131] L. Corradi, G. Montagnoli, D. R. Napoli, P. Spolaore, A. M. Stefanini, X. Jincheng, S. Beghini, F. Scarlassara, G. F. Segato, F. Soramel, et al. A kinematic coincidence technique for the study of low-energy heavy-ion reactions. *Nuclear Instruments and Methods in Physics Research Section A: Accelerators, Spectrometers, Detectors and Associated Equipment*, 297(3):461–466, 1990.

[132] CAEN Tools for Discovery. CAEN Tools for Discovery. `http://www.caen.it`.

List of Figures

List of Tables

Acknowledgements

Many people have contributed to make these last three years extremely interesting and stimulating from both a scientific and a personal point of view. In primis I would like to thank dott. Enrico Fioretto and dott. Lorenzo Corradi. They followed me with their invaluable help and support during this PhD, teaching me a lot with enthusiasm and patience. They have been constantly present to discuss about the analysis, to explain me the operation of the detectors and eventually to read and correct this thesis. I owe them most of what I have learnt in these years.

I thank dott. Philipp John for initiating me into the analysis of PRISMA data with ROOT and for providing me with the essential tools to take on the first steps of my work. In this I was assisted also by Marco Siciliano, my office mate, dott. Alain Goasduff and dott. Tea Mijatović: I had to opportunity to share with them fruitful discussions, which helped me in overtaking some particularly demanding points of the analysis.

I would like to thank dott. Suzana Szilner and dott. Dieter Ackermann not only for their fundamental contribution during the experiment but also for reading this thesis and giving me a series of indispensable comments and corrections which have surely increased its quality. I include in these thanks all the rest of the PRISMA group, dott. Alberto Stefanini, dott. Giovanna Montagnoli, dott. Daniele Montanari, prof. Fernando Scarlassara and Giulia Colucci for their support and for allowing me to participate in many experiments, seminars and conferences which have made my experience as a PhD student much richer.

Sincere thanks go to prof. Nanni Pollarolo who provided me not only with the theoretical calculations necessary to interpret the results but also with extremely precious ideas for the continuation and improvement of my analysis.

I thank CAEN and in particular dott. Paola Garosi and dott. Matteo Corbo for giving me the opportunity to move my first steps into the field of digitizers. They helped me with care and promptness and generously gave me useful advice to improve my work.

A special thank goes to Davide Rosso, who hosted me in his laboratory for months and helped me in my activity in every possible way, teaching me several “tricks” about HPGe detectors. It was a pleasure to work with him.

I would like to thank also dott. Gabriele Pasquali and dott. Tommaso Marchi. Gabriele developed the pClasses that I used in the analysis of the digital signal of the Bragg chamber,

Tommaso taught me how to use them and has always been available when I needed help.

Last but not least, a special mention goes to my family, to Chiara, who will soon be part of it, and to all my friends. Looking back now to these three years I can more clearly realize how important their constant presence and support have been and how lucky I feel having these people in my life.

Molte persone hanno contribuito a rendere questi ultimi tre anni estremamente interessanti e stimolanti da un punto di vista sia scientifico che umano. In primis vorrei ringraziare il dott. Enrico Fioretto e il dott. Lorenzo Corradi. Mi hanno seguito con i loro inestimabili aiuto e supporto durante questo dottorato, insegnandomi moltissimo con entusiasmo e pazienza. Sono stati costantemente presenti per discutere dell'analisi, per spiegarmi il funzionamento dei rivelatori e infine per leggere e correggere questa tesi. Devo a loro la maggior parte di ciò che ho appreso in questi anni.

Ringrazio il dott. Philipp John per avermi iniziato all'analisi dei dati di PRISMA con ROOT e per avermi fornito gli strumenti essenziali per affrontare i primi passi del mio lavoro. In questo sono stato assistito anche da Marco Siciliano, mio compagno di ufficio, dal dott. Alain Goasduff a dalla dott.ssa Tea Mijatović: ho avuto la possibilità di condividere con loro discussioni proficue che mi hanno aiutato a superare dei punti particolarmente impegnativi dell'analisi.

Vorrei ringraziare la dott.ssa Suzana Szilner e il dott. Dieter Ackermann non solo per il loro fondamentale contributo durante l'esperimento ma anche per aver letto questa tesi e avermi fornito una serie di commenti e correzioni indispensabili, che hanno certo contribuito ad aumentare la qualità della tesi stessa. Includo in questi ringraziamenti tutto il gruppo PRISMA, il dott. Alberto Stefanini, la prof.ssa Giovanna Montagnoli, il dott. Daniele Montanari, il prof. Fernando Scarlassara e Giulia Colucci per il loro supporto e per avermi permesso di partecipare a numerosi esperimenti, seminari e conferenze che hanno reso la mia esperienza come studente di dottorato più ricca.

Un ringraziamento sincero va al prof. Nanni Pollarolo che mi ha fornito non solo i calcoli teorici necessari ad interpretare i risultati ma anche idee estrememamente preziose per la continuazione ed il miglioramento della mia analisi.

Ringrazio la CAEN e in particolare la dott.ssa Paola Garosi ed il dott. Matteo Corbo per avermi dato l'opportunità di muovere i miei primi passi nel campo dei digitalizzatori. Mi hanno aiutato con attenzione e sollecitudine e si sono profusi in utili consigli per migliorare il mio lavoro.

Un grazie speciale va a Davide Rosso, che mi ha ospitato nel suo laboratorio per mesi e mi ha aiutato nella mia attività in ogni modo possibile, insegnandomi diversi "trucchi" sui rivelatori HPGe. È stato un piacere lavorare con lui.

Vorrei ringraziare anche il dott. Gabriele Pasquali ed il dott. Tommaso Marchi. Gabriele ha sviluppato le pClasses che ho utilizzato nell'analisi del segnale digitale della camera di Bragg, Tommaso mi ha insegnato ad usarle ed è stato sempre disponibile quando avevo bisogno di un aiuto.

Ultimo ma non meno importante, una menzione speciale va alla mia famiglia, a Chiara, che presto ne entrerà a far parte, e a tutti i miei amici. Guardando ora indietro a questi tre anni mi rendo conto con maggiore chiarezza di quanto importanti siano stati la loro presenza costante e il loro supporto e di quanto mi senta fortunato ad avere queste persone nella mia vita.